SYNTHESIS AND ASSEMBLY OF NANOPARTICLES AT AIR-WATER INTERFACE

THESIS SUBMITTED TO

THE UNIVERSITY OF PUNE

FOR THE DEGREE OF

DOCTOR OF PHILOSOPHY

IN

CHEMISTRY

BY

Ms. ANITA SUBHASH SWAMI

MATERIALS & PHYSICAL CHEMISTRY DIVISION

NATIONAL CHEMICAL LABORATORY

PUNE 411 008

INDIA

DECEMBER 2004

Dedicated to parents and teachers

DECLARATION

I, **Ms. Anita Subhash Swami**, hereby declare that the work incorporated in this thesis entitled "*Synthesis and assembly of nanoparticles at air-water interface*" carried out by me at Materials and Physical Chemistry Division, National Chemical Laboratory, Pune, has not been submitted for the award of any other degree or diploma.

Date: (Anita Subhash Swami)
Place:

CERTIFICATE

This is to certify that the work discussed in the thesis entitled "*Synthesis and assembly of nanoparticles at air-water interface*" by **Ms. Anita Subhash Swami**, for the degree of Doctor of Philosophy was carried out under my supervision in the Materials and Physical Chemistry Division, National Chemical Laboratory, Pune. Such material as has been obtained by other sources have been duly acknowledged in this thesis. To the best of my knowledge, the present work or any part thereof, has not been submitted to any other University for the award of any other degree or diploma.

Date: (Dr. Murali Sastry)

Place: Research Supervisor

ACKNOWLEDGEMENTS

TABLE OF CONTENTS

CHAPTER IV: SYNTHESIS OF NANOSTRUCTURES AT THE AIR-WATER INTERFACE BY THE SPONTANEOUS REDUCTION OF PRECURSOR METAL IONS IN THE SUBPHASE USING LANGMUIR MONOLAYERS AS REDUCING AGENTS

CHAPTER V: SYNTHESIS OF NANOSTRUCTURES BY THE REDUCTION OF PRECURSOR METAL IONS CONSTRAINED TO A MONOLAYER AT THE AIR-WATER INTERFACE

CHAPTER VI: Summary

C H A P T E R I

Introduction

This chapter is an introduction to the thesis and gives a brief overview about the interest in assembling nanoparticles in two-dimensional (2D) and three-dimensional (3D) ordered structures and several methods available in the literature for the same. It also discusses the importance of anisotropic nanostructures with respect to their optical and catalytic properties and efforts that have been made to achieve them. Besides, it includes protocols used in present work for the 2D assembly of nanoparticles as well as for the synthesis of anisotropic nanostructures, both using the air-water interface.

1.1   Introduction

Nanostructures-structures that are defined to have at least one dimension in the range 1-100 nm, have received steadily growing interest as a result of their peculiar properties, organization to form superstructures and applications superior to their bulk counterparts. Metallic nanoparticles, gold and silver in particular have fascinated scientists since the Middle Ages because of their colorful colloidal solutions [1]. They were used as pigments to give brilliant ruby red and yellow color to the paintings and stained glasses used in cathedrals at that time [1]. Optical properties of nanoparticles continue to attract scientists even today. It is now recognized that the origin of unusual optoelectronic and physicochemical properties of nanoparticles lies in quantum confinement of electrons by the potential wells of nanometer-sized structures [2]. Nanoparticles, nanostructures, nanoscience, nanotechnology… have become most frequently used terms in the current literature of materials science. From point of view of the common man, nanotechnology appears to be the fabrication of miniature machines, which will be able to travel through the human body and repair damaged tissues or supercomputers small enough to fit in a pocket. However nanostructured materials have potential applications in many more areas such as optoelectronics [3], single electron transistors and light emitters [4], non-linear optical devices [5], catalysis [6], solar energy conversion [7] photonic band gap materials [8] and biomedical applications [9]. In order to realize the practical devices with nanomaterials utilizing their unique properties, the individual nanoparticles need to be assembled in a desired fashion. Nanotechnology provides the tools to play with the ultimate toy box of nature- atoms and molecules where everything is made from it and the possibilities to create new things are limitless. In more scientific terms, nanotechnology actually deals with the manipulation and control of individual atoms and thereby the programmed formation of superstructures. Two major approaches currently being used for the generation of organized nanoscale assemblies are the "top-down" (engineering down) and "bottom-up" (engineering up) methods. Top down approach involves generation of patterned structures by suitable lithographic and ion implantation technique and marks the beginning of silicon-integrated chip technology

[10]. However it has been realized that the current rate of miniaturization in silicon memory technology will be affected very soon by the physical limits of device dimensions imposed by ultra-violet, electron/ion beam and soft x-ray lithographic techniques (known as Moore's law). This is the reason why the bottom-up approaches assume considerable importance in comparison with top-down approaches.

Ordered metal nanoparticle assemblies with well-defined two-dimensional (2D) and three-dimensional (3D) spatial configurations achieved by bottom-up methods are expected to show novel properties that are not present in the isolated particles [11]. Hence 2D and 3D superlattices prepared from tailored nanocrystalline building blocks provide new opportunities to optimize and enhance the properties and performance of the materials. Thus though the properties of individual particles or a collection of well-separated particles in colloidal solution are of great interest to understand the fundamental properties of nanoparticles like their energy structure and relaxation mechanism, the study of collective properties of assembled nanostructures has become an important element of nanotechnology research in recent years. The macroscopic properties of the nanocrystal superlattices is determined not only by the properties of each individual particle (as a function of their size and shape) but by the coupling/interaction between nanocrystals interconnected and isolated by a monolayer of thin organic molecules (capping material). For instance, applications of nanoparticle-based materials are emerging in which collective nanoparticle optical properties are exploited for colorimetric, surface enhance Raman and surface plasmon resonance bioassays [12]. The parameters that influence the collective behaviour of assembled nanostructures can now be manipulated by chemists with better degree of control thus providing new initiative in research on cluster engineered materials.

Further, it has been now recognized that along with size and composition, shape of nanoparticles plays an important role in manipulating its electronic and chemical properties. For example, transition metal surfaces are known to have very efficient catalytic properties for many important reactions. Since nanoparticles have very high surface to volume ratio, their potential use in catalysis is obvious. It has been

demonstrated by Sayed and co-workers that different atomic planes available on the surface of shapes other than spheres can also translate into materials that catalyze different reactions based on their shape [6]. There is also great current interest in nanorods and nanowires due to the absorption of visible light both along the length of the nanorod (the longitudinal plasmon band) and along the width of the nanorod (the transverse plasmon band). The larger the aspect ratio, the more red-shifted the longitudinal plasmon band is, as theory predicts [6c] and experiment confirms [13]. Recent exciting work with semiconductor nanorods and nanowires has shown that polarized light emission and lasing are observable from these nanomaterials [14]. Others have predicted and in some cases shown that unique and improved surface-enhanced Raman scattering properties [15], magnetic properties [16] and electronic properties [17] are possible with anisotropic nanomaterials compared to spheres. Metallic nanorods or nanowires may be useful as interconnects for various optoelectronic devices [18]. Million-fold fluorescence enhancement in gold nanorods and the first observation of distinct quadrupole plasmon resonances in silver nanoprisms are some of the exciting shape dependent properties reported recently. Plate and rodlike nanoparticles are also attractive because of their liquid crystalline phase behaviour [19].

Thus with these fundamentally interesting and technologically important goals in mind various methods have been developed to achieve 2D and 3D ordered assemblies of nanoparticles and variety of chemical routes have been reported for generating anisotropic nanostructures having different shapes, overview of which is given in following sections.

1.2 Various methods for two-dimensional (2D) and three-dimensional (3D) organization of nanoparticles

1.2.1 Immobilization on self assembled monolayers

Self-assembled monolayers (SAM) of organic bifunctional molecules on gold or aluminum substrates with terminal thiol groups have been widely used for creating arrays of quantum dots. When immersed in colloidal solution, these free thiols bind the colloid and anchor it to the surface. Alivisatos and coworkers [20] were the first to show the capability of 2D SAM of 1,6 hexanedithiol, formed on gold thin film in organization of

CdS nanoparticles through covalent interactions. In another approach they have shown that carboxylic acid derivatized CdS nanoparticles can also be arranged on aluminium thin film [20]. The self-assembly in this case occurs through electrostatic interaction of the free carboxylic groups on the CdS surface with the aluminium atoms on the surface of the substrate [20]. Similar strategy has been extended by Sastry and co-workers for the organization of silver nanoparticles on 2D SAMs of aromatic bifunctional molecules such as 4-CTP and 4-ATP on both gold and aluminium thin film surfaces using covalent and electrostatic interactions respectively [21]. The salient features of the work were the control over the silver nanoparticle density in the SAM by pH-dependent modulation of the electrostatic interactions and the reversibility of the nanoparticle adsorption process [21]. Recently, this approach has been extensively used by others for fabrication of arrays of Au nanoparticles [22]. In yet another approach, CdS, PbS and Ag nanoparticles have been grown by chemical method using bifunctional SAM [23]. In this method, nanoparticles were formed at the surface of SAM by immersing it in precursor metal ion solution while bubbling H_2S gas or hydrazine gas though the solution resulting in 2D organization of nanoparticles [23]. Further, it has been shown that the spontaneous and directed assembly for 2D structures can be easily extended to multilayer superlattices (3D assemblies) by repeating the process of self-assembly. In this approach, a linker molecule is first assembled on a substrate (preferably dithiol molecules are assembled on gold substrate). A monolayer of nanoparticles is then assembled and covered yet with another layer of dithiols upon which another layer of nanoparticles can be prepared. In this method, alternating layers of nanoparticles of different sizes as well as different compositions can be used, as shown by Rao and coworkers [24] as well as by Natan and coworkers [24]. One of the most striking examples is the achievement of 3D CdSe quantum dot superlattices, reported by Bawendi and coworkers [24].

1.2.2 Electrophoretic deposition

In the process of electrophoretic deposition, two metal electrodes (usually indium tin oxide electrode) are immersed in a small glass cell containing colloidal solution. The charged nanoparticles migrate under the influence of electric field and get deposited on

the electrode. The rate of nanoparticle deposition depends on both the applied voltage and initial concentration of colloidal solution. The formation of large monolayer domains can be rationalized by assuming that the colloidal particles migrate over the grid surface (and over each other) until they can find sites with the highest positive electrostatic potential, since this leads to the greatest free energy gain for the colloid particles. So incoming colloidal particles are deflected to unoccupied surface sites and do not induce multilayer condensation of the colloid. Most of the adsorbed solvent is displaced by the colloidal particles prior to removal of the grid from the solution, and hence both the emersion from the solution and the subsequent evaporation of the remaining solvent on the grids no longer drastically affect the development of ordered domains. Particles can form well-ordered 2D lattices with almost macroscopic dimensions by the use of electrophoretic deposition. Electrophoretically deposited colloidal particles move toward one another over very large distances (greater that five particle diameters) to form 2D colloidal crystals. This coalesence of particles with the same charge is opposite to what is expected from electrostatic considerations and appears to result from electrohydrodynamic fluid flow arising from an ionic current flowing through the solution. The ability to modulate this "lateral attraction" between particles, by adjusting field strength or frequency, facilitates the reversible formation of 2D fluid and crystalline colloidal states on electrode surface [25]. Gersig and Mulveney [26] have succeeded in assembling aqueous citrate reduced gold nanoparticles [26a] as well as thiol capped gold nanoparticles [26b] as a 2D array on the copper grid. 2D organization of Pt nanoparticles by electrophoretic depostion has also been established by others [27]. Recently, Kamat and coworkers have shown that electrophoretic deposition methodology is quite effective in assembling gold nanoparticles as a 3D array without inducing interparticle interactions [28].

1.2.3 Spontaneous organization by solvent evaporation

It has been shown by several groups [19b, 29] that nanoparticles with a very narrow size distribution form spontaneous self-assembled structures when deposited from a solution phase onto a solid substrate by carefully adjusting the rate of solvent evaporation. Success of the method depends on various parameters such as nanoparticle

concentration, solvent evaporation, narrow size distribution, ionic strength, and surfactant concentration. The influence of the solvent evaporation process on 2D and 3D assembly of silver nanoparticles from their solution phase has been studied in great detail by Pileni and coworkers [29c-d, 30]. There are several examples in the literature for the evaporation induced 2D and 3D assembly of alkanethiol/alkylamine capped gold and silver nanoparticles [31]. Although a narrow size distribution is thought to be required to form nanocrystal superlattices extending over large areas, it has been shown by Kiely et al. that it is possible to produce ordered arrays of nanoparticles from bimodal distribution of sizes of the same metal [32a] and also of different metals [32b]. They have shown the formation of AB$_2$ and AB superlattice arrays consisting of gold and silver nanoparticles where size distribution of each metal fraction (A or B) was very narrow. Along with stabilizing the nanoparticles in solution, the capping material also controls the interparticle distances of self-assembled structures. By comparing the measured separation between two neighbouring particles with twice the chain length of the capping molecules [30,33], it has been shown that the hydrocarbon chains of capping molecules are interdigitated. Therefore the nanoparticles cannot come too close to each other simply because of steric hindrance that can be controlled in a designed fashion by varying the hydrocarbon chain length of the capping molecule. Even greater chemical control can be achieved by using bifunctional ligands [34], which are bound to the surface of the nanoparticles and can bring to a neighbouring particle during the assembly process via the second functional group.

1.2.4 Biological template based methods

DNA is among the most commonly used biological template used for 3D assembly of nanoparticles. Addition of colloidal particles modified with thiolated oligonucleotides (single stranded DNA) to complementary linker oligonucleotide strands allows the formation of extended structures with control over particle chemical composition, periodicity, and aggregate thermal stability. High control over the optical, mechanical and electrical properties of these hybrid bioinorganic materials was demonstrated for gold nanoparticles with DNA independently by Mirkin and coworkers

[35] as well as Alivisatos and coworkers [36]. Arrays of nanoparticles have also been created using the inherent repeating patterns of bacterial S-layer proteins [37]. Bacterial self-assembling S-layer protein lattices display a highly repetitive surface structure that makes them particularly suitable as biotemplates to fabricate arrays of metallic/semiconducting nanostructures [37]. Tobacco mosaic virus (TMV) is yet another biological template that has been used in the synthesis and organization of nanoparticles [38]. The TMV has a cylindrical structure with dimensions, roughly 300 x 18 nm with 4 nm wide central channel consisting of 2130 identical protein subunits arranged helically around RNA single strand. The charged amino acid residues on the surface of proteins act as nucleation sites for nanoparticles deposition. Mann and co-workers have demonstrated the assembly of PbS, CdS and SiO_2 on the surface of TMV structures [38].

1.2.5 Lithography

Nanosphere lithography as developed by Van Duyne et al. [39] could also be regarded as a template-based method and is one of the 'top-down' approaches for ordered arrays of nanostructures using self-assembled colloid monolayers. In this method, colloidal particles of the size 10 nm to 10 μm (such as polystyrene latex spheres) are assembled to form a monolayer on a suitable substrate by spreading the colloidal particles by simple solvent evaporation. Control over the solvent evaporation rate is important in realizing an ordered, hexagonal arrangement of colloidal particles on the substrate. The growth of the colloidal particle monolayer may also be achieved by other techniques such as the Langmuir-Blodgett technique [40], spin coating [41] of the colloidal suspension or by slow withdrawal of a substrate from the colloidal suspension. After formation of an ordered monolayer of the colloidal particles on the desired substrate, metal is evaporated into the spaces between the colloids, which are subsequently removed usually by ultrasonic agitation. This gives rise to an ordered array of metallic nanostructures in a honeycomb pattern [39]. The size of the particles can be controlled by the size of the colloidal spheres, and the shape can be controlled by the angle of incidence between the substrate and the material deposition beam [39]. The dimensions of the 2D order are determined by the assembly of the colloidal particles and hence the template. An

important thing to be noted here is that these arrays consist of naked metallic clusters as no organic molecules are bound to them. Apart from nanosphere lithography, Mirkins group has demonstrated how one can use high-resolution lithographic technique, called dip-pen lithography combined with wet etching techniques to generate arrays of Au nanostructures functionalized with oligonucleotides [42]. The process provides control over feature size, shape, interfeature distance and the type of biomolecules immobilized on the nanofeatures [42].

1.2.6 Polymer mediated organization of nanoparticles

Another interesting approach for realizing 2D arrays of nanoparticles is based on the use of surface modified polymers. Natan and coworkers [43] have shown the self-assembly of gold and silver nanoparticles onto immobilized polymers having pendant functional groups with high affinity for nanoparticles (e.g. -CN, -NH$_2$, -SH, PH(Ph)$_2$) [x]. In yet another example, formation of ordered arrays of ligand-stabilized gold nanoparticles, [Au$_{55}$(PPh$_3$)$_{12}$Cl$_6$] was accomplished by a polyelectrolyte thin film [44]. In this case, cluster density in the monolayer on the polymer surface, as observed by atomic force microscopy, can be controlled by variation of the reaction times of the polymer film with the cluster solution [44]. Tailor-made gold nanoparticle monolayer arrays have also been achieved using polymer nanosheets composed of amphiphilic copolymers, poly(N-dodecyl acrylamide-co-4-vinyl pyridine) [p(DDA/VPy)] LB films [45]. Predominant factors to immobilize gold nanoparticles are based on electrostatic interaction between nanoparticles and p(DDA/VPy) LB films. The VPy moieties are uniformly distributed in the polymer nanosheet; consequently, a 2D homogeneous gold nanoparticle monolayer can be formed onto the polymer nanosheets [45]. Recently, Chumanov's group has proven poly(vinylpyridine) to be a universal monofunctional surface modifier for the immobilization of various metal, semiconductor and dielectric nanoparticles on different substrates [46]. A preferred method of modification is the adsorption of the polymer from an alcohol solution followed by thorough rinsing to remove weakly bound molecules and by high temperature annealing for the further stabilization of the polymer film [46].

Advantage of this method is that it can be successfully applied for the modification of just about any surface including metals, oxides, plastics, and so forth [46].

1.2.7 Laser induced organization of nanoparticles

Kawasaki et al. have demonstrated that Ag and Au island films sputter-deposited on mica could be converted to a dense monolayer or 2D array of spherical nanoparticles without aggregation by post deposition nanosecond laser irradiation at 532 nm in a relatively narrow range of laser fluence [47]. These nanoparticles are essentially free from any protective material, and may be easily modified and derivatized by many different kinds of molecular species if necessary for desired application.

1.2.8 Organization at the air-water interface

Fendler et al pioneered the use of the air-water interface for the synthesis as well as assembly of nanoparticles employing Langmuir-Blodgett technique. Further, the technique was successively used by other groups for formation of colloidal particulate films of different technologically important materials. Particulars of the research in this area have been discussed in following sections.

1.2.8-1 *Immobilization of nanoparticles at air-water interface using electrostatic interaction*

This strategy consists of spreading of oppositely charged Langmuir monolayer on the surface of aqueous solution of charged colloidal particles. The electrostatic immobilization of negatively charged carboxylic acid derivatized gold [48], silver [49] and cadmium sulphide [50] nanoparticles at the air-water interface using positively charged fatty amine Langmuir monolayer has been studied in detail by Sastry and co-workers. The advantage of this approach for the 2D assembly of nanoparticles is that varying the charge on the amine molecules through colloidal subphase pH, one can control the degree of cluster incorporation into the Langmuir monolayer.

1.2.8-2 *Spreading surfactant stabilized nanoparticles on aqueous subphase*

The air-water interface has been used for the assembly of nanoparticles synthesized *ex-situ* in solution. This method involves three steps: 1) synthesis of colloidal particles in the aqueous phase, 2) hydrophobization of aqueous colloidal particles by phase transfering them to organic phase using suitable phase transfer agent 3) spreading

of hydrophobized nanoparticles (monolayer protected clusters, MPCs) on aqueous subphase in a Langmuir trough and formation of their mono/multilayers onto suitable substrates using LB technique. Fendler's group has shown the formation of compact, ordered arrays of MPCs of silver [51], platinum [52], palladium [52] CdS [53], lead zirconium titanate [54] Fe_2O_3 [55], TiO_2 [56] and Other groups have also employed this technique to form superlattices of C_{60} molecules [57], silver [58], gold [59], Pt [60] and CdS [61] nanoparticles stabilized with different passivating agents. Apart from spherical nanoparticles, the 2D assembly of anisotropic nanostructures such as silver nanowires, which serve as excellent substrates for surface-enhanced Raman spectroscopy [62] and barium chromate nanorods [63] has also been demonstrated by this technique.

1.2.8-3 *Reduction of metal ions under Langmuir monolayer*

Apart from assembly of nanoparticles synthesized *ex-situ*, the air-water interface has also been used for *in-situ* synthesis of nanoparticles and their consequent assembly. Metal and semiconductor nanocrystals were grown under suitable Langmuir monolayers via the slow infusion of reactant gas (reducing agent) into the closed environment surrounding a trough containing the monolayer-coated aqueous precursor metal ion solution subphase. Formation of nanoparticulate films of cadmium sulphide [64], lead sulphide [64,65] zinc sulphide [65], and cadmium selenide [66] has been established by this technique. The presence of well-packed, negatively charged monolayers is an essential requirement for the *in-situ* formation of semiconductor particles. Negative charges, available in high density at the surfactant headgroup-aqueous subphase interface, effectively concentrate cations from the aqueous subphase. Slow infusion of reactant gas results in the formation of covalent metal-sulfide bonds at the monolayer interface. Nascent metal sulphide nuclei rapidly grow to aligned microclusters. With continued infusion of reactant gas, the microclusters coalesce, predominantly two dimensionally, at the monolayer interface to an interconnected semiconductor particulate film. The residual ions (e.g. sulphide and/or bisulphide ions), produced in the aqueous subphase from reactant gas, adsorb onto the surface of the initially formed semiconductor particulate film and attract metal cations in high local concentrations which, in turn, act as seed for

the formation of a new set of clusters and semiconductor particles. These particles loosely interconnect and form additional layers of porous semiconductor particulate films. The thickness of monolayer-supported semiconductor particulate films increases to a plateau value beyond which no additional semiconductor particle formation could be observed. Selected area electron diffraction and synchrotron X-ray studies in case of lead sulphide [65] and cadmium sulphide [64] nanoparticulate films, confirm that the crystals grow epitaxially with respect to the monolayer. Factors such as nature of the surfactant, surface pressure and the temperature affect the morphology of the nanocrystallites formed under the monolayer. A similar strategy was also shown to be applicable for the generation of silver [67] and gold [68] nanoparticulate films under suitable surfactant monolayers.

1.2.8-4 *Chemical/photochemical generation of nanoparticles within Langmuir-Blodgett films*

In this method, spreading a fatty acid Langmuir monoalyer on the surface of aqueous metal ion solution subphase results in the formation of precursor metal carboxylates at the air-water interface. The LB film with incorporated metal ions deposited on suitable substrate is then exposed to suitable reactant gas (reducing agent) in a sealed cell to form the nanoparticles. Almost molecular level ordering of the reacting ions in the LB films ensure accurate control over the nanoparticles size in addition to stabilization of the nanoparticles by the lipid bilayers. Reports on the synthesis of nanoparticles in LB matrices include photoreduction of gold ions complexed with octadecylamine/hexadecylaniline [69], synthesis of size quantized CdS [70], PbS [71] and CdSe [72], CdTe [73] nanoparticles by exposure of the film to H_2S (or H_2Se, H_2Te respectively).

1.3   Various methods for generation of different anisotropic nanostructures

1.3.1 Template directed synthesis

Template directed synthesis is one of the extensively used approaches for making anisotropic nanostructures. In this approach the template simply serves as a scaffold within (or around) which a desired material is deposited or generated *in-situ* and shaped into a nanostructure with its morphology complementary to that of the template. When

the template is only involved physically, it is often selectively removed using post-synthesis treatment (such as chemical etching and calcination) in order to collect the resultant nanostructure. In a chemical process, the template is usually consumed as the reaction proceeds and it is possible to directly obtain the nanostructures as a pure product. Template directed synthesis is simple, high-throughput and cost effective procedure that also allows the complex topology present on the surface of the template to be duplicated in a single step. Variety of templates have been successfully demonstrated by different research groups for generating anisotropic nanostructues, a few of them are discussed below.

1.3.1-1 *Templating against porous materials*

Channels in porous materials contribute an important class of template used in the synthesis of 1D nanostructures. Polymer films containing track-etched channels and anodically etched alumina films are the two types of membranes generally used. Polymer films contain randomly scattered pores across the membrane surface while alumina films usually have hexagonally packed 2D array of cylindrical pores with a relatively uniform size. The desired material can be loaded into the pores using vapor-phase sputtering, liquid-phase injection or solution-phase chemical or electrochemical deposition. Synthesis of arrays of Au [74] and Ag [74] nanotubes by absorption of respective metal ion solution by capillary interaction into the pores of alumina membrane followed by drying and decomposition of salt at higher temperature has been demonstrated. Rubinstein and coworkers have shown that self sustained 'nanotubes' of Au and Ag which preserve nanoparticles morphology can be obtained by assembly of nanoparticles on the pore walls of silane treated alumina membrane accompanied by their room temperature coalescence [75]. Use of polycarbonate membrane for the preparation of Au and Ag nanorods is also reported in the literature [76]. Further, in addition to macroporous membrane, mesoporous silica has also been exploited as template for the development of highly ordered mesostructured nanowires and nanowire arrays [77]. Recently, Fitzmaurice and coworkers have shown how multiwalled carbon nanotubes can

serve as a template for assembly of gold nanoparticles, which ultimately leads to nanowire formation [78].

1.3.1-2 *Templating against features on solid substrate*

The microstructures that could be conveniently patterned on the surface of solid substrate using lithography and etching could be exploited as templates to fabricate 1D nanostructures of various materials. For example, Penner and co-workers have demonstrated the growth of Au, Ag, Pd and Cu nanowires by templating against the steps present on a highly oriented, pyrolytic graphite using electrodeposition [79]. A salient feature of this method is that continuous thin nanowires with lengths up to hundreds of micrometers could be routinely prepared as parallel arrays on the surfaces of solid supports that could be subsequently released into the free-standing form or be transferred onto the surfaces of other substrates.

1.3.1-3 *Templating against preformed nanostructures*

Templating against nanostructures (anisotropic), pre-synthesized using other methods provides a generic and powerful approach to bring in anisotropy in nanostructures. With this simple approach, Xia and co-workers have synthesized highly crystalline nanotubes of metals such as Au, Pt and Pd via galvanic displacement reaction between Ag nanowires and appropriate precursors of these metals in the aqueous medium [80]. In this process when silver nanowires are dispersed into an aqueous $HAuCl_4$ solution, are immediately oxidized to silver ions. The resultant Au atoms are confined to the vicinity of the template surface. Once their concentration reaches a critical value, the Au atoms nucleate and grow into small clusters, and eventually evolve into a sheath-like structure around the silver template. Following similar approach, Mirkin's group has examined Ag nanoprisms as templates for synthesis of triangular nanoframes of gold and silver [81] while Yang and co-workers have demonstrated the formation of Au, Ag, Pt and Pd nanowires using $LiMo_3Se_3$ as reducing and sacrificing template [82].

1.3.1-4 *Templating against DNA*

DNA is an interesting biomaterial used as a template to generate nanowires. First step of this process involves assembly of precursor metal ions into linear arrays through

the interaction between functional side groups of DNA and the metal ions. In next step, these metal ions are reduced to form string of nanoparticles along the backbone of each DNA molecule, which are further connected to generate continuous nanowires. For instance, nanowires of Au [83], Ag [84], Pt [85] and Pd [86] have been successfully produced by this method.

1.3.1-5 *Templating against polymeric material*

Block copolymers/polymers provide another class of versatile template for generating anisotropic nanostructures. Under appropriate conditions, different segments of block copolymer form regular arrays of cylinders with a structure similar to that of self-assembled surfactants. Different regions of the arrayed structure can be easily designed with functional groups to selectively interact with the precursor metal ions through physical adsorption or chemical bonding, subsequent reduction of which results in 1D nanostructures. This templating procedure has been exploited for the synthesis of Ag nanowires [87] Au nanowires and nanosheets [88] using range of copolymers. In a recent study, Schatz and co-workers have observed that Ag nanodisks could be obtained using polystyrene mesospheres as template [89].

1.3.2 Solution phase methods based on capping reagents

It is now well understood that one can control the shape of a crystal by introducing appropriate capping reagents to change the free energies of the various crystallographic surfaces and thus to alter their growth rates. Range of compounds have been evaluated as capping reagents to control the shape of colloidal particles synthesized using solution-phase methods and are discussed below:

1.3.2-1 *Polyol method*

A solution phase approach has been demonstrated by Xia and coworkers for the large-scale synthesis of silver nanowires [90]. The process involves reduction of silver nitrate ($AgNO_3$) with ethylene glycol (EG) in the presence of poly(vinyl pyrrolidone) (PVP), called polyol process. The first step of this process is the formation of Pt (or Ag) nanoparticles by reducing $PtCl_2$ (or $AgNO_3$) with EG at high temperature. It is believed that these Pt (or Ag) nanoparticles serve as seeds for the heterogeneous nucleation and

growth of silver (formed by reducing $AgNO_3$ with EG) because of their close match in crystal structure and lattice constants. In the presence of PVP, the growth of silver is directed into a highly anisotropic mode to form uniform nanowires with high aspect ratio as high as ~ 1000. It has been verified that the morphology and aspect ratios of silver nanostructures could be varied from nanoparticles and nanorods to long nanowires by adjusting the reaction conditions, including the ratio of PVP to $AgNO_3$, reaction temperature, and seeding conditions. Mechanistic aspects of this study reveal that the PVP molecules interact more strongly with (100) planes than that with (111) planes of silver maintaining the anisotropic growth [90a]. Recently it has been observed by Xia's group that the slight modification in the standard polyol synthesis by addition of sodium chloride to the reaction mixture results in other morphologies of silver nanostructures such as cubes and tetrahedrons with truncated corners/edges [91]. On the other hand, Liz-Marzan and coworkers have reported the ability of N,N-dimethyl formamide (DMF), to reduce Ag^+ ions so that Ag nanoprisims can be synthesized using PVP as a stabilizer [92]. In this case, DMF plays role of solvent as well as reducing agent like EG in the above cases. Apart from silver, polyol synthesis method has also been utilized for anisotropic nanostructure growth of other metals such as gold [93] and platinum [94].

1.3.2-2 *Seed mediated growth method*

The synthesis of gold nanorods/wires with relatively high aspect ratios by aqueous seeded growth method has been established by Murphy's group [13e,95]. The synthesis relies on the reduction of metal salt by a weak reducing agent in the presence of preformed metallic seed particles. A systematic study reveals that the nanorod dimension is influenced by various parameters such as concentration and size of seed, concentration of metal ions, ratio of concentration of seed to metal ions, concentration and nature of reducing agent, nature as well as chain length of capping agent [95f,g]. Further it has been observed that seed mediated growth in presence of NaOH (at higher pH of reaction mixture) enables quantitative production of gold nanorods of high aspect ratio [95b]. In recent studies Murphy and coworkers have found that the synthetic parameters mentioned above are highly interdependent and their different combinations give rise to various

interesting shapes like triangles, hexagons and rods [96]. Recently this method has been improved by El-Sayed's group resulting in spectacular increase in nanorod yield [97]. In addition to nanorods and nanowires, Chen and coworkers have shown that seed mediated growth process can also be employed for large-scale synthesis of silver nanoplates/nanodisks [98].

1.3.2-3 *Other methods*

Many other solution phase chemical reduction processes are reported for generation of different shape nanostructures. For example, Pileni's group has described the formation of Ag nanodisks by a soft chemical route using reverse micellar solutions [99] and has also demonstrated that tuning experimental conditions results in size-controlled Ag nanodisks with constant aspect ratio [100]. Recently, a very simple approach has been developed for the synthesis of Au nanoplates by sodium aspartate reduction of Au ions [101]. In an attempt to prepare metallic nanostructures with as clean surfaces as possible in water, Murphy and co-workers have developed a synthetic method to make silver nanowires in the absence of surfactant/polymer by citrate reduction of Ag ions in presence of sodium hydroxide. Detailed study reveals that hydroxide ion concentration is the key to produce nanowires [102]. In a very recent study made by Adachi and co-workers it has been shown that citrate reduction of $AuCl_4^-$ ion with low concentration of citrate yields Au nanowires with 2D network [103]. The formation of 2D gold nanowires in this case is induced by the small amount of reducing agent because the preliminary gold nanoparticles formed by reduction of $AuCl_4^-$ are thermodynamically unstable in the aqueous solution due to the insufficient capping of citrate [103]. Apart from chemical methods, it has been demonstrated by Sastry's group that biological systems such as lemon grass leaf extract is highly effective as reducing agent resulting in high yield of Au nanotriangles in a single step [104].

1.3.3 Electrochemical method

Wang and co-workers have developed a method for the synthesis of Au nanorods via electrochemical oxidation/reduction within a simple two-electrode type cell [13b]. The electrochemical cell comprises gold cathode and platinum anode electrodes

immersed in an electrolytic solution consisting of a shape inducing cationic surfactant, hexadecyltrimethylammonium bromide ($C_{16}TAB$), and a rod-inducing cosurfactant, tetraoctylammonium bromide (TC_8AB). The $C_{16}TAB$ serves as the supporting electrolyte as well as the stabilizer for nanoparticles to prevent their further growth. During synthesis, the bulk gold metal is converted from the anode to form gold nanoparticles most probably at the interfacial region of the cathodic surface and within the electrolytic solution. The synthesis is conducted under an ultrasonication and a controlled temperature. The ratio between the surfactants controls the average aspect ratio of the Au nanorods. In later studies, it has been shown by same group how experimental conditions can be optimized further to improve the yield and controllability of aspect ratio of Au nanorods [105].

1.3.4 Photochemical method

Recently, Yang's group has developed a new promising approach for synthesis of Au nanorods with highly controllable aspect ratio using a photochemical method [106]. The synthesis strategy involves reduction of Au ions by irradiation with UV light in presence of surfactants, $C_{16}TAB$ and TC_8AB and different amounts of silver ions. In yet another approach it has been shown by Schatz and co-workers [107] and also by Mirkin and co-workers [107] that light can be used to transform spherical colloidal silver nanoparicles into nanoprisms. In a recent study, by Callegari et al., have shown that during photoinduced conversion of silver nanospheres, the wavelength of light used plays an important role in controlling particle size and shape of resulting nanostructure [108].

1.4 Methods used in the present work

The work involved in this thesis discusses the use of the air-water interface for the large-scale 2D assembly of nanoparticles and formation of anisotropic nanostructures using the Langmuir-Blodgett (LB) technique. An important aspect of the work is that new protocols have been developed for the synthesis of anisotropic gold nanostructures, which involve constrained growth of the nanocrystals within the confined plane of the Langmuir monolayer. These protocols are different from existing air-water interface wet-chemistry methods where the role of the Langmuir monolayer is passive and the growth zone is

much more delocalized since metal ions electrostatically bound to Langmuir monolayer are reduced using external reducing agent either at the interface [64-68] or after deposition onto the substrate [69-73].

The thesis consists of six chapters. Chapter one is a brief introduction to the thesis and is followed by chapter two which describes the physical principles of different characterization techniques that are extensively used for the characterization of Langmuir-Blodgett films of nanomaterials. It includes Langmuir-Blodgett (LB) technique, Quartz Crystal Microgravimetry (QCM), UV-visible Spectroscopy, Fourier Transform Infrared Spectroscopy (FTIR), X-ray diffraction (XRD), Transmission Electron Microscopy (TEM), X-ray Photoelectron Spectroscopy (XPS), and contact angle measurements. Applications of these techniques to understand various aspects of formation of LB films of nanoparticles have been summarized.

The third chapter deals with the synthesis of hydrophobized (water insoluble) gold and silver nanoparticles, their assembly at air-water interface and formation of LB films thereafter. Hydrophobization of gold and silver nanoparticles was achieved by simple phase transfer of aqueous colloidal solution to organic phase utilizing the electrostatic interaction between nanoparticle surface and long chain amine molecules present in the organic phase. Hydrophobized gold and silver nanoparticles form stable Langmuir monolayer when spread at the air-water interface leading to long range hexagonal close packed 2D ordered assembly. A salient feature of present work is that long chain fatty amines (such as octadecylamine, ODA) capped gold and silver nanoparticles can also be organized into long-range ordered arrays alternative to short-chain thiol capped nanoparticle assemblies (extensively studied systems in the literature). LB films made from ordered assemblies of nanoparticles show different optical behaviour when compared with dispersed spherical nanoparticles indicating that the interparticle-coupling phenomenon exists between the particles in the arrays. Thus, it is believed that these monolayers could be good candidates for electron-transport measurements as a function of interparticle distance, parallel to the conventional systems comprising monolayer of short-chain thiol capped nanoparticles.

In the fourth chapter, the one step synthesis of gold and silver nanostructures at the air-water interface using different reducing Langmuir monolayers has been demonstrated. It has been shown that the reduction of chloroaurate ions present in the subphase by hexadecylaniline (HDA) Langmuir monolayer results in the formation of highly anisotropic, flat, thin nanosheets of gold which are highly oriented in (111) direction (earlier it has been shown in this laboratory that the reduction of gold ions with same HDA molecule at liquid-liquid interface leads to the formation of spherical nanoparticles with no specific orientation [109]). This study reveals that any amphiphilic molecule forming stable Langmuir monolayer at air-water interface and bearing head group acting as a reducing agent, can be used for the synthesis of nanoparticles at both liquid-liquid and air-water interface. Thus, the above synthetic strategy can be generalized for the synthesis of other metal nanoparticles using appropriate Langmuir monolayer. Stepping ahead in this direction, C_{18} -alkylated tyrosine molecule has been synthesized (reduction of gold ions with tyrosine is reported in the literature [110]) and it has been shown that it behaves similar to HDA molecule at both liquid-liquid (forming spherical nanoparticles) and air-water interface (forming anisotropic, flat nanosheets). In a sense, it has been shown that the shape variation in the nanoparticles can be achieved by carrying out the reduction with the same reducing agent at two different interfaces. Further this approach has been established for the synthesis of silver nanoparticles by reduction of silver ions in the subphase, under alkaline conditions using pentadecylphenol (PDP) Langmuir monolayer. However unlike in case of gold, reduction of silver ions using PDP Langmuir monolayer results in formation of 2D assembly of spherical silver nanoparticles.

In chapter five, the intrinsic anisotropy of air-water interface for the growth of anisotropic, flat nanostructures of gold has been exploited further. Unlike in the previous case discussed in chapter four, where constrained growth of nanostructures was a consequence of restriction of reducing agent to the 2D interface, in this case the same has been accomplished by confining precursor metal ions to the air-water interface. Confinement of metal ions was achieved by hydrophobizing gold ions with surfactants

such as ODA and benzyldimethylstearylammonium chloride (BDSAC). On spreading the solution of hydrophobized metal ions on the surface of aqueous subphase containing suitable reducing agent results in synthesis of nanoparticles at the interface in a true sense. Effect on shape of the nanostructures using different surfactants for making metal ions hydrophobic formed has been discussed.

One of the important aspects of these nanostructures formed at 2D air-water interface is that they can be deposited on different substrates in layer-by-layer fashion (shown by QCM and UV-vis spectroscopy measurements), ultimately, which is the primary requirement for the realization of their potential applications.

Chapter six is brief summary of the work presented in the thesis and possible further scope for research in this area.

References:

(1)   Kerker, M. *J. Colloid Int. Sci.* **1985**, *105*, 297.

(2)   (a) Milliron, D. J.; Hughes, S.M.; Cui, Y.; Manna, L.; Li, J. W.; Lin-W.; Alivisatos, A. P. *Nature* **2004**, *430*, 190. (b) Buhro, W.E.; Colvin, V. L. *Nature Mater.* **2003**, *2*, 138. (c) Mirkin, C. A. *Inorg. Chem.* **2000**, *39*, 2258. (d) Fendler, J.H. *Membrane Mimetic Chemistry Approach to Advanced Materials* Springer-Verlag, Berlin, **1992**.

(3)   (a) Monti, O. L. A.; Fourkas, J. T.; Nesbitt, D. J. *J. Phys. Chem. B* **2004**, *108,* 1604. (b) Jin, R.; Cao, Y. C.; Hao, E.; Métraux, G. S.; Schatz, G.C.; Mirkin C. A. *Nature* **2003**, *425*, 487. (c) Schmid, G. **"*Clusters and colloids: From theory to Application*"** Weinheim: VCH. **1994**. (d) Kamat, P. V.; Meisel, D. "*Studies in Surface Science and Catalysis*" Semiconductor and Nanoclusters- Physical, Chemical, and Catalytic Aspects. Amsterdam: Elsevier **1997**.

(4)   (a) Klein, D. L.; Roth, R.; Lim, A. K. L.; Alivisatos, A. P.; McEuen, P. L. *Nature* **1997**, *389*, 699. (b) Weller, H. *Angew. Chem. Int. Ed.* **1998**, *37*, 1658. (c) Cui, J. B.; Burghard, M.; Kern, K. *Nano Lett.* **2002**, *2*, 117. (d) Bjo1rk, M. T.; Thelander, C.; Hansen, A.E.; Jensen, L. E.; Larsson, M. W.; Wallenberg, L. R.; Samuelson, L. *Nano Lett.* **2004**, *4*, 1621. (e) Liu, C.; Zapien, J. A.; Yao, Y.;Meng, Z.; Lee, C. S.; Fan, S.; Lifshitz, Y.; Lee, S. T. *Adv. Mater.* **2003**, *15*, 838.

(5)   Wang, Y. *Acc. Chem. Res.* **1991**, *24*, 133. (b) Yoffe, A. D. *Adv. Phys.* **1993**, *42*, 173.

(6)   (a) Aiken, J. D. III; Finke, R. G. *J. Mol. Cata. A* **1999**, *145*, 1. (b) Reetz, M. T.; Quaiser, S. A.; Breinbauer, R.; Teshe, B. *Angew. Chem. Int. Ed.* **1995**, *34*, 2728. (c) El-Sayed, M. A. *Acc. Chem. Res.* **2001**, *34*, 257 and references therein.

(7)   (a) Hagfeldt, A.; Graetzel, M. *Acc. Chem. Res.* **2000**, *33*, 269. (b) Bueno, J. T.; Shchukina, N.; Ramos, A. A. *Nature* **2004**, *430*, 326.

(8)   Moran, C. E.; Steele, J. M.; Halas, N. J. *Nano Lett.* **2004**, *4,* 1497.

(9)   (a) West, J. L.; Halas, N. *J. Curr. Opin. Biotech.* **2000**, *11*, 215. (b) Mornet, S.; Vasseur, S.; Grasset, F.; Duguet, E. *J. Mater. Chem.* **2004**, *14*, 2161. (c) Roy, I.;

Ohulchanskyy, T.Y.; Pudavar, H.E.; Bergey, E.J.; Oseroff, A.R.; Morgan, J.; Dougherty, T.J.; Prasad, P. N. *J. Am. Chem. Soc*. **2003**, *125*, 7860. (d) Hirsch, L. R.; Stafford, R. J.; Bankson, J. A.; Sershen, S. R.; Rivera, B.; Price, R. E.; Hazle, J. D.; Halas, N. J.; West, J. L. *PNAS* **2003**, *100*, 13549. (e) Salata, O.V. *J. Nanobiotech.* **2004**, *2*, 3.

(10)   Xia, Y.; Whitesides, G. M. *Angew. Chem. Int. Ed.* **1998**, *37*, 551.

(11)   (a) Alivisatos, A. P. *Science* **1996**, *271*, 933. (b) Kim, S.H.; Medeiros-Ribeiro, G.; Ohlberg, D. A. A.; Williams, R. S.; Heath, J. R. *J. Phys. Chem. B* **1999**, *103,* 10341. (c) Remacle, F.; Beverly, K. C.; Heath, J. R.; Levine, R. D. *J. Phys. Chem. B* **2003**, *107,* 13892. (d) Chumanov, G.; Sokolov, K.; Cotton, T. M. *J. Phys. Chem.* **1996**, *100,* 5166.

(12)   (a) Mirkin, C. A.; Letsinger, R. L.; Mucic, R. C.; Storhoff, J. J. *Nature* **1996**, *382*, 607. (b) He, L.; Musick, M. D.; Nicewarner, S. R.; Salinas, F. G.; Benkovic, S. J.; Natan, M. J.; Keating, C. D. *J. Am. Chem. Soc.* **2000**, *122*, 9071.

(13)   (a) Foss, C. A.; Hornyak, G. L.; Stockert, J. A.; Martin, C. R. *J. Phys. Chem*. **1994**, *98*, 2963. (b) Yu, Y. Y.; Chang, S. S.; Lee, C. L.; Wang, C. R. C. *J. Phys. Chem. B* **1997**, *101*, 6661. (c) Link, S.; Mohamed, M. B.; El-Sayed, M. A. *J. Phys. Chem. B* **1999**, *103*, 3073. (d) Jana, N. R.; Gearheart, L.; Murphy, C. J. *Chem. Comm*. **2001**, 617. (e) Jana, N. R.; Gearheart, L.; Murphy, C. J. *J. Phys. Chem. B* **2001**, *105*, 4065.

(14)   (a) Hu, J. T.; Li, L. S.; Yang, W. D.; Manna, L.; Wang, L. W.; Alivisatos, A. P. *Science* **2001**, *292*, 2060. (b) Huang, M. H.; Mao, S.; Feick, H.; Yan, H. Q.; Wu, Y. Y.; Kind, H.; Weber, E.; Russo, R.; Yang, P. D. *Science* **2001**, *292*, 1897.

(15)   Kottmann, J. P.; Martin, O. J. F.; Smith, D. R.; Schultz, S. *Chem. Phys. Lett*. **2001**, *341*, 1.

(16)   Thurn-Albrecht, T.; Schotter, J.; Kastle, G. A.; Emley, N.; Shibauchi, T.; Krusin-Elbaum, L.; Guarini, K.; Black, C. T.; Tuominen, M. T.; Russell, T. P. *Science* **2000**, *290*, 2126.

(17)   Li, L.; Hu, J.; Yang, W.; Alivisatos, A. P. *Nano Lett.* **2001**, *1*, 349.

(18)   (a) Hu, J. T.; Odom, T. W.; Lieber, C. M. *Acc. Chem. Res.* **1999**, *32*, 435. (b) Link, S.; El-Sayed, M. A. *J. Phys. Chem. B* **1999**, *103*, 8410.

(19)   (a) van der Kooij, F. M.; Kassapidou, K.; Lekkerkerker, H. N. W. *Nature* **2000**, *406*, 868. (b) Nikoobakht, B.; Wang, Z. L.; El-Sayed, M. A. *J. Phys. Chem. B* **2000**, *104*, 8635.

(20)   Colvin, V. L.; Goldstein, A. N.; Alivisatos, A. P. *J. Am. Chem. Soc.* **1992**, *114,* 5221.

(21)   (a) Gole, A.; Sainkar, S. R.; Sastry, M. *Chem. Mater.* **2000**, *12,* 1234. (b) Bandyopadhyay, K.; Patil, V.; Vijayamohanan, K.; Sastry, M. *Langmuir* **1997,** *13,* 5244. (c) Sastry, M. *Colloids and Colloid Assemblies: Synthesis, Modification, Organization and Utilization of Colloid Particles* ed. F. Caruso, Wiley-VCH, Berlin Chapter 12. **2003**, 369-397. (d) Sastry, M. *Handbook of Surfaces and Interfaces of Materials*, Ed. H.S. Nalwa, Nanostructured Materials, Micelles and Colloids, Academic Press**,** Volume 3, Chapter 2, **2001**, 87-119.

(22)   (a) Hutter, E.; Fendler, J. H.; Roy, D. *J. Phys. Chem. B* **2001**, *105,* 11159. (b) Doron, A.; Katz, E.; Willner, I. *Langmuir* **1995***, 11,* 1313. (c) Chan, E.W. L.; Yu, L. *Langmuir* **2002**, *18,* 311. (d) Fan, H.; Lopez, G. P. *Langmuir* **1997**, *13,* 119. (e) Park, S.; Weaver, M. J.; *J. Phys. Chem. B* **2002**, *106,* 8667. (f) Okamoto, T.; Yamaguchi, I. *J. Phys. Chem. B* **2003**, *107*, 10321. (g) He, H. X.; Zhang, H.; Li, Q.G.; Zhu, T.; Li, S. F. Y.; Liu, Z. F. *Langmuir* **2000**, *16,* 3846.

(23)   (a) Drouard, S.; Hickey, S. G.; Riley, D. J. *Chem. Comm.* **1999**, 67. (b) Jiang, P.; Liu, Z. F.; Cai, S.M. *Langmuir* **2002**, *18,* 4495. (c) Patil, V.; Mayya, K.S.; Sastry, M. *J. Mater. Sci. Lett.* **1997**, *16*, 899.

(24)   (a) Rao, C. N. R.; Kulkarni, G. U.; Thomas, P. J.; Ed-wards, P. P. *Chem. Soc. Rev.* **2000**, *29*, 27. (b) Musick, M. D.; Keating, C. D.; Keefe, M. H.; Natan, M. J. *Chem. Mater.* **1997**, *9,* 1499. (c) Murray, C. B.; Kagan, C. R.; Bawendi, M. G. *Science* **1995**, *270*, 1335.

(25)   Trou, M.; Saville, D. A.; Aksay, I. A. *Science* **1996**, *272*, 706.

(26) (a) Giersig, M.; Mulvaney, P. *J. Phys. Chem.* **1993***, 97,* 6334. (b) Giersig, M.; Mulvaney, P. *Langmuir* **1993**, *9*, 3408.

(27) Teranishi, T.; Hosoe, M.; Tanaka, T.; Miyake, M. *J. Phys. Chem. B* **1999**, *103,* 3818.

(28) Chandrasekharan, N.; Kamat, P. V. *Nano Lett*. **2001**, *1*, 67.

(29) (a) Korgel, B. A.; Fullam, S.; Connoly, S.; Fitzmaurice, D. *J. Phys. Chem. B* **1998**, *122*, 4640. (b) Harfenist, S. A.; Wang, Z. L.; Alvarez, M. M.; Vezmar, I.; Whetten R. L. *J. Phys. Chem.* **1996**, *100,* 13904. (c) Pileni, M. P. *Langmuir* **1997**, *13*, 3266. (d) Pileni, M. P. *New J. Chem*. **1998**, *22*, 693.

(30) Pileni, M. P. *J. Phys. Chem. B* **2001**, *105,* 3358.

(31) (a) Selvakannan, PR.; Mandal, S.; Pasricha, R.; Sastry, M. *J. Colloid Int. Sci*. **2004**, *279*, 124. (b) Sarathy, K. V.; Raina, G.; Yadav, R. T.; Kulkarni, G. U.; Rao, C. N. R. *J. Phys. Chem. B* **1997**, *101,* 9876. (c) Brown, L. O.; Hutchison, J. E. *J. Phys. Chem. B* **2001**, *105,* 8911. (d) He, S.; Yao, J.; Jiang, P.; Shi, D.; Zhang, H.; Xie, S.; Pang, S.; Gao, H.; *Langmuir* **2001**, *17,* 1571. (e) Zhao, S.Y.; Wang, S.; Kimura, K. *Langmuir* **2004**, *20,* 1977. (f) Stoeva, S.; Klabunde, K. J.; Sorensen, C.M.; Dragieva, I. *J. Am. Chem. Soc*. **2002**, *124*, 2305. (g) Liu, S.; Zhu, T.; Hu, R.; Liu, Z. *Phys. Chem. Chem. Phys*. **2002**, *4*, 6059.

(32) (a) Kiely, C. J.; Fink, J.; Brust, M.; Bethell D.; Schiffrin, D. J. *Nature* **1998**, *396*, 444. (b) Kiely, C. J.; Fink, J., Zheng, J. G.; Brust, M.; Bethell D.; Schiffrin, D. J. *Adv. Mater*. **2000**, *12*, 640.

(33) (a) Collier, C. P.; Vossmeyer, T.; Heath, J. R. *Ann. Rev. Phys. Chem*. **1998**, *49*, 71. (b) Wang, Z. L. *Adv. Mater*. **1998**, *10*, 13.

(34) Andres, R. P.; Bielefeld, J. D.; Henderson, J. I.; Janes, D. B.; Kolagunta, V. R. *Science* **1996**, *273*, 1690.

(35) (a) Elghanian, R.; Storhoff, J. J.; Mucic, R. C.; Letsinger, R. L.; Mirkin, C. A. *Science* **1997**, *277*, 1078. (b) Mitchell G. P.; Mirkin, C. A.; Letsinger, R. L. *J. Am. Chem. Soc*. **1999**, *121*, 8122. (c) Taton, T. A.; Mirkin, C. A.; Letsinger, R. L.

Science **2000**, *289*, 1757. (d) Storhoff, J. J.; Mirkin, C. A. *Chem. Rev.* **1999**, *99, 1849.

(36)   Alivisatos, A. P.; Johnsson , K. P.; Peng, X.; Wilson, T. E.; Loweth, C. J. *Nature* **1996**, *382*, 609.

(37)   (a) Shenton, W.; Pum, D.; Sleytr, B.; Mann, S. *Nature* **1997**, *389*, 585. (b) Bergkvist, M.; Mark, S. S.; Yang, X.; Angert, E. R.; Batt, C. A. *J. Phys. Chem. B* **2004**, *108,* 8241.

(38)   (a) Shenton, W.; Douglas, T.; Young, M.; Stubbs, G.; Mann, S. *Adv. Mater*. **1999**, *11*, 253. (b) Dujardin, E.; Peet, C.; Stubbs, G.; Culver, J. N.; Mann, S. *Nano Lett*. **2003**, *3*, 413.

(39)   (a) Hulteen, J. C.; van Duybe, R. P. *J. Vac. Sci. Tech. A* **1995**, *13,* 1533. (b) Haynes, C. L.; van Duybe, R. P.; *J. Phys. Chem. B* **2001**, *105*, 5599. (c) Hulteen, J. C.; Treichel, D. A.; Smith, M.T.; Duval, M. L.; Jensen, T.R.; van Duyne, R. P. *J. Phys. Chem. B* **1999**, *103,* 3854. (d) Haynes, C. L.; McFarland, A. D.; Smith, M.T.; Hulteen, J. C.; van Duyne R. P. *J. Phys. Chem B* **2002**, *106*, 1898. (e) Ormonde, A. D.; Hicks, E. C. M.; Castillo, J.; van Duyne, R. P. *Langmuir* **2004**, *20,* 6927.

(40)   Burmeister, F.; Schafle, C.; Matthes, M.; Bohmisch, J.; Boneberg, J.; Leiderer, P. *Langmuir* **1997**, *13*, 2983.

(41)   Zhong, Z.; Gates, B.; Xia, Y. *Langmuir* **2000**, *16,* 10369.

(42)   (a) Zhang H.; Mirkin, C.A. *Chem. Mater.* **2004**, *16,* 1480. (b) Zhang H.; Li, Z.; Mirkin, C.A. *Adv. Mater*. **2002**, *14*, 1472.

(43)   (a) Freeman, R. G.; Grabar, K. C.; Alison, K. G.; Bright, R. M.; Davis, J. A.; Guthrie, A. P.; Hommer, M. B.; Jackson, M. A.; Smith, P.C.; Walter, D. G.; Natan, M. J. *Science* **1995**, *267*, 1629. (b) Grabar, K. C.; Allison, K.J.; Baker, B. E.; Bright, R. M.; Brown, K.R.; Freeman, R. G.; Fox, A. P.; Keating, C. D.; Musik, M. D.; Natan, M. J. *Langmuir* **1996**, *12*, 2353. (c) Grabar, K. C.; Freeman, R. G.; Hommer, M. B.; Natan, M. J. *Anal. Chem*. **1995**, *67*, 735. (d) Bright, R. M.;

Walter, D. G.; Musik, M. D.; Jackson, M. A.; Allison, K.J.; Natan, M. J. *Langmuir*, **1996**,*12*, 810.

(44) Peschel, S.; Schmid, G. *Angew. Chem. Int. Ed.* **1995**, *34*, 1442.

(45) Tanaka, H.; Mitsuishi, M.; Miyashita, T. *Langmuir* **2003**, *19,* 3103.

(46) Malynych, S.; Luzinov, I.; Chumanov, G. *J. Phys. Chem. B* **2002**, *106,* 1280.

(47) Kawasaki, M.; Hori, M. *J. Phys. Chem. B* **2003**, *107,* 6760.

(48) Mayya, K. S.; Patil, V.; Sastry, M. *Langmuir* **1997**, *13,* 2575.

(49) (a) Sastry, M.; Mayya, K. S.; Patil, V.; Paranjape, D. V.; Hegde, S. G. *J. Phys. Chem. B* **1997,** *101,* 4954. (b) Mayya, K. S.; Sastry, M. *Langmuir* **1998,** *14,* 74.

(50) Mayya, K.S.; Patil, V.; Madhu Kumar P.; Sastry, M. *Thin Solid Films* **1998,** *312*, 308.

(51) Meldrum, F. C.; Kotov, N. A.; Fendler, J. H. *Langmuir* **1994***, 10,* 2035.

(52) Meldrum, F.C.; Kotov, N. A.; Fendler, J. H. *Chem. Mater.* **1995**, *7,* 1112.

(53) (a) Kotov, N. A.; Meldrum, F. C.; Wu, C.; Fendler, J. H. *J. Phys. Chem.* **1994**, *98*, 2735. (b) Tian, Y.; Fendler, J.H. *Chem. Mater.* **1996**, *8,* 969.

(54) Kotov, N. A.; Zavala, G.; Fendler, J. H. *J. Phys. Chem.* **1995,** *99,* 12375.

(55) Meldrum, F. C.; Kotov, N. A.; Fendler, J. H. *J. Phys. Chem.* **1994***, 98,* 4506.

(56) Kotov, N. A.; Meldrum, F.C.; Fendler, J.H. *J. Phys. Chem.* **1994***, 98,* 8827.

(57) Ganguly, P.; Paranjape, D.V.; Patil, K.R.; Chaudhari, S. K.; Kshirsagar, S.T. *Indian J. Chem. A* **1992**, *31*, F42.

(58) (a) Wang, W.; Chen, X.; Efrima, S. *J. Phys. Chem. B* **1999,** *103,* 7238. (b) Heath, J. R.; Knobler, C. M.; Leff, D. V. *J. Phys. Chem. B* **1997**,*101*, 189.

(59) (a) Burghard, M.; Philipp, G.; Roth, S.; von Klitzing, K.; Pugin, R.; Schmid, G. *Adv. Mater.* **1998**, *10*, 842. (b) Bourgoin, J. F.; Kergueris, C.; Lefevre, E.; Palacin, S. *Thin Solid Films* **1998**, *327-329*, 515. (c) Chen, X. Y.; Li, J. R.; Jiang, L. *Nanotech.* **2000**, *11*, 108. (d) Kim, B.; Tripp, S. L.; Wei, A. *J. Am. Chem. Soc.* **2001**, *123,* 7955. (e) Brust, M.; Stuhr-Hansen, N.; Nørgaard, K.; Christensen, J. B.; Nielsen, L. K.; Bjørnholm, T. *Nano Lett.* **2001**, *1*, 189. (f) Brown, J. J.; Porter, J. A.; Daghlian, C. P.; Gibson, U. J. *Langmuir* **2001**, *17,* 7966. (g) Huang, S.;

Minami, K.; Sakaue, H.; Shingubara, S.; Takahagi, T. *Langmuir* **2004**, *20*, 2274. (h) Santhanam, V.; Andres, R. P. *Nano Lett.* **2004**, *4*, 41.

(60)　(a) Sastry, M.; Patil, V.; Mayya, K.S.; Paranjape, D.V.; Singh, P.; Sainkar, S.R. *Thin Solid Films* **1998**, *324*, 239. (b) Perez, H.; de Sousa, R.M. Lisboa; Pradeau, J.P.; Albouy, P.A. *Chem. Mater.* **2001**, *13*, 1512.

(61)　Damle, C.; Gole A.; Sastry, M. *J. Mater. Chem.* **2000**, *10*, 1389.

(62)　Tao, A.; Kim, F.; Hess, C.; Goldberger, J.; He, R.; Sun, Y.; Xia, Y.; Yang P. *Nano Lett.* **2003**, *3*, 1229.

(63)　Kim, F.; Kwan, S.; Akana, J.; Yang, P. *J. Am. Chem. Soc.* **2001**, *123,* 4360.

(64)　(a) Kyunghee, C. Y.; Fendler, J.H. *Langmuir* **1990**, *6,* 1519. (b) Yang, J.; Meldrum, F.C.; Fendler, J. H. *J. Phys. Chem.* **1995***, 99,* 5500. (c) Zhao, X. K.; Xu, S.; Fendler, J. H. *Langmuir* **1991**, *7*, 520. (d) Zhao, X. K.; Fendler, J. H. *Chem. Mater* **1991,** *3,* 168. (e) Zhao, X. K.; Fendler, J. H. *J. Phys. Chem.* **1991**, *95,* 3716. (f) Zhao, X. K.; McCormick, L. D.; Fendler, J. H. *Chem. Mater.* **1991**, *3*, 922. (g) Yuan, Y.; Cabasso, I.; Fendler, J.H.; *Chem. Mater.* **1990**, *2*, 226. (h) Yang, J.; Meldrum, F.C.; Fendler J. H. *J. Phys. Chem.* **1995***, 99,* 5500.

(65)　(a) Zhao, X. K.; Yang, J. L.; McCormick, D.; Fendler, J. H. *J. Phys. Chem.* **1992***, 96,* 9933. (b) Yang, J.; Fender, J. H. *J. Phys. Chem.* **1995***,99,* 5505.

(66)　Zhao, X. K.; McCormick, L.D.; Fendler J. H. *Langmuir* **1991**, *7,* 1255.

(67)　Yi, K. C.; Horvolgyi, Z.; Fendler, J. H. *J. Phys. Chem.* **1994**, *98*, 3872.

(68)　Yi, K. C.; Mendieta, V. S.; Castaiiares, R.L.; Meldrum, F.C.; WU, C.; Fendler, J. H. *J. Phys. Chem.* **1995***, 99,* 9869.

(69)　Ravaine, S.; Fanucci, G. E.; Seip, C.T.; Adair, J. H.; Talham, D.R. *Langmuir* **1998**, *14*, 708.

(70)　(a) Smotkin, E. S.; Lee, C.; Bard, A. J.; Campion, A.; Fox, M. A.; Mallouk, T. E.; Webber, S. E; White, J. M. *Chem. Phys. Lett.* **1988**, *152*, 265. (b) Ceddes, N. J.; Urquhart, R. S.; Furlong, D. N.; Lawrence, C. R.; Tanaka, K.; Okahatas, Y.; *J. Phys. Chem.* **1993***, 97,* 13767. (c) Urquhart, R. S.; Furlong, D. N.; Mansur, H.;

Grieser, F.; Tanaka, K.; Okahatat, Y. *Langmuir* **1994**,*10*, 899. (d) Peng, X.; Lu, R.; Zhao, Y.Y.; Qu, L.; Chen, H.; Li T. *J. Phys. Chem.* **1994**, *98,* 7052.

(71) (a) Peng, X.; Guan, S.; Chai, X.; Jiang, Y.; Li, T. *J. Phys. Chem.* **1992**, *96,* 3170. (b) Zhu, R.; Min, G.; Wei, Y. *J. Phys. Chem.* **1992**, *96,* 8210.

(72) Urquhart, R. S.; Furlong, D. N.; Gengenbach, T.; Geddes, N. J.; Griesert, F. *Langmuir* **1996**, *11*, 1127.

(73) Grieser, F.; Furlong, D. N.; Scoberg, D.; Ichinose, I.; Kimizuka, N.; Kunitake, T. *J. Chem. Soc. Faraday Trans*. **1992**, *88*, 2207.

(74) (a) Qu, L.; Shi, G.; Wu, X.; Fan, B. *Adv. Mater*. **2004**, *16*, 1200. (b) Hou, S.; Harrell, C. C.; Trofin, L.; Kohli, P.; Martin, C. R. *J. Am. Chem. Soc.* **2004**, *126*, 5674. (c) Go1ring, P.; Pippel, E.; Hofmeister, H.; Wehrspohn, R. B.; Steinhart, M.; Go1sele, U. *Nano Lett*. **2004**, *4*, 1121. (d) Choi, J.; Sauer, G.; Nielsch, K.; Wehrspohn, R.B.; Go¨sele, U. *Chem. Mater.* **2003**, *15,* 776.

(75) Lahav, M.; Sehayek, T.; Vaskevich, A.; Rubinstein, I. *Angew. Chem. Int. Ed*. **2003**, *42*, 5576

(76) Cepak, V. M.; Martin, C. R. *J. Phys. Chem. B* **1998**, *102,* 9985.

(77) Wu, Y.; Livneh, T.; Zhang, Y. X.; Cheng, G.; Wang, J.; Tang, J.; Moskovits, M.; Stucky, G. D. *Nano Lett.* **2004**, *4*, 2337.

(78) Sainsbury, T.; Fitzmaurice, D. *Chem. Mater.* **2004**, *16,* 2174.

(79) (a) Penner, R. M. *J. Phys. Chem. B* **2002**, *106,* 3339. (b) Walter, E. C.; Murray, B. J.; Favier, F.; Kaltenpoth, G.; Grunze, M.; Penner, R. M. *J. Phys. Chem. B* **2002**,*106*, 11407.

(80) (a) Sun, Y.; Mayers, B. T.; Xia, Y. *Nano Lett*. **2002**, *2*, 481. (b) Sun, Y.; Xia, Y. *J. Am. Chem. Soc*. **2004**, *126*, 3892.

(81) Me´traux, G. S.; Cao, Y. C.; Jin, R.; Mirkin, C. A. *Nano Lett*. **2003**, *3*, 519.

(82) Song, J. H.; Wu, Y.; Messer, B.; Kind, H.; Yang, P. *J. Am. Chem. Soc.* **2001,** *123,* 10397.

(83)   (a) Patolsky, F.; Weizmann, Y.; Lioubashevski, O.; Willner, I. *Angew. Chem. Int. Ed*. **2002**, *41*, 2323. (b) Keren, K.; Gilad, K.R.; Yoseph, G. B.; Sivan, U.; Braun, E. *Science* **2002**, *297*, 72.

(84)   Braun, E.; Eichen, Y.; Sivan, U.; Yoseph, G. B. *Nature* **1998**, *391*, 775.

(85)   Ford, W. E.; Harnack, O.; Yasuda, A.; Wessels, J. M. *Adv. Mater*. **2001**, *13*, 1793.

(86)   Deng, Z.; Mao, C. *Nano Lett*. **2003**, *3*, 1545.

(87)   (a) Zhang, D.; Qi, L.; Ma, J.; Cheng, H. *Chem. Mater*. **2001,** *13,* 2753. (b) Cornelissen, J. J. L. M.; Heerbeek, R. V.; Kamer, P. C. J.; Reek, J. N. H.; Sommerdijk, N. A. J. M.; Nolte, R. J. M. *Adv. Mater*. **2002**, *14*, 489.

(88)   (a) Kim, U. K.; Cha, S. H.; Shin, K.; Jho, J. Y.; Lee, J. C. *Adv. Mater.* **2004**, *16*, 459. (b) Djalali, R.; Li, S.Y.; Schmidt, M. *Macromolecules* **2002**, *35,* 4282.

(89)   Hao, E.; Kelly, K. L.; Hupp, J. T.; Schatz, G. C. *J. Am. Chem. Soc*. **2002**, *124*, 15182.

(90)   (a) Sun, Y.; Mayers, B.; Herricks, T.; Xia, Y. *Nano Lett*. **2003**, *3*, 955. (b) Sun, Y.; Yin, Y.; Mayers, B. T.; Herricks, T.; Xia, Y. *Chem. Mater.* **2002**, *14,* 4736. (c) Sun, Y.; Gates, B.; Mayers, B.; Xia, Y. *Nano Lett.* **2002**, *2*, 165. (d) Sun, Y.; Xia, Y. *Adv. Mater.* **2002**, *14*, 833.

(91)   Wiley, B.; Herricks, T.; Sun, Y.; Xia, Y. *Nano Lett*. **2004**, *4*,1733.

(92)   Santos, I. P.; Liz-Marzan, L. M. *Nano Lett*. **2002**, *2*, 903.

(93)   Kim, F.; Connor, S.; Song, H.; Kuykendall, T.; Yang, P. *Angew. Chem. Int. Ed*. **2004**, *43*, 3673.

(94)   (a) Chen, J.; Herricks, T.; Geissler, M.; Xia, Y. *J. Am. Chem. Soc.* **2004**, *126*, 10854. (b) Herricks, T.; Chen, J.; Xia, Y. *Nano Lett*. **2004**, *4*, 2367.

(95)   (a) Sau, T. K.; Murphy, C. J. *Langmuir* **2004,** *20,* 6414. (b) Busbee, B. D.; Obare, S. O.; Murphy, C. J. *Adv. Mater*. **2003**, *15*, 414. (d) Murphy, C. J.; Jana, N. R. *Adv. Mater*. **2002***, 14*, 80. (e) Jana, N.R.; Gearheart, L.; Murphy, C. J. *Adv. Mater*. **2001**, *13*, 1389. (f) Gao, J.; Bender, C. M.; Murphy, C. J. *Langmuir* **2003**, *19,* 9065. (g) Gole, A.; Murphy, C. J. *Chem. Mater*. **2004**, *16,* 3633.

(96)   Sau, T. K.; Murphy, C. J. *J. Am. Chem. Soc*. **2004**, 126, 8648.

(97)   Nikoobakht, B.; El-Sayed, M. A. *Chem. Mater.* **2003**, *15,* 1957.

(98)   (a) Chen, S.; Carroll, D. L. *Nano Lett*. **2002**, *2*, 1003. (b) Chen, S.; Fan, Z.; Carroll, D. L. *J. Phys. Chem. B* **2002**, *106*, 10777. (c) Chen, S.; Carroll, D. L. *J. Phys. Chem. B* **2004***, 108,* 5500*.*

(99)   Maillard, M.; Giogio, S.; Pileni, M. P. *Adv. Mater*. **2002**, *14*, 1084.

(100) Maillard, M.; Giogio, S.; Pileni, M. P. *J. Phys. Chem. B* **2003**, *107,* 2466.

(101) Shao, Y.; Jin, Y.; Dong, S. *Chem. Comm.* **2004**, 1104.

(102) Caswell, K. K.; Bender, C. M.; Murphy, C. J. *Nano Lett*. **2003**, *3*, 667.

(103) Pei, L.; Mori, K.; Adachi, M. *Langmuir* **2004**, *20,* 7837.

(104) Shankar, S. S.; Rai, A.; Ankamwar, B.; Singh, A.; Ahmad, A.; Sastry, M. *Nature Mater*. **2004**, *3*, 482.

(105) Chang, S. S.; Shih, C. W.; Chen, C. D.; Lai, W. C.; Wang, C. R. C. *Langmuir* **1999**, *15,* 701.

(106) Kim, F.; Song, J. H.; Yang, P. *J. Am. Chem. Soc*. **2002**, *124*, 14316.

(107) (a) Jin, R.; Cao, Y. W.; Mirkin, C. A.; Kelly, K. L.; Schatz, G.C.; Zheng, J. G. *Science* **2001**, *294,*1901. (b) Jin, R.; Cao, Y. C.; Hao, E.; Metraux, G. S.; Schatz, G. C.; Mirkin, C. A. *Nature* **2003**, *425*, 487.

(108) Callegari, A.; Tonti, D.; Chergui, M. *Nano Lett*. **2003**, *3*, 1565.

(109) Selvakannan, PR.; Mandal, S.; Pasricha, R.; Adyanthaya, S. D.; Sastry, M. *Chem. Comm*. **2002**, 1334.

(110) Zhou, Y. ; Chen, W. ; Itoh, H. ; Naka, K. ; Ni, Q. ; Yamane*,* H. ; Chujo, Y. *Chem. Comm*. **2001**, 2518.

C H A P T E R II

Characterization techniques

The different experimental techniques used during the course of the present work are discussed in this chapter.

The main emphasis of this thesis is the synthesis and assembly of metal nanoparticles at air-water interface and deposition of their films using Langmuir-Blodgett (LB) technique. The LB films of nanoparticles have been characterized by a host of techniques such as Quartz Crystal Microgravimetry (QCM), UV-vis spectroscopy, Fourier Transform Infrared spectroscopy (FTIR), X-ray photoemission spectroscopy (XPS), Transmission Electron Microscopy (TEM), X-ray diffraction (XRD) and contact angle measurements. A lot of other techniques have also been used. This chapter is devoted in explaining the basic principles on which different techniques are based and their application to understanding various aspects of formation of the LB films.

2.1 Langmuir Blodgett (LB) technique

LB technique is one of the most promising techniques for preparing organic thin films [1] as it enables (a) the precise control of the monolayer thickness, (b) homogenous deposition of the monolayer over large areas on almost any kind of solid substrate and (c) the possibility to make multilayer structures with varying layer composition. For the work discussed in this thesis, LB technique has been extensively used to organize the hydrophobised gold and silver nanopartiles on the surface of water and study their assembly by subsequent formation of monolayer and multilayer films on different substrates. Further this technique has also been used for the synthesis of anisotroic gold nanostructures by restricting the reduction of precursor metal ions to the two dimensional air-water interface.

Langmuir films: Langmuir films consist of surface active materials or 'surfactants' trapped at the interface between two dissimilar phases, either liquid-liquid or liquid-gas. Surfactants are molecules which are amphiphilic in nature (Fig. 2.1) and consist of a hydrophilic (water soluble) and hydrophobic (water insoluble) part. The hydrophobic part usually consists of hydrocarbon or fluorocarbon chains and the forces acting upon them are predominantly van der Waal's type ($1/r^{12}$ and $1/r^6$). While the hydrophilic part consists of a polar group (-OH, -COOH, $-NH_3^+$, $-PO_4^-(CH_2)_2NH_3^+$ etc.) and the forces acting upon them are predominantly coulomb type ($1/r^2$).
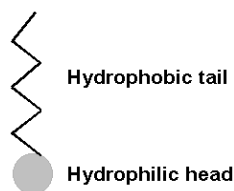
Figure 2.1 A schematic of an amphiphilic molecule showing hydrophobic (long hydrocarbon chain) and hydrophilic (polar group) parts.

Amphiphilic molecules are trapped at the intrface because they possess two very different types of bonding within the one molecular structure. The driving force behind the association is the reduction of the free energy of the system. Therefore, when a surfactant comes in contact with water it accumulates at the air-water interface causing a decrease in the surface tension of water. Many of these amphiphilic molecules insoluble in water can (with the help of a volatile and water insoluble solvent) be easily spread on a water surface with hydrophilic 'head' groups pulling the molecule into the bulk of the water and the hydrophobic 'tail' groups pointing into the air. One molecule thick surface monolayer will only be achieved if the amphiphatic balance (that is balance between hydrophilic and hydrophobic parts) of the molecule is correct. Sweeping a barrier over the water surface causes the molecules to come closer together and eventually form a compressed, ordered monolayer. The film produced by such a method is known as a Langmuir film.

Pressure-Area Isotherm (π-A isotherm): The most important indicator of the monolayer properties of an amphiphilic molecule is given by measuring the changes in surface tention upon compressing the monolayer. The reduction of surface tension is known as the surface pressure i.e. surface pressure is the lateral pressure that must be applied to prevent the film from spreading. Pressure readings are made by means of Wilhelmy plate attached to a microbalance. The plot of surface pressure versus area occupied per molecule is known as a 'pressure-area isotherm' – isotherm because compression takes place at constant temperature (Fig. 2.2). The shape of isotherm is characteristic of the molecules making up the film and hence provides a two-dimensional 'fingerprint'. π-A isotherm gives information about the stability of the molecules in the

two dimensional system, phase transitions and conformational transitions. It also gives some idea of the amount of pressure that has to be applied to the film on the sub phase, to enable deposition of the LB film in the solid-like phase. Thus at appropriate pressure, the film can be transferred to the substrate.
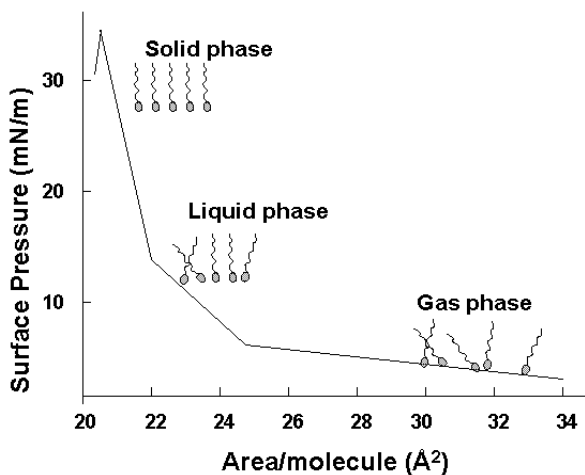
Figure 2.2   A typical pressure area (π-A) isotherm showing the various phase transitions of the floating monolayer

Deposition of LB films: Langmuir film balance can also be used for building up highly organised multilayers of the amphiphile. This is accomplished by successively dipping a solid substrate up and down through the monolayer while simultaneously keeping the surface pressure constant by a computer controlled feedback system between the electrobalance measuring the surface pressure and the barrier moving mechanism. Consequently the floating monolayer is adsorbed to the solid substrate. In this way multilayer structures of hundreads of layers can be produced. These multilayer structures are commonly called Langmuir-Blodgett or simply LB films. The LB deposition is traditionally carried out in the 'solid' phase. The surface pressure is then high enough to ensure sufficient cohesion in the monolayer so that the monolayer does not fall apart during transfer to the solid substrate. This also ensures the build up of homogeneous multilayers. The surface pressure value that gives the best results depends on the nature of the monolayer. When the solid substrate is hydrophilic (glass, SiO_2 etc.) the first layer is deposited by raising the solid substrate from the subphase through the monolayer,

whereas if the substrate is hydrophobic (HOPG, silanized SiO$_2$ etc.) the first layer is deposited by lowering the substrate into the subphase through the monolayer.

There are several parameters that affect on what type of LB film is produced. These are nature of the spread film, the subphase composition and temperature, the surface pressure during the deposition and the deposition speed, the type and nature of the solid substrate and the time the solid substrate is stored in air or in the subphase between the deposition cycles.
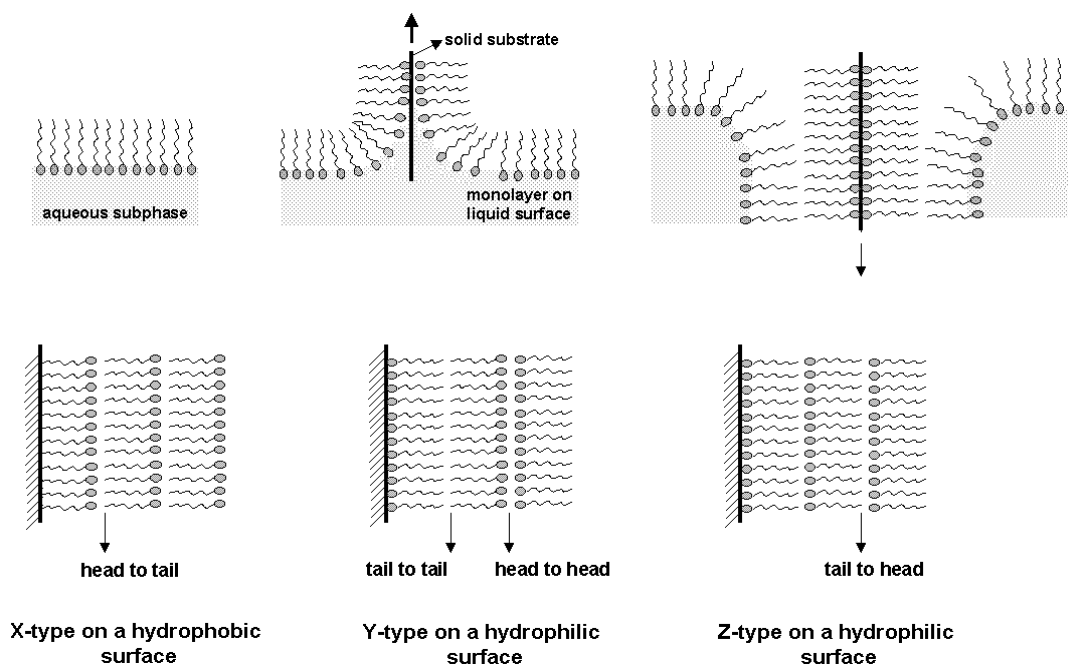
Figure 2.3 A schematic showing different types of deposition of LB films

The quantity and the quality of the deposited monolayer on a solid support is measured by a transfer ratio, given by:

$$TR = \frac{area\ of\ monolayer\ removed\ from\ the\ subphase\ at\ cons\tan t\ pressure}{area\ of\ substrate\ immersed\ in\ water}$$

For ideal transfer the TR is 1. Different kind of LB multilayers can be produced and/or obtained by successive deposition of monolayers on the same substrate. The most common type is Y-type multilayer, which is produced when the monolayer deposits to the solid substrate in both upward and downward movement of the substrate. When the monolayer deposits only during upward or downward movement, the multilayer structure

is called either Z-type or X-type (Fig. 2.3). An alternative way to deposit the monolayer is the Langmuir-Schaeffer (LS) technique. This technique differs from the vertical deposition technique described above only in the sense that the solid substrate is horizontally lowered in contact with the monolayer.

Nima LB trough, Model 611 was used for the present work. Pressure–area (π–A) isotherms were recorded at room temperature as a function of time from spreading the monolayer at a compression and expansion rate of 100 cm^2/min. A standard Wilhelmy plate was used for surface pressure sensing. Multilayer films of the nanoparticles of different thickness were formed by the LB technique at a constant surface pressure and a deposition rate of 20 mm/min with a waiting time of 180 s between dips on quartz slides, Si (111) wafers, gold-coated AT-cut quartz crystals and carbon-coated transmission electron microscopy (TEM) grids for UV–vis spectroscopy, Fourier transform infrared spectroscopy (FTIR), quartz crystal microgravimetry (QCM) and transmission electron microscopy measurements, respectively. The quartz and Si (111) substrates were hydrophobized by depositing three monolayers of lead arachidate prior to transfer of the nanoparticle monolayers. The hydrophobization of the support resulted in better transfer ratios of the nanoparticle monolayers. For the LB films grown on different substrates, monolayer transfer was observed both during the upward and downward strokes of the substrate at close to unity transfer ratio.

2.2 Quartz Crystal Microgravimetry (QCM)

Quartz crystal based microgravimetry is a powerful tool to study various adsorption processes and has been used to study adsorption of gases, self-assembled monolayers (SAMs), Langmuir-Blodgett films, nanoparticles, and biomolecules. For the work discussed in this thesis, QCM has been extensively used for calculating the exact amount of entrapped nanoparticles during layer by layer deposition of their LB films.

Working principle: One can describe the QCM to be an ultra-sensitive mass sensor. The heart of the QCM is the piezoelectric AT-cut quartz crystal sandwiched between a pair of electrodes. When the electrodes are connected to an oscillator and an AC voltage is applied over the electrodes the quart crystal starts to oscillate at its resonance frequency

due to the piezoelectric effect. This resonance frequency is sensitive to the mass changes of the crystal and its electrodes.
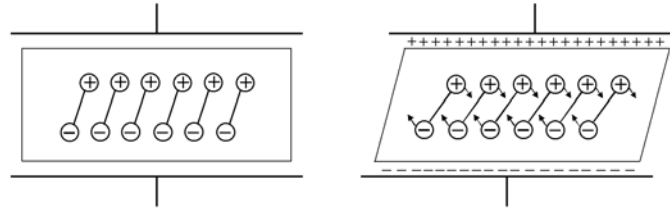

Figure 2.4 Schematic representation of the converse piezoelectric effect for shear motion.

Piezoelectric effect: In 1880, Jacques and Pierre Curie discovered that a mechanical stress applied to the surfaces of various crystals, including quartz, rochelle salt ($NaKC_4H_4O_6$-$4H_2O$) and tourmaline, afforded a corresponding electrical potential across the crystal whose magnitude was proportional to the applied stress [2]. This behaviour is referred to as piezoelectric effect; "piezo" comes from the Greek word piezen meaning to "to press". Not predicted by the Curies, the converse piezoelectric effect was later suggested by Lippman. According to the converse piezoelectric effect application of an electrical field across any piezoelectric material results in corresponding mechanical strain in it. This converse piezoelectric effect is the basis of quartz crystal microgravimetry (QCM) technique. This property only exits in materials that are acentric, viz. those crystallize in non-centrosymmetric space groups. A single crystal of an acentric material will possess a polar axis due to dipoles associated with the orientation of atoms in the crystalline lattice. When stress is applied across an appropriate direction, there is a shift of dipoles resulting from the displacement of atoms. This atomic displacement leads to a corresponding change in the net dipole moment. This will produce a net change in electrical charge on the faces of the crystal. This is depicted above in Fig. 2.4.

Application of electric field across the crystal causes a vibrational motion of the quartz crystal, with amplitude parallel to the surface of the crystal [3]. The result of the vibrational motion of the quartz crystal is the establishment of a transverse acoustic wave that propagates across the thickness of the crystal, reflecting back into the crystal at the surfaces. When a uniform layer of foreign material is added to the surface of the quartz

crystal, the acoustic wave will travel across the interface, and will propagate through the layer as shown in Fig. 2.5. This leads to decrease in the frequency of the crystal. The Frequency changes on deposition of the film can be converted to mass loading using the Saurbrey formula [4].
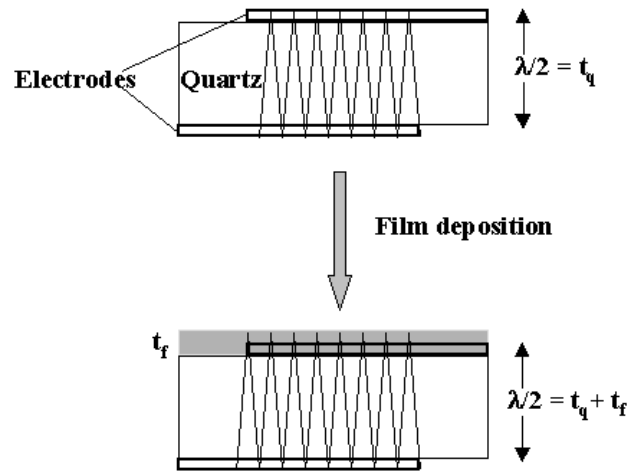
Figure 2.5 Schematic representation of the transverse shear wave in a quartz crystal and a composite resonator comprising the quartz crystal and a layer of a foreign material

Saurbrey formula

$$\Delta f = -2f_0^2 \ \frac{\Delta m}{A \ x \ (\mu_q \ x \ \rho_q)}$$

where, Δf - frequency shift, f_0 - frequency of the crystal prior to a mass change, Δm – mass change, A - Piezo electrically active area, ρ_q - density of quartz, μ_q - shear modulus for quartz. ($\mu_q = 2.95 \ x \ 10^{11} \ g \ cm^{-1} \ s^{-2}$, $\rho_q = 2.65 \ g/cm^3$).

Why AT-cut Quartz Resonators?

Although a 20 of the 32 crystal systems lack a center of inversion and can exhibit piezoelectricity, the most commonly used piezoelectric material is crystalline α quartz (SiO_2). The advantage of using quartz over other crystals is that it is a completely oxidized material and insoluble in water. It can also resist temperatures up to 579 ^0C still maintaining its piezoelectricity. Only quartz provides the unique combination of

mechanical, electrical, chemical and thermal properties that has led to its commercial significance. Crystals cut with the proper angles with respect to the crystalline axes exhibit shear displacements. Depending on the cut angle, a large number of different resonator types such as thickness-shear mode, plate and flexural resonators can be obtained from a mother crystal with eigen frequencies ranging from $5 \times 10^2 - 3 \times 10^8$ Hz. Generally AT-cut quartz crystals are used for QCM purposes in which thin quartz wafer is prepared by slicing a quartz rod at an angle of 35.25^0 with respect to the X-axis of the crystal, resonates in the *thickness shear mode*. AT cut quartz crystals exhibit a high frequency stability of $\Delta f/f \sim 10^{-8}$, which makes them well suited for many electronic devices. Since AT-cut quartz crystals have a temperature coefficient that is almost zero between 0-50 ^{0}C, this particular cut is the most suitable one for QCM sensors.

In the work described in this thesis we have used a gold coated AT-cut 6 MHz quartz crystal. The frequency counter used was an Edwards FTM5 instrument operating at a frequency stability and resolution of ± 1 Hz. At this resolution and the type of quartz crystal used, the mass resolution would be 12 ng/cm^2. Different thickness LB films of nanoparticles were deposited on the QCM crystals and the frequency changes were measured *ex situ* after drying (in flowing nitrogen) of the crystals. The frequency changes were converted to a mass uptake by using the standard Saurbrey formula [4]. The Sauerbrey equation does not apply for thick films, viscous liquids, elastic solids and viscoelastic bodies. Most reported QCM investigations have assumed ideal rigid behavior and no slip at the resonator-fluid boundary while using the Sauerbrey equation [5]. These assumptions are valid when dealing with studies on inorganic thin films, wherein the film deposited is rigid enough to be considered "quartz like". However while dealing with LB films that are being intercalated nanoparticles, one would need to consider factors such as viscoelastic effects, high mass loadings, surface roughness, surface stress, interfacial slippage and non uniform mass distribution in any piezoelectric measurement [5]. The thin films (about 250 Å), low mass loadings (about 6-12 µg) as compared to total weight of the crystal, and assuming uniform mass distribution over the film surface supports the validity of the use of Sauerbrey equation in our case.

2.3 Uv-vis spectroscopy

Theory The total energy of a molecule is the sum of its electronic energy, vibrational energy and rotational energy. The magnitude of these energies decreases in the following order: E_{elec}, E_{vib} and E_{rot}. Energy absorbed in the UV region produces changes in the electronic energy of the molecule resulting from transitions of valence electrons in the molecule. The relationship between the energy absorbed in an electronic transition and the frequency (ν), wavelength (λ) and wavenumber ($\bar{\nu}$) of radiation producing the transition is

$$\Delta E = h\nu = hc/\lambda = h\,\bar{\nu}\,c$$

where, h is Planck's constant, c is the velocity of light and ΔE is the energy absorbed in an electronic transition in a molecule from a low-energy state (ground state) to a high energy state (excited state). The energy absorbed is dependent on the energy difference between the ground state and the excited state; the smaller the difference in energy, the longer the wavelength of absorption. Since UV energy is quantized, the absorption spectrum arising from a single electronic transition should consist of a single, discrete line. A discrete line is not obtained since electronic absorption is superimposed on rotational and vibrational sublevels as shown in Fig. 2.6. The principal characteristics of an absorption band are its position and intensity. The position of an absorption band correspond to the wavelength of radiation whose energy is equal to that required for an electronic transition. The intensity of absorption is largely dependent on two factors: the probability of interaction between the radiation energy and the electronic system and the difference between the ground and excited state. The intensity of absorption may be expressed as transmittance (*T*), defined by

$$T = I/I_0$$

where I_0 is the intensity of the radiant energy striking the sample, and *I* is the intensity of the radiation emerging from the sample. A more convenient expression of absorption intensity is that derived from the Lambert-Beer law, which establishes a relationship between the absorbance, the sample thickness and the concentration of the absorbing species. The relationship is expressed as

$$A = abc$$

where, *A* is the measured absorbance, *a* is absorptivity , *b* is the cell-path length, and *c* is the analyte concentration.
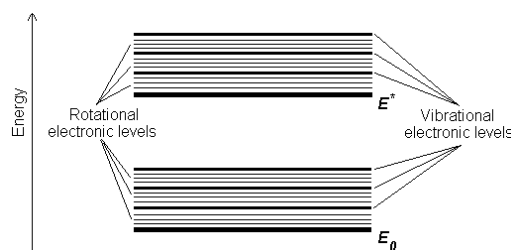

Figure 2.6 Energy level diagram of a diatomic molecule

On the other hand, light absorption by small metal particles is best described by Mie's theory [6]. The absorption spectrum of particles in a given solvent can be calculated from the optical constants of the bulk metal, although the absorption of the particles is often vastly different from that of the bulk metal itself [6]. The simplest case is when the particles are spherical and their size is small compared to the wavelength of light, and the particles are well separated in solution. At particle sizes between about 3 and 20 nm, there is not a strong dependence of the absorption spectra on particle size. This is because the particles are below the size at which higher order terms in the Mie formula for the absorption constant become significant. Thus, one has to regard only the dipole term, which depends only on the total metal concentration in the solution and not on particle size. The absorption coefficient in $mol^{-1}.L.cm^{-1}$ is calculated from the relation [6,7]

$$\alpha \;=\; \frac{18\pi}{\ln 10} \; \frac{10^{5}}{\lambda} \; \frac{Mn_{0}^{3}}{\rho} \; \frac{\varepsilon_{2}}{\left(\varepsilon_{1} \;+\; 2n_{0}^{2}\right) \;+\; \varepsilon_{2}^{2}}$$

where, λ is the wavelength of light in nanometers, M and ρ are the molecular weight and density of the metal, n_{o} is the refractive index of the solvent and ε_{1} and ε_{2} are the real and imaginary parts of the dielectric constant of the metal. When the size of the particles becomes smaller than the mean free path of the electrons, the absorption bands are broadened; this is accounted for by using size-corrected values of ε_{2} [7,8]

$$\varepsilon_2 \;=\; \varepsilon_{2(bulk)} \;+\; \left(\omega_p^2 \middle/ \omega^3\right)\;\left(V_F/R\right)$$

where ω is the light frequency, ω_p the plasmon frequency, v_F the electron velocity at the Fermi level and R the particle radius(R/vF, mean time of the free movement of the electrons). Resonance with the incident light is reached at the wavelength, where the negative value of ε_1 of the metal is equal to twice the dielectric constant of the medium. For example, gold particles possess plasmon resonances in the visible range (~514 nm). When a small spherical metallic nanoparticle is irradiated by light, the oscillating electric field causes the conduction electrons to oscillate coherently. This is schematically pictured in Fig.2.7.
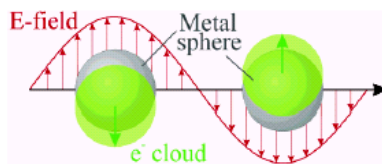
Figure 2.7 Polarization of a spherical metal particle by the electrical field vector of the incoming light

When the electron cloud is displaced relative to the nuclei, a restoring force arises from Coulomb attraction between electrons and nuclei that results in oscillation of the electron cloud relative to the nuclear framework. The oscillation frequency is determined by four factors: the density of electrons, the effective electron mass, and the shape and size of the charge distribution [8]. The collective oscillation of the electrons is called the dipole plasmon resonance of the particle (sometimes denoted "dipole particle plasmon resonance" to distinguish from plasmon excitation that can occur in bulk metal or metal surfaces). Thus, the electron density within a surface layer, the thickness of which is about equal to the screening length of a few angstroms, oscillate, whereas the density in the interior of the particle remains constant ("surface plasmon"). Therefore, any changes in the electron density of this surface layer will lead to changes in the plasmon absorption. UV–vis spectroscopy measurements of all the samples in the present case were performed on a Jasco V-570 UV/Vis/NIR spectrophotometer operated with a resolution of 1 nm.

2.4 Fourier transform infrared spectroscopy (FTIR)

Principle The atoms in a molecule do not remain in a fixed relative position and vibrate about some mean position. Due to this vibrational motion if there is a periodic alternation in the dipole moment then such mode of vibration is infrared (IR) active. The IR region of the electromagnetic spectrum is 100 μm – 1 μm wavelength. The vibrating molecule absorbs energy only from radiation with which it can coherently interact, i.e. the radiation of its own oscillation frequency. The appearance or non-appearance of certain vibrational frequencies gives valuable information about the structure of a particular molecule. The frequency of vibration is given by the relation:

$$\nu \; = \; \frac{1}{2\pi} \; \sqrt{\frac{k}{\mu}}$$

where, k is force constant; μ is reduced mass.

Silicon is the most commonly used substrate for IR measurements, for variety of reasons. It is chemically very stable and generally not very reactive even at high temperatures. It is excellent for optical studies of deposited films in the visible region using reflection techniques. It does not have strong lattice absorption bands in the useful regions of the infrared and thus can be used for transmission studies in this region. To correct for the lattice absorption bands in silicon, a reference silicon sample is used as a reference.

Peak assignments for fatty amines from monolayer protected clusters:

C-H Stretching region The two bands at 2920 and 2850 cm^{-1} have been assigned to the antisymmetric and symmetric methylene (CH$_2$) stretching vibrations respectively and two weak bands at about 2960 and 2875 cm^{-1} to the asymmetric/degenerate and symmetric methyl (CH$_3$) stretching vibrations respectively. The position of the peaks and the increase in intensity of the methylene stretching vibrations relative to methyl stretching vibration with chain length indicates structural integrity of the molecule. More interestingly, actual peak values of the symmetric and antisymmetric CH$_2$ stretching vibrations, can be used as a sensitive indicator of the ordering of the alkyl chains. For example, Nuzzo *et al* reported that the d$^-$ and d$^+$ values for hexadecanethiolate monolayer

on gold surface appear at 2920 and 2850 cm^{-1} respectively and concluded that the number of gauche defects in the methylene chains was small [9]. Similarly Porter et al. [10] reported that monolayers with chains longer than 6 carbon atoms in the alkyl chain, were highly ordered, whereas the smaller molecules resembled the liquid state, i.e., high density of gauche defects (d$^+$ and d$^-$ - 2855 and 2924 respectively).

N-H vibrations Typical peaks for the free amine are seen at 3333 cm^{-1}. This band shifts to 3198 cm^{-1} on salt formation of primary amine [11]. NH$_3$ symmetric deformation band is observed at 1487 cm^{-1} in case of pure amine The NH$_3$ antisymmetric deformation appears in the region of 1587 cm^{-1} [12].

FTIR measurements of the LB films of nanoparticles in the present study were carried out in the diffuse reflectance mode at a resolution of 4 cm^{-1} on a Perkin-Elmer FTIR Spectrum One spectrophotometer.

2.5 Nuclear magnetic resonance spectroscopy (^{1}H NMR)

Magnetic properties of nuclei All atomic nuclei possess nuclear spin, I, which may be integral (i.e. 1,2,3 etc.) or half integral (i.e ½, 3/2, 5/2 etc.) Since nucleus possesses an electric charge, the spinning nucleus gives rise to a magnetic field whose axis coincides with the axis of spin. Thus each nucleus can be thought of being equivalent to a minute magnet having magnetic moment μ. Each nucleus with I > 0 has magnetic moment. If a magnetic nucleus is placed in a uniform magnetic field, it is found that the magnetic dipole assumes only a discrete set of orientations. The system is said to be quantized. The magnetic nucleus may assume any one of (2I + 1) orientations with respect to the direction of the applied magnetic field. Thus, a proton (I = ½) will be able to assume only one of two possible orientations that correspond to energy levels of ± μH in a applied magnetic field, where H is the strength of the external magnetic field. The transition of a proton from one possible orientation to another may be affected by the absorption or emission of a discrete amount of energy such that

$$E = h\nu = 2\mu H,$$

where ν is the frequency of electromagnetic radiation absorbed or emitted.

Unless the axis of the nuclear magnet is oriented exactly parallel or antiparallel with the applied magnetic field, there will be a certain force by the external field to so orient it. But because the nucleus is spinning the effect is that its rotatioanl axis draws out a circle perpendicular to the applied field. This motion of nucleus is called precession and is of exceptional importance in the nuclear resonance phenomenon.

Theory of nuclear resonance The precessional frequency of the spinning nucleus is exactly equal to the frequency of electromagnetic radiation necessary to induce a transition from one nuclear spin state to another. The nucler transition corresponds to a change in the angle that the axis of the nuclear magnet makes with the applied magnetic field. This change can be brought about through the application of electromagnetic radiation whose magnetic vector component is rotating in a plane perpendicular to the main magnetic field. When the frequency of the rotating magnetic field and the frequency of the precessing nucleus become equal, they are said to be in resonance, and absorption or emission of energy by the nucleus can occur.

Chemical shift If the resonance frequencies for all protons in a molecule were the same, the nuclear resonance technique would be of little use- one would observe only one peak for the compound, regardless of the number or nature of protons present. The utility of the nuclear resonance phenomenon depends on the fact that nuclear magnetic resonane frequencies are to a small degree dependent on the molecular environment of the nucleus. The surrounding electrons shield the nucleus, so the effective magnetic field felt by the nucleus is not quite the same as the applied field. Electronic shielding arises from an induced circulation of electrons about a nucleus. These circulations are induced by the applied field and are in a plane perpendicular to the applied magnetic field. They produce a magnetic field that, in the region of the nucleus, is usually in a direction opposed to the direction of the applied field. The magnitude of the induced field is directly proportional to the magnitude of the applied field. The effective magnetic field experienced by the nucleus is changed by this small local field such that

$$H_{eff} = H_0 - \sigma\, H_0$$

where, σ H_0 is the induced field owing to electronic circulations. Protons in different environments are shielded by the circulations of surrounding electrons to different extents. Hence, different values of σ H_0, each dependent on the magnitude of the applied field H_0 are obtained for different protons. Because the strength of the applied magnetic field cannot be determined to the reequired degree of accuracy, the absolute position of absorption cannot be obtained directly from the instrument. However relative proton frequencies can readily be determined. The separation of resonance frequencies of nuclei in different structural environments from some arbitrarily chosen standard is termed the chemical shift.

Proton NMR spectra of the solutions of gold nanoparticles synthesized at both liquid–liquid and air–water interfaces in the current study were recorded on a Bruker AC 200 MHz instrument and scanned in the range 0–15 ppm.

2.6 X-ray photoelectron spectroscopy (XPS)

X-ray Photoelectron Spectroscopy known as XPS has been developed from the Fifties by Professor K. Siegbahn for which he was awarded the Physics Nobel Prize in 1981. XPS is surface science technique used to study the composition and electronic state of the surface region of a sample. Since, the technique provides a *quantitative analysis of the surface composition* is sometimes known by the alternative acronym, ESCA (**E**lectron **S**pectroscopy for **C**hemical **A**nalysis).

Working Principle: XPS is based on well-known photoelectric effect (a single photon in/electron out process) first explained by Einstein in 1905. Photoelectron spectroscopy uses monochromatic sources of radiation (i.e. photons of fixed energy given by relation, E = $h\nu$). In XPS the photon is absorbed by an atom in a molecule or solid, leading to ionization and the emission of a core (inner shell) electron. The kinetic energy distribution of the emitted photoelectrons (i.e. the number of emitted photoelectrons as a function of their kinetic energy) can be measured using any appropriate electron energy analyser and a photoelectron spectrum can thus be recorded. The one way to look at the overall process of photoionization is follows :

$$A + h\nu = A^+ + e\text{-}$$
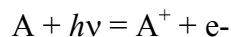
Conservation of energy then requires that:

$$E(A) + h\nu = E(A^+) + E(e\text{-})$$

Since the electron's energy is present solely as kinetic energy (KE) this can be rearranged to give the following expression for the KE of the photoelectron:

$$KE = h\nu - (\ E(A^+) - E(A)\ )$$

The final term in brackets, representing the difference in energy between the ionized and neutral atoms, is generally called the *binding energy* (BE) of the electron - this then leads to the following commonly quoted equation:

$$KE = h\nu - BE$$

the binding energies (BE) of energy levels in solids are conventionally measured with respect to the Fermi-level of the solid, rather than the vacuum level. This involves a small correction to the equation given above in order to account for the *work function* (ϕ) of the solid,

$$KE = h\nu - BE - \phi$$

Employing photons with fixed energy $h\nu$, it is obvious that if kinetic energy KE and work function ϕ of the sample are measured, it is possible to measure binding energy of electron in solid. Binding energies being characteristic of atoms, different elements present in the sample under investigation are identified. Electrons traveling through a material have a relatively high probability of experiencing inelastic collisions with locally bound electrons as a result of which they suffer energy loss and contribute to the background of the spectrum rather than a specific peak. Due to inelastic scattering process, the flux of photoelectrons emerging from the sample is much attenuated.

Why is the XPS technique surface sensitive? The soft X-rays employed in XPS penetrate a substantial distance into the sample (~ μm). Thus this method of excitation imparts no surface sensitivity at the required atomic scale. However the photoelectrons can escape from only a very short distance beneath the surface (< 100 Å). The surface sensitivity thus arises from the emission and detection of the photoemitted electrons.

Chemical shift The exact binding energy of an electron depends not only upon the level from which photoemission is occurring, but also upon:

(1) the formal oxidation state of the atom

(2) the local chemical and physical environment

changes in either (1) or (2) give rise to small shifts in the peak positions in the spectrum - so-called *chemical shifts*. Atoms of a higher positive oxidation state exhibit a higher binding energy due to the extra coulombic interaction between the photo-emitted electron and the ion core. This ability to discriminate between different oxidation states and chemical environments is one of the major strengths of the XPS technique.

The basic requirements for a XPS experiment are:

(1) x-ray source of fixed-energy radiation (usually Mg Kα with $h\nu$ = 1253.6 eV or Al Kα with $h\nu$ = 1486.6 eV)

(2) Concentric hemispherical analyser (CHA), which uses an electric field between two hemispherical surfaces to disperse the electrons according to their kinetic energy, and thereby measure the flux of emitted electrons of a particular energy.

(3) a high vacuum environment (to enable the emitted photoelectrons to be analysed without interference from gas phase collisions)

For the work described in this thesis, the XP spectra of C 1s, Au 4f, Ag 3d, and N 1s core levels were recorded from a LB film containing nanoparticles deposited on Si (111) substrate. XPS measurements were carried out on a VG Microtech ESCA 3000 instrument at a base pressure better than 1 x 10^{-9} Torr with un-monochromatized Mg Kα radiation (1253.6 eV energy). The measurements were made in the constant analyzer energy (CAE) mode at a pass energy of 50 eV and electron takeoff angle (angle between electron emission direction and surface plane) of 60°. This leads to an overall resolution of ~ 1 eV in the measurements. The chemically distinct components in the core level spectra were resolved by a non-linear least squares fitting algorithm after background removal by the Shirley method [13].

2.7 Transmission electron microscopy (TEM)

Working principle: In TEM analysis, a thin specimen is illuminated with electrons in which the electron intensity is uniform over the illuminated area. As the electrons travel through the specimen, they are either scattered by a variety of processes or they may

remain unaffected by the specimen. The end result is that a nonuniform distribution of electrons emerges from the exit surface of the specimen, that contains all the structural and chemical information about the specimen. Electron microscope is constructed to display this nonuniform distribution of electrons in two different ways.
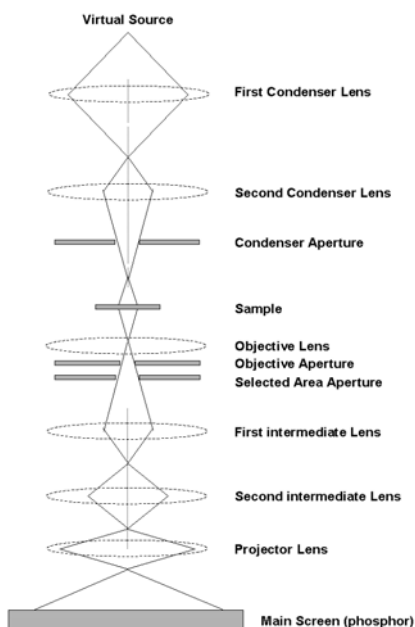
Figure 2.8 Diagram showing the various elements of the TEM instrument

Angular distribution of scattering can be viewed in the form of scattering patterns, usually called diffraction patterns, and spatial distribution of scattering can be observed as contrast in images of the specimen. The advantage of this arrangement is the possibility of directly viewing the area from which the diffraction pattern arises. The basic components of transmission electron microscope are shown in Fig. 2.8

In the present study, TEM has been used for the size determination of hydrophobised gold and silver nanoparticles drop coated onto a carbon-coated copper grid and also to study their assembly on the surface of water by depositing (vertical lifting) film from LB trough on similar grids. Further it has also been used to study the morphology of nanostructures formed at air-water interface by restricting the reduction of

metal ions to two dimensional surface. The TEM measurements were done on a JEOL model 1200EX instrument operated at an accelerating voltage of 120 kV.

2.8 X-ray diffraction (XRD)

X-ray Generation & Properties X-rays are electromagnetic radiations with typical photon energies in the range of 100 eV - 100 keV. For diffraction applications, only short wavelength x-rays (hard x-rays) in the range of a few angstroms to 0.1 angstrom (1 keV - 120 keV) are used. Because the wavelength of x-rays is comparable to the size of atoms, they are ideally suited for probing the structural arrangement of atoms and molecules in a wide range of materials. The energetic x-rays can penetrate deep into the materials and provide information about the bulk structure. X-rays are produced generally by either x-ray tubes or synchrotron radiation. In a x-ray tube, which is the primary x-ray source used in laboratory x-ray instruments, x-rays are generated when a focused electron beam accelerated across a high voltage field bombards a stationary or rotating solid target. As electrons collide with atoms in the target and slow down, a continuous spectrum of x-rays are emitted, which are termed Bremsstrahlung radiation. The high energy electrons also eject inner shell electrons in atoms through the ionization process. When a free electron fills the shell, a x-ray photon with energy characteristic of the target material is emitted. Common targets used in x-ray tubes include Cu and Mo, which emit 8 keV and 14 keV x-rays with corresponding wavelengths of 1.54 Å and 0.8 Å, respectively. (The energy E of a x-ray photon and it's wavelength is related by the equation $E = hc/\lambda$, where h is Planck's constant and c the speed of light). In recent years synchrotron facilities have become widely used as preferred sources for x-ray diffraction measurements. Synchrotron radiation is emitted by electrons or positrons travelling at near light speed in a circular storage ring. These powerful sources, which are thousands to millions of times more intense than laboratory x-ray tubes, have become indispensable tools for a wide range of structural investigations and brought have advances in numerous fields of science and technology.

Lattice Planes and Bragg's Law. X-rays primarily interact with electrons in atoms. When x-ray photons collide with electrons, some photons from the incident beam will be

deflected away from the direction where they original travel, much like billiard balls bouncing off one anther. If the wavelength of these scattered x-rays did not change (meaning that x-ray photons did not lose any energy), the process is called elastic scattering (Thompson Scattering) in that only momentum has been transferred in the scattering process. These are the x-rays that we measure in diffraction experiments, as the scattered x-rays carry information about the electron distribution in materials. On the other hand, in the inelastic scattering process (Compton Scattering), x-rays transfer some of their energy to the electrons and the scattered x-rays will have different wavelength than the incident x-rays. Diffracted waves from different atoms can interfere with each other and the resultant intensity distribution is strongly modulated by this interaction. If the atoms are arranged in a periodic fashion, as in crystals, the diffracted waves will consist of sharp interference maxima (peaks) with the same symmetry as in the distribution of atoms. Measuring the diffraction pattern therefore allows one to deduce the distribution of atoms in a material. The peaks in a x-ray diffraction pattern are directly related to the atomic distances. Fig. 2.9 shows incident x-ray beam interacting with the atoms arranged in a periodic manner as shown in 2 dimensions. The atoms, represented as spheres in the figure, can be viewed as forming different sets of planes in the crystal.
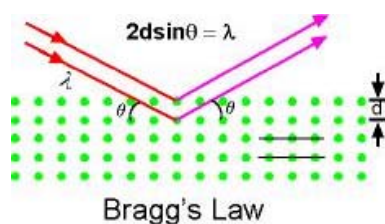
Figure 2.9 X-ray reflections from a crystal

For a given set of lattice plane with an inter-plane distance of d, the condition for a diffraction (peak) to occur can be simply written as:

$$2d \sin\theta = n\lambda$$

which is known as the Bragg's law, after W.L. Bragg, who first proposed it. In the equation, λ is the wavelength of the x-ray, θ the scattering angle, and n an integer representing the order of the diffraction peak. The Bragg's Law is one of most important

laws used for interpreting x-ray diffraction data. It is important to point out that Bragg's Law applies to scattering centers consisting of any periodic distribution of electron density. In other words, the law holds true if the atoms are replaced by molecules or collections of molecules, such as colloids, polymers, proteins and virus particles.

Powder Diffraction Powder XRD, Debye-Scherrer method is particularly used for characterizing samples in the present work. As the name suggests, the sample is usually in a powdery form, consisting of fine grains of single crystalline material to be studied. The technique is used also widely for studying particles in liquid suspensions or polycrystalline solids (bulk or thin film materials). The term 'powder' really means that the crytalline domains are randomly oriented in the sample. Therefore when the 2-D diffraction pattern is recorded, it shows concentric rings of scattering peaks corresponding to the various d spacings in the crystal lattice. The positions and the intensities of the peaks are used for identifying the underlying structure (or phase) of the material. For example, the diffraction lines of graphite would be different from diamond even though they both are made of carbon atoms. This phase identification is important because the material properties are highly dependent on structure. Powder diffraction data can be collected using either transmission or reflection geometry. Because the particles in the powder sample are randomly oriented, these two methods yield the same data.

XRD patterns of the LB films and gold nanoparticles synthesized in chloroform and solution-cast on glass substrates were recorded on a Phillips PW 1830 instrument operating at a voltage of 40 kV and a current of 30 mA with Cu-Ka radiation.

2.9 Contact angle measurements

What is contact angle? Contact angle, θ, is a quantitative measure of the wetting of a solid by a liquid. It is defined geometrically as the angle formed by a liquid at the three phase boundary where a liquid, gas and solid intersect as shown in Fig. 2.10. It can be seen from this figure that low values of θ indicate that the liquid spreads, or wets well, while high values indicate poor wetting. If the angle θ is less than 90 the liquid is said to wet the solid. If it is greater than 90 it is said to be non-wetting. A zero contact angle represents complete wetting.
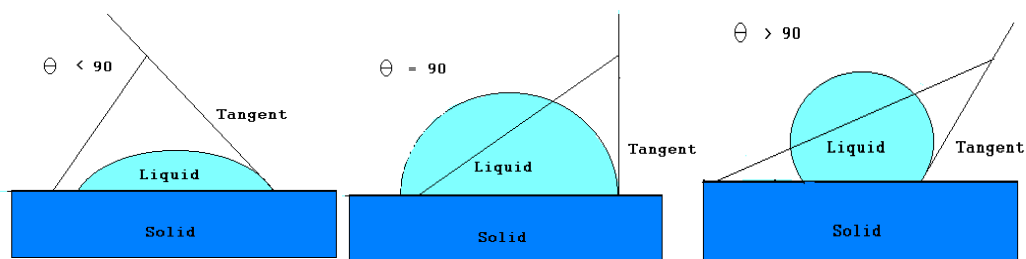
Figure 2.10 Schematic showing the different contact angles of a liquid drops on solid substrate

How is contact angle measured? Two different approaches are commonly used to measure contact angles of non-porous solids, goniometry and tensiometry. Goniometry involves the observation of a sessile drop of test liquid on a solid substrate. Tensiometry involves measuring the forces of interaction as a solid is contacted with a test liquid.

Goniometry. Analysis of the shape of a drop of test liquid placed on a solid is the basis for goniometry. The basic elements of a goniometer include a light source, sample stage, lens and image capture. Contact angle can be assessed directly by measuring the angle formed between the solid and the tangent to the drop surface. Goniometry can be used in many situations where tensiometry cannot. One can use a great variety of solid substrates provided they have a relatively flat portion for testing and can fit on the stage of the instrument. Substrates with regular curvature, such as contact lenses are also easily analyzed. Testing can be done using very small quantities of liquid. It is also easy to test high temperature liquids such as polymer melts.

In the present study contact angle measurements of a sessile water drop (1 μL) were carried out on the nanoparticle multilayer films deposited on quartz substrates using a Rame-Hart 100 goniometer.
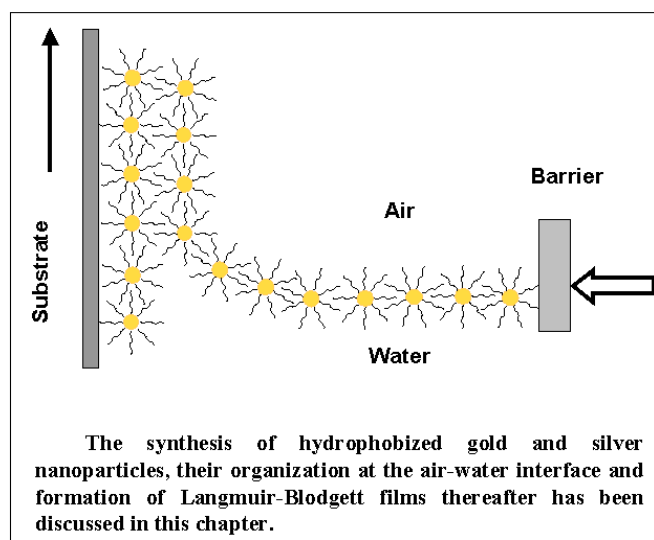
References

(1)   Ulman, A. *An introduction to Ultrathin Organic Films: from Langmuir-Blodgett to Self-Assembly*, Academic Press, San Diego, CA, **1991**.

(2)   Curie, P.; Curie, J. C. R. *Acad. Sci.* **1880**, *91*, 294.

(3)   Buttry, D. A.; Ward, M.D. *Chem. Rev.* **1992**, *92*, 1356.

(4)   Sauerbrey, G. *Z. Phys. (Munich)* **1959**, *155*, 206.

(5)   Wang, J.; Frostman, L.M.; Ward, M.D. *J. Phys. Chem.* **1992**, *96*, 5224. (b) Buttry, D. A.; Ward, M.D. *Chem. Rev.* **1992**, *92*, 1356.

(6)   Mie, G. *Ann. Phys*. **1908**, *25*, 377.

(7)   Mulvaney, P. *Langmuir* **1996**, *12*, 788. (b) Henglein, A. *J. Phys. Chem. B*. **1993**, *97, 5457.

(8)   Kelly, K. L.; Coronado, E.; Zhao, L.L.; Schatz, G. C. *J. Phys. Chem. B* **2003**, *107, 668.

(9)   Nuzzo, R.G.; Fusco, F.A.; Allara, D.L. *J. Am. Chem. Soc*. **1987**, *109,* 2358. (b) Nuzzo, R.G.; Dubois, L.H.; Allara, D.L. *J. Am. Chem. Soc*. **1990**, *112*, 558.

(10)   Porter, M.D.; Bright, T.B.; Allara, D.L.; Chidsey, C.E.D. *J. Am. Chem. Soc*. **1987**, *109*, 3559.

(11)   Bardosova, M.; Tregold, R.H.; Ali-Adib, Z. *Langmuir* **1995**, *11*, 1273. (b) Pal, S. *Ph. D thesis* University of Pune, **1996**.

(12)   Ning, G.; Guangfu, Z.; Shiquan, X. *J. Mol. Struct*. **1992**, *275*, 85.

(13)   Shirley, D. A. *Phys. Rev. B* **1972**, *5*, 4709.

C H A P T E R III

Organization of amine functionalized nanoparticles at air-water interface and formation of multilayer films using Langmuir-Blodgett technique

The synthesis of hydrophobized gold and silver nanoparticles, their organization at the air-water interface and formation of Langmuir-Blodgett films thereafter has been discussed in this chapter.

3.1 Introduction

In order to build nanodevices for practical applications the individual nanoparticles need to be assembled in a desired fashion and much current research interest lies in ordered two-dimensional (2D) assembly of nanoparticles. Of the many methods reported to prepare the 2D assembly of nanoparticles as discussed in chapter 1, the Langmuir-Blodgett (LB) technique is an important approach and efficient in template based assembly and synthesis of nanostructures. The degree of control over the molecular level organization of amphiphiles and ions that can be exercised at the air-water interface, makes LB a versatile technique. It has been shown that amphiphilic molecules at air-water interface can be used as a template for the organization of small [1] and large inorganic ions (such as polyoxometallates) [2], biological macromolecules (such as proteins, DNA) [3]. Langmuir monolayer of amphiphilic molecules has also been widely used as a template for the synthesis and assembly of nanoparticles. Fendler and coworkers were the first to show the templating action of Langmuir monolayers of amphiphilic molecules in the synthesis of nanoparticles at air-water interface. They showed that the slow infusion of H_2S into the monolayers of n-$C_{16}H_{33}C(H)[CON(H)(CH_2)_2-NH_2]_2$ [4] and arachidic acid [5] spread on the surface of aqueous $CdCl_2$ solution results in the formation of CdS nanoparticles. The method was also shown to be applicable for the formation of other semiconducting nanoparticles such as CdSe [6] and PbS [7]. Further, they extended this strategy to the synthesis of metal nanoparticles such as silver [8] and gold [9] using suitable Langmuir monolayers. Formation of silver and gold nanoparticulate films was achieved by exposing the precursor metal ion solution, coated with suitable monolayers of amphiphilic molecules to the external reducing agents such as formaldehyde (HCHO), hydrazine [8], and carbon monoxide, ultraviolet radiations [9] respectively. In all the above cases, it was observed that the nanostructures formed at the air-water interface were distinct from those formed in the subphase. The factors responsible for this are the templating action of the charged monolayer and the high concentration of the oppositely charged ions at the air-water interface (4-5 orders of magnitude higher than that in the bulk of the solution) [10].

Apart from synthesis, the air-water interface has also been used for the assembly of nanoparticles. Insofar as using the air-water interface for assembly of nanoparticles is concerned, perhaps the oldest variant was based on the assembly of hydrophobized (water-insoluble) nanoparticles and formation of multilayer films by LB technique. This involves the dispersion of hydrophobized nanoparticles in volatile solvent, their organization at air-water interface by spreading the dispersion on the surface of water and then formation of their mono/multilayers onto suitable substrates using LB technique. Based on this concept, Fendler's group has demonstrated the formation of compact, ordered arrays of monolayer protected clusters (MPCs) of silver [11], Fe_2O_3 [12], TiO_2 [13], lead zirconium titanate [14], platinum [15], palladium [15] and CdS [16]. This approach was also extensively used by others to form superlattices of C_{60} molecules [17], silver [18], gold [19], Pt [20] and CdS [21] nanoparticles stabilized with different passivating agents. Later, it was shown by Heath *et al.* that the spontaneous assembly of dodecanethiol-capped silver nanoparticles at the air-water interface results in the formation of arrays of high aspect ratio wires whose width was observed to be a function of particle size and also dependent on the nature of volatile solvent used [18b]. In a different approach, Chen and coworkers have used dithiol such as TBBT (4,4-thiobisbenzenethiol) as a bridging molecule to cross link gold nanoparticles organized at the air-water interface to achieve more rigid and long range ordered assembly of nanoparticles [22]. Brust and co-workers have recognized the possibility of linear assembly of nanoparticles resulting in the formation of nanowires at air-water interface by the organization of dodecanethiol-capped gold nanoparticles on the surface of water in the presence of the surfactant dipalmitoylphosphatidylcholine (DPPC) [23]. The unidirectional sintering of nanoparticles accompanied by packing into a mazelike structure was shown to be a templating effect of the surfactant at the molecular level [23]. Apart from spherical nanoparticles, LB technique has also been exploited for the 2D assembly of anisotropic nanostructures such as silver nanowires, which serve as excellent substrates for surface-enhanced Raman spectroscopy [24] and barium chromate nanorods [25].

All the reports available for 2D assembly of nanoparticles using LB technique, discuss the assembly of hydrophobized (organically dispersible) nanoparticles at air-water interface. The driving force for the 2D assembly here is the hydrophobic-hydrophobic interaction between the hydrophobized nanoparticles. In a different approach, it has been shown previously in this laboratory that carboxylic acid-derivatized (hydrophilic, water dispersible) colloidal particles of gold [26] and silver [27] nanoparticles can be assembled at the air-water interface using positively charged fatty amine Langmuir monolayers. Since the assembly is driven by the electrostatic interaction between the charged particles and the Langmuir monolayers the degree of cluster incorporation into the Langmuir monolayers could be well controlled by varying the charge on amine molecules through the colloidal subphase pH.

2D assemblies of gold and silver nanoparticles in particular are very widely studied systems because of their unique optical and electronic properties. Various reports available in the literature on the 2D assembly of gold and silver nanoparticles using LB technique are based on the use of alkane thiol as a passivating agent. It is well understood from these reports that the chain length of a passivating agent is one of the important parameter, which controls their properties. In most of the cases studied earlier, the molecules used for hydrophobization of the nanoparticles are alkane thiols and the hydrocarbon chain length of a passivating agent extends maximum up to C_{12} [18,19]. The bonding between surface of nanoparticle and thiol molecule is covalent in nature. However long-chain amine molecules for passivation of nanoparticles and formation of their 2D ordered assemblies have received very less attention. The amine molecules interact with the nanoparticles through electrostatic interaction and are more closely related to the biological molecules that are mainly amine functionalized or functionalized with carboxyl groups. Study with amine functionalized molecules could thus provide us with a wider range of options for surface derivatization and its ultimate biological applications. In the following sections we have disscused the synthesis and assembly of octadecyl (C_{18}) amine (ODA) capped gold and silver nanoparticles at air-water interface using versatile LB technique.

3.2 Assembly of hydrophobized gold nanoparticles at air-water interface

3.2-1 Synthesis of dodecylamine/octadecylamine capped gold nanoparticles

In a typical experiment, colloidal gold was synthesized by borohydride reduction of 10^{-4} M aqueous $HAuCl_4$ solution as described in detail elsewhere [28]. This results in a clear ruby red colloidal gold solution at pH 9 with an average particle size of 5 ± 1 nm. To 50 ml of the gold colloidal solution thus prepared, 50 ml of a 5×10^{-4} M solution of dodecylamine (DDA, $CH_3\text{-}(CH_2)_{11}\text{-}NH_2$)/octadecylamine (ODA, $CH_3\text{-}(CH_2)_{17}\text{-}NH_2$, Aldrich) in chloroform was added to form biphasic mixture of the red-colored gold hydrosol on top of the colorless organic solution. Vigorous shaking of the mixture resulted in rapid transfer (within 30 s) of the gold colloidal particles into the organic phase and this was observed by the red coloration of the organic phase (and a corresponding loss of color from the aqueous phase) when the two layers separated out. The colorless aqueous phase was then discarded, and the process of phase transfer was continued with fresh borohydride-reduced gold colloidal solution. About 1000 mL of borohydride-reduced gold colloidal solution was transferred in this way. The organic layer was then separated and rotovapped to yield a powder of hydrophobized gold nanoparticles as explained elsewhere [29]. This powder was purified by washing 4–5 times with ethanol to remove uncoordinated DDA/ODA molecules in the organic solution and dried in nitrogen atmosphere. A known amount of powder form of purified DDA/ODA-capped gold nanoparticles (DDA-Au/ODA-Au) was redispersed in chloroform and used for further experiments

3.2-2 Organization of dodecylamine/octadecylamine capped gold nanoparticles at air-water interface and formation of LB films

50 μL of 1:1 (w/w) mixture of purified hydrophobized gold nanoparticles (DDA-Au/ODA-Au) and octadecanol was dissolved in chloroform and spread on the surface of water at pH 6.5 in LB trough (water was purified by a Millipore Milli-Q system with a resistivity of 18 MΩ cm). Concentration of DDA-Au/ODA-Au in chloroform was 1 mg/mL. Addition of octadecanol was important to obtain a stable monolayer (ML) and formation of multilayer films of gold nanoparticles. Multilayer films of hydrophobized

nanoparticles were formed on different substrates according to the details given in chapter 2.

3.2-3 Gold nanoparticles hydrophobized with dodecyl amine

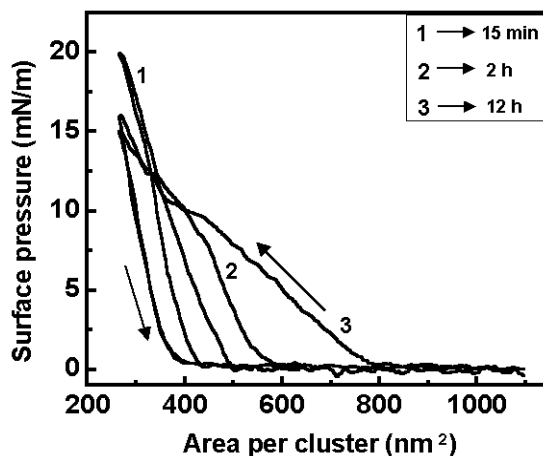### 3.2-3a *Surface pressure-area (π-A) isotherm results*

Figure 3.1 π–A isotherms recorded during one compression and expansion cycle of a 1:1 (w/w) mixture of DDA-Au nanoparticles and octadecanol as a function of time of spreading the monolayer on the surface of water.

Organization of 1:1 (w/w) mixture of hydrophobized DDA-Au nanoparticles and octadecanol in chloroform, spread on the surface of water was followed by π-A isotherm measurements as a function of time of spreading the monolayer as shown in Fig. 3.1. The upward and downward directed arrows in the isotherms indicate the compression and expansion cycles of the monolayer respectively. It is observed that the hysteresis in the π-A isotherm is small immediately after spreading the monolayer (curve 1, corresponding to time t = 15 min) and that the hysteresis increases steadily with time stabilizing after 12 h (curve 3) of spreading of the monolayer. Assuming an area/DDA molecule of 25 $Å^2$ on the surface of gold nanoparticle [29], the mass of one gold nanocluster of size 50 Å with the hydrophobic sheath is calculated to be 4.67×10^{-19} gm. From a knowledge of the concentration of the gold nanoparticles in chloroform (1mg/mL) and the amount of this solution (50 μL) spread on the surface of water, the number of clusters present on the surface of water was calculated to be 10.7×10^{13} and the area of trough was transformed into an effective area/cluster. Large expansion of the monolayer occurs as a function of

time as pressure take-off area is observed to increase from ca. 500 nm^2/cluster at time t = 15 min to ca. 800 nm^2/cluster at time t = 12 h. At time t = 15 min, the monolayer was compressible to pressure of 20 mN/m above which it collapses and after 12 h it was compressible only to a pressure of 15 mN/m. In the fully compressed state prior to collapse, average area/cluster in gold nanoparticle monolayer is 350 nm^2 as obtained from π–A isotherm measurements. Simple calculations were performed in order to understand the nature of interaction between neighboring gold nanoparticles on the surface of water. If one assumes the radius of one monolayer protected gold cluster to be the sum of the gold core (50 Å diameter, obtained from TEM results, Fig. 3.5A) and the length of the DDA molecule (1.647 nm), the area per nanoparticle at which overlap of the hydrocarbon chains between neighboring particles would occur can be shown to be ca. 54 nm^2. The length of DDA molecule was obtained from the empirical formula of Bain *et al.. l* = 0.25 nm + 0.127n nm, where n is the number of CH_2 groups, and 0.25 nm takes into account the amine and methyl terminal functional groups [30]. This area/cluster of 54 nm^2 is much smaller than the closest packing area of 350 nm^2/cluster in fully compressed state obtained from the π-A isotherm measurements presented in Fig. 3.1. Thus, it is clear that the interactions other than steric factors dominate the effects seen in the π-A isotherms. One possibility is repulsive electrostatic interactions between gold nanoparticles, which would be sufficiently long-range to account for the large take-off areas observed. The gold nanoparticles are covered by DDA molecules, which, at the pH of preparation of the hydrophobic particles at the liquid-liquid interface, would be positively charged. Thus, it is likely that the gold nanoparticles consist of a positively charged core that is masked by the hydrocarbon sheath, rendering it hydrophobic. Another important observation is the increase in takeoff area with time. We believe this could be due to the reorganization of the octadecanol molecules in the monolayer with time scales that are relatively long. One mode of reorganization could be interdigitation of the hydrocarbon chains in octadecanol and DDA molecules bound to the surface of gold nanoparticles. This process would lead to a very large tilt in the orientation of the octadecanol molecules and consequently, an increase in the monolayer area. However

this is a tentative explanation and detailed study involving x-ray reflectivity/*in-situ* ellipsometry measurements is needed for clear understanding of nature of interaction between hydrophobized gold nanoparticles on the surface of water. From the π-A isotherm measurements (Fig. 3.1), a region of large incompressibility is seen to occur up to surface pressure of ca. 15 mN/m and, therefore, multilayer films of DDA-capped gold nanoparticles of different thickness were transferred onto hydrophobized quartz substrates and gold-coated quartz crystals at this surface pressure by the LB technique for study by optical absorption spectroscopy and QCM, respectively. We would like to point out that, at this pressure, the area per DDA-Au nanocluster is roughly 290 nm^2.

It may be pointed out here that just DDA-capped gold nanoparticles in chloroform spread on the surface of water (i.e. without addition of octadecanol) did not yield uniform Langmuir monolayer. Instead they formed separate domains, which came closer during compression forming a continuous film. During deposition it was observed that the film breaks when the substrate crosses the interface resulting in very poor transfer ratio of the monolayer during successive immersion cycles. Addition of equal parts by weight of octadecanol to DDA-Au nanoparticles in chloroform facilitated the formation of stable, uniform Langmuir monolayer of hydrophobized gold nanoparticles on the surface of water (as seen from π-A isotherms, Fig. 3.1). Nonionic surfactant such as octadecanol was chosen to avoid additional electrostatic interactions, which would have been present if ionic surfactants such as stearic acid/octadecyl amine etc had been used.

3.2-3b *UV-vis spectroscopic analysis*

The advantage of organizing the nanoparticles on the surface of water is that ordered, long-range assemblies of the nanoparticles can be achieved which can subsequently be transferred to different substrates for further characterization. Optical absorption spectra of DDA-Au nanoparticle monolayer transferred from the air-water interface onto hydrophobized quartz substrates were recorded as a function of number of monolayers and are shown in Fig. 3.2A. It was observed that the intensity of optical absorption peak at 578 nm increases monotonically as a function of number of monolayers. This absorbance band is due to the excitation of surface plasmons of gold

nanoparticles present in the LB films and gives the particles their characteristic pink/purple color [31] as shown in inset of Fig. 3.2A. Indeed, the wavelength at which resonance occurs (578 nm) is considerably red-shifted with respect to the absorbance band for aqueous colloidal gold solutions, where it occurs in the range 510-525 nm.
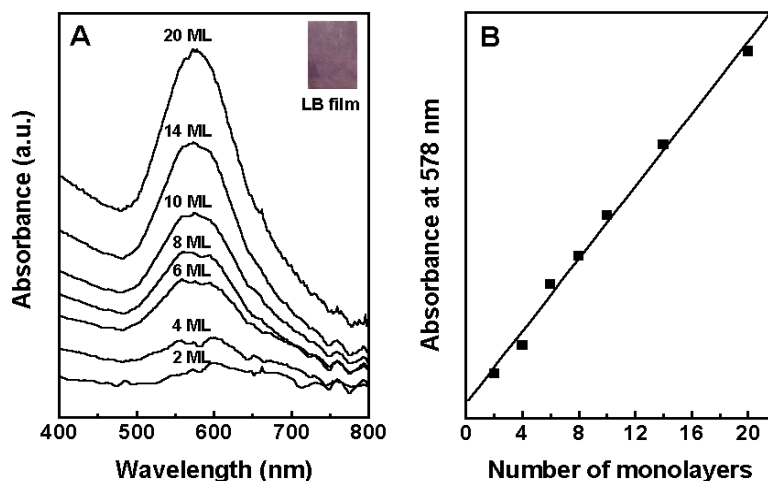

Figure 3.2 (A) UV–vis spectra recorded from LB films of DDA-capped gold nanoparticles transferred onto quartz substrate at different thickness of the film. The number of monolayers of the gold nanoparticles in the LB films is indicated next to the respective curve. Inset of the figure shows the photograph of the 20 monolayers (ML) thick LB film of gold nanoparticles deposited onto the quartz substrate. **(B)** A plot of intensity of the surface of plasmon resonance (at 578 nm) plotted as a function of number of monolayers of DDA-Au nanoparticles in LB films grown on quartz substrate. The solid line is a nonlinear least-squares fit to the data.

The shift observed in the optical spectra of the LB films can be attributed to the change in the dielectric environment of the gold nanoparticles in thin film in comparison with that where the gold nanoparticles are dispersed in solution and also to the interparticle plasmon coupling due to their close packed arrangement. The property of coupled plasmon absorbances due to close contact of optically absorbing nanoparticles has been predicted theoretically [32] and shown with a Langmuir-Blodgett film of gold nanoparticles to emerge together with a loss of electrical resistivity at interparticle separations less than about 5 nm [33]. Fig. 3.2B shows a plot of the intensity of absorbance at 578 nm as a function of the number of monolayers in the LB films for which the spectra are shown in Fig. 3.2A. A linear increase in the absorbance intensity

with number of monolayers of DDA-capped gold nanoparticles in the LB films indicates that the excellent layer-by-layer transfer of the hydrophobized gold nanoparticles had occurred.

3.2-3c *Quartz crystal microgravimety and contact angle measurements*

The mass uptake during formation of multilayers of DDA-capped gold nanoparticles by the LB technique was studied by QCM and the data obtained is shown in Fig. 3.3A. It can be seen from the QCM measurements that the mass uptake is nearly constant during each deposition. This indicates that the monolayers of gold nanoparticles are transferred onto the substrate uniformly in a layer-by-layer fashion. The solid line is a linear least square fit to the QCM data and yields a mass uptake/bilayer (corresponding to one immersion cycle of the quartz crystal in the water subphase) of 0.733 $\mu g/cm^2$. From the mass per gold nanoparticle taken together with DDA sheath (4.67×10^{-19} gm), the number of gold nanoparticles on the quartz crystal surface transferred per bilayer can be calculated to be 1.56×10^{12} per cm^2. This yields an effective area per gold nanoparticle of approximately 128 nm^2, which is lower than the area of colloidal particle of 290 nm^2 at which the colloidal particle monolayer transfer from the surface of water is effected (see discussion on π-A isotherms). This discrepancy may be due to the roughness of the QCM quartz crystal, which has not been corrected for in this case. The surface roughness factor for the crystals used in this study is ca. 2.5 [34] and would lead to an overestimation of the mass uptake of the hydrophobized gold particles in the LB films. Accounting for the roughness factor leads to a corrected area/cluster from QCM measurements of ca. 320 nm^2, which is close to that measured from the π-A isotherms. Thus, the QCM measurements show that monolayers of DDA-capped gold nanoparticles are transferred in a layer-by-layer fashion by the LB technique. We add here that QCM measurements of LB films of just DDA-capped gold nanoparticles without octadecanol gave a good monolayer transfer for the first immersion cycle alone after which very little monolayer transfer was observed for further immersions. Contact angle measurements of a sessile water drop on LB films of the hydrophobized DDA-Au nanoparticles of different thickness were done and data is shown in Fig. 3.3B. The contact angle varies from 67°

for LB film of 2 monolayers (ML) to 83° for the 14 ML film. While the film of DDA-capped gold nanoparticles does become more hydrophobic with increase in thickness, it is interesting to note that the film is still fairly hydrophilic even after depositing 14 ML.
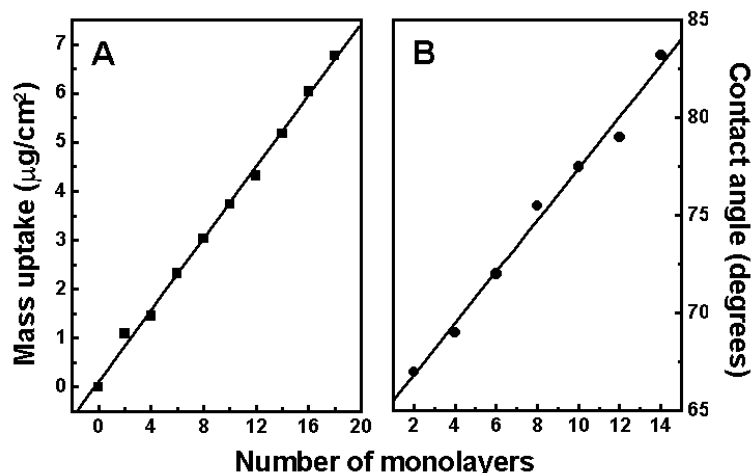

Figure 3.3 (A) QCM mass uptake data plotted as a function of number of monolayers of the DDA-capped gold nanoparticles transferred onto the AT-cut quartz crystal. The solid line is a nonlinear least-squares fit to the QCM data. **(B)** Contact angle measurements of a sessile water drop on LB films of DDA-capped gold nanoparticles plotted as a function of thickness (in terms of number of monolayers transferred) of the film. The solid line is to aid the eye and has no physical significance.

This is an interesting result of the investigation and may explain why stable monolayers of the gold nanoparticles at fairly high surface pressures could be obtained on the surface of water. The fairly high hydrophilicity could be due to interdigitated octadecanol molecules inferred from the π-A isotherm studies (Fig. 3.1). Such an interdigitation would result in a layer of polar OH groups surrounding the DDA hydrocarbon sheath and consequently, more hydrophilic monolayers. Given that the surface coverage of the gold nanoparticles per monolayer determined from QCM studies is 71%, and little of the underlying substrate would be "seen" by the sessile water drop in the contact angle measurements, the above seems the likely mechanism. This result, together with UV-vis spectroscopy results presented in Fig. 3.2A, clearly shows that multilayer LB films of the gold nanoparticles organized at the air–water interface may be grown uniformly in layer-by-layer fashion.
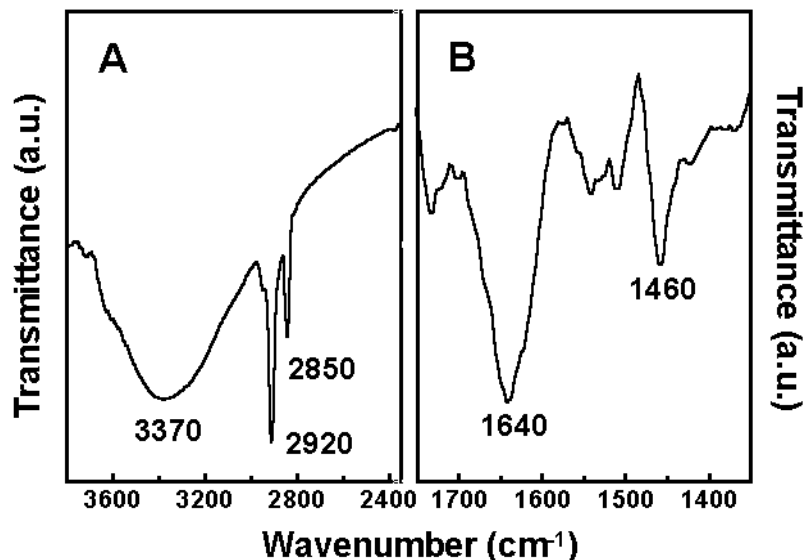
3.2-3d FTIR spectroscopic analysis

Figure 3.4 FTIR spectrum recorded from 20 ML thick LB film of DDA-capped gold
nanoparticles deposited on a Si (111) substrate in two different spectral
regions: **(A)** (3800-2400) cm^{-1} and **(B)** (1750-1350) cm^{-1}.

The FTIR spectrum of LB film (20 ML) of gold nanoparticles transferred to
hydrophobized Si (111) wafer was recorded and the spectrum obtained in the regions
(3800-2400) cm^{-1} and (1750-1350) cm^{-1} is plotted in Fig. 3.4A and B, respectively. The
methylene antisymmetric and symmetric vibration modes at 2920 cm^{-1} and 2850 cm^{-1},
respectively, are clearly seen in Fig. 3.4A and indicate that the hydrocarbon chains
capping the gold nanoparticles are closely packed without a significant density of defects
in the chains [35]. A broad peak observed at 3370 cm^{-1} is assigned to the N-H and O-H
stretch modes of vibration from the DDA molecules capping the surface of gold
nanoparticles and octadecanol molecules, respectively. In the lower spectral region (Fig.
3.4B), the feature at 1460 cm^{-1} arises due to methylene scissoring mode of vibration, the
splitting of which is a sensitive indicator of the crystalline packing of hydrocarbon chains
[36]. The fact that this feature is broad without noticeable splitting indicates that the
chains, though close packed are not in a crystalline environment. This is likely to be a
consequence of the surface of curvature of the gold nanoparticles. Another feature

observed at 1640 cm^{-1} is due to N-H bending vibration mode arising from the DDA molecules bound to the surface of gold nanoparticles.

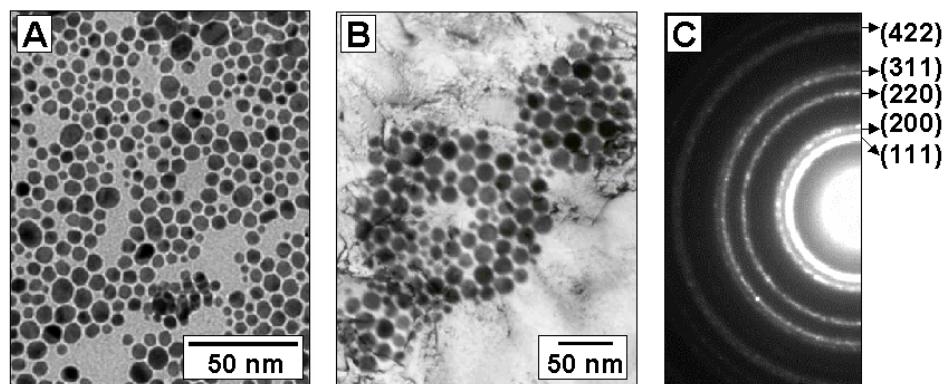### 3.2-3e *Transmission electron microscopy results*

Figure 3.5 **(A)** Representative TEM image recorded from the drop-coated film of DDA-capped gold nanoparticles deposited on TEM grid. **(B)** TEM image of one monolayer of DDA-capped gold nanoparticles transferred from air-water interface onto a carbon-coated TEM grid by vertical lifting. **(C)** Electron diffraction pattern obtained from the nanoparticles shown in image B.

Fig. 3.5A,B show representative TEM images of drop-coated film of DDA-capped gold nanoparticles from the as-prepared solution of nanoparticles and one monolayer of DDA-capped gold nanoparticles transferred by vertical deposition from the air–water interface on carbon coated TEM grids, respectively. Indexing of ring type diffraction pattern (Fig. 3.5C) obtained from the LB film of DDA-Au nanoparticles confirms the fcc lattice structure of gold nanoparticles matching with that of standard gold (JCPDF No. 040784). Drop-coated film of DDA-capped gold nanoparticles (Fig. 3.5A) shows spherical nanoparticles with average particle size distribution 5.8 ± 1.5 nm. The size of the spherical particles obtained in the film transferred by LB method ranges from 8 to 28 nm (Fig. 3.5B). Variation in size of gold nanoparticles in LB film in comparison with that in drop coated film may be possibly due to the sintering of gold nanoparticles on the surface of water. There are reports in the literature that monolayer-protected gold nanoparticles have a tendency to form large three-dimensional superstructures [37]. This occurs by a process termed digestive ripening, which involves refluxing of gold nanoparticles in the presence of an excess of capping ligand. This

process transforms polydisperse nanoparticles in solution into highly monodisperse ones, often by a method of ligand exchange [38a]. However, unlike the above-mentioned case, the present study deals with the organization of the nanoparticles at the air–water interface at room temperature with no additional ligands that could effect digestive ripening. Hence the possibility of digestive ripening as a mechanism for the formation of large domains was ruled out. Hutchison and co-workers have shown the formation of artificial templates obtained by friction transfer followed by a nanoreplication step on carbon substrate, which leads to the linear alignment of gold nanoparticles [38b]. This linear assembly of nanoparticles further results in the formation of nanowires due to sintering of nanoparticles on the substrate by heat treatment or exposure to electron beam bombardment [39]. It is possible that a similar mechanism of surface sintering of the gold nanoparticles is applicable in the present case, leading to the increase in the size of nanoparticles at the air–water interface.

It is clear from the above studies that the gold nanoparticles hydrophobized with DDA could be successfully organized on the surface of water to form Langmuir monolayer, which further can be deposited on the solid substrate in layer-by-layer fashion. However TEM analysis illustrates that the monolayer consists of many small domains of close packed assemblies of nanoparticles and does not show long range, 2D assembly of nanoparticles. In order to study the effect of hydrocarbon chain length of alkyl amine molecule on the organization of hydrophobized nanoparticles at air-water interface, similar experiments were performed with long chain alkyl amine (ODA)-capped hydrophobized gold nanoparticles.

3.2-4 Gold nanoparticles hydrophobized with ODA

3.2-4a *Surface pressure-Area (π-A) isotherm results*

Fig. 3.6 shows the π–A isotherm measurements of 1:1 (w/w) mixture of hydrophobized ODA-Au nanoparticles and octadecanol (ODO) in chloroform, spread on the surface of water. Area of trough was transformed into an effective area/cluster as mentioned previously in section 3.2-3a. Curves 1-3 indicate the isotherms recorded 15 min, 2 h and 12 h after spreading the monolayer. Though the take off area increases from

350 nm^2/cluster at time t = 15 min to 450 nm^2/cluster at time t = 12 h, there is no considerable change in isotherm curves as a function of time as it is observed in case of DDA-capped gold nanoparticles.
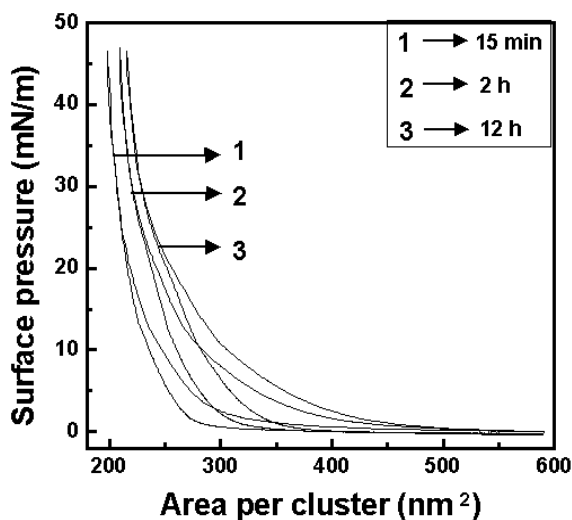

Figure 3.6 π–A isotherms recorded during one compression and expansion cycle of a 1:1 (w/w) mixture of ODA-Au nanoparticles and octadecanol as a function of time of spreading the monolayer on the surface of water.

This indicates that there is no reorganization of ODO molecules and gold nanoparticles on the surface of water as a function of time. Also unlike in the case of DDA-Au nanoparticles where the monolayer collapsed at very low surface pressure (20 mN/m) with average area/cluster of 350 nm^2 before collapse, the monolayer of ODA-capped gold nanoparticles was found to be stable up to surface pressure of 45 mN/m (Fig. 3.6) and the average area/cluster before collapse was found to be 250 nm^2. The area/cluster calculated theoretically, 72 nm^2 is much smaller than the closest packing area of 250 nm^2/cluster in fully compressed state (obtained from the π-A isotherm measurements, Fig. 3.6) due to electrostatic repulsive interactions between neighboring gold nanoparticles similar to that discussed in case of DDA-Au nanoparticles. π-A isotherm studies reveal that gold nanoparticles hydrophobized with ODA form more stable monolayer on the surface of water than those hydrophobized with DDA. From the π-A isotherm measurements (Fig. 3.6), a region of large incompressibility is seen to occur up to surface pressure of ca. 45 mN/m and, therefore, multilayer films of ODA-

capped gold nanoparticles of different thickness were transferred onto hydrophobized quartz substrates by the LB technique for optical absorption spectroscopy measurements.

3.2-4b *Transmission electron microscopy results*

TEM images recorded from one monolayer of ODA-Au nanoparticles deposited by vertical lifting from air-water interface on to copper grid show long range, ordered 2D assembly of nanoparticles (Fig. 3.7A & B, recorded at different magnifications) in comparison with the TEM image recorded from the drop coated film (Fig. 3.7C). It is also observed that the size of nanoparticles does not change after organizing them on the surface of water, as observed in case of DDA-capped gold nanoparticles. π-A isotherm and TEM results suggest that longer hydrocarbon chain length of a capping agent in case of alkyl amine capped gold nanoparticles helps to form stable monolayer resulting in long range, 2D assembly of nanoparticles when organized on the surface of water. Thus these results indicate that in case of DDA-capped gold nanoparticles, the major fraction of ODO molecules phase separate from the nanoparticles and thus lead to very small domains of nanoparticles.
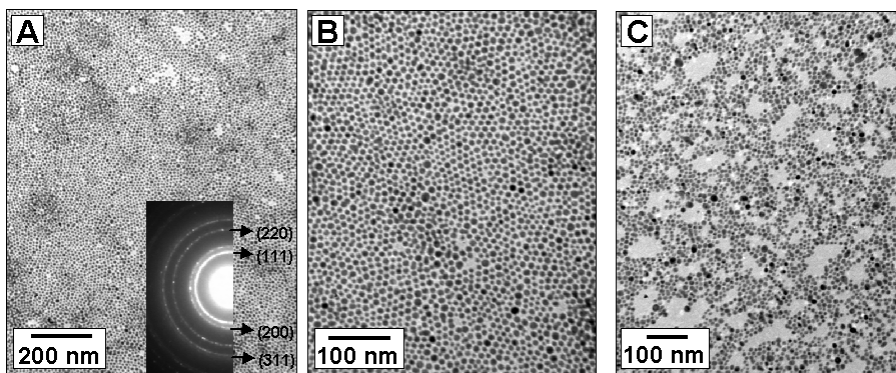

Figure 3.7 (A,B) Representative TEM images of one monolayer of ODA-capped gold nanoparticles transferred from air-water interface onto a carbon-coated TEM grid by vertical lifting. Inset of (A) shows the electron diffraction pattern obtained from nanoparticles shown in image A. **(C)** Representative TEM image recorded from the drop-coated film of ODA-capped gold nanoparticles.

While in case of ODA-capped gold nanoparticles they form mixed monolayer resulting in long-range assembly of nanoparticles. This may be an effect of better interdigitation of ODO molecules with ODA-capped gold nanoparticles than that with

DDA-capped gold nanoparticles probably due to the difference in the length of hydrocarbon chains.
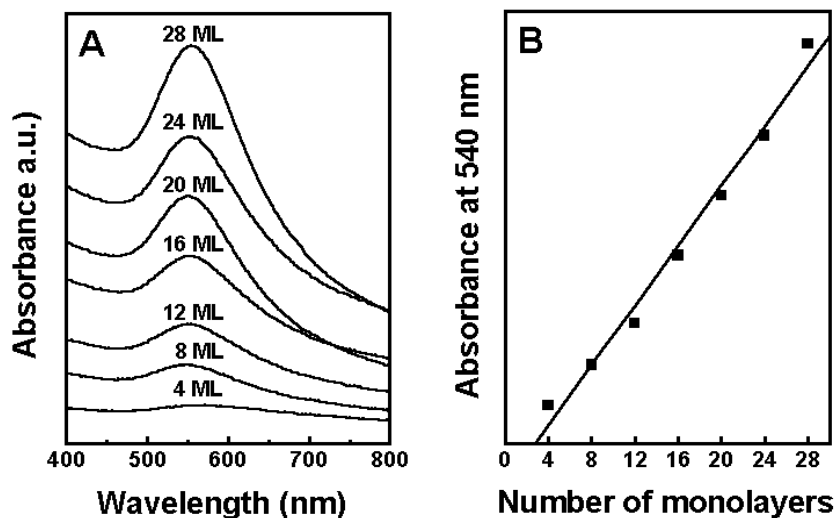
3.2-4c *UV-vis spectroscopic analysis*

Figure 3.8 **(A)** UV–vis spectra recorded from LB films of ODA-capped gold nanoparticles transferred onto quartz substrate at different thickness of the film. The number of monolayers of the gold nanoparticles in the LB films is indicated next to the respective curve. **(B)** A plot of intensity of the surface of plasmon resonance (at 540 nm) plotted as a function of number of monolayers of ODA-Au nanoparticles in LB films grown on quartz. The solid line is a nonlinear least-squares fit to the data.

UV-vis spectroscopy measurements made from the LB films of ODA-capped gold nanoparticles as a function of thickness are shown in Fig. 3.8A. The linear increase in the absorbance at 540 nm as a function of thickness of LB film (Fig. 3.8B) indicates the uniform layer-by-layer deposition of gold nanoparticles up to thickness of 28 ML. The red shift in surface plasmon resonance obtained as a consequence of interparticle plasmon coupling is less (540 nm) in comparison with that obtained in case of DDA-Au nanoparticles (578 nm). The difference in the shift of surface plasmon resonance can be attributed to the increase in the chain length of the capping molecule from C_{12} (in case of DDA-Au) to C_{18} (in case of ODA-Au nanoparticles), that leads to increase in interparticle separation and may result in weaker coupling between the particles. Besides, it is clear from TEM results that in case of DDA-Au nanoparticles (Fig. 3.5), there is increase in the

size of nanoparticles due to sintering after organizing them on the surface of water while no such change is observed in case of ODA-Au nanoparticles (Fig. 3.7).

Another striking difference revealed from TEM studies is that the assemblies of nanoparticles are much smaller in case of DDA-Au nanoparticles in comparison with the long-range assemblies obtained in case of ODA-Au nanoparticles. Thus the difference in particle size and extent of long-range assembly also could be the factors responsible for the change in shift of surface plasmon resonance obtained in case of LB films of DDA-Au and ODA-Au nanoparticles.

3.3 Assembly of hydrophobized silver nanoparticles at air-water interface

3.3-1 Synthesis of octadecylamine capped silver nanoparticles

Synthesis of silver nanoparticles by tyrosine reduction of silver ions under alkaline conditions was recently studied in our laboratory. 10 mL of 10^{-3} M aqueous silver sulfate solution was taken along with 10 mL of 10^{-3} M aqueous solution of tyrosine and the mixture was diluted to 100 mL with deionized water. To this, 1 mL of 0.1 M KOH was added, and the solution (pH 10) was allowed to boil until it turned yellow, indicating the formation of silver nanoparticles [39]. 50 mL of aqueous silver nanoparticle solution was taken, and its pH was adjusted to 5 using dilute hydrochloric acid (HCl) and was found to be stable. This solution was vigorously stirred with 50 mL of 5 x 10^{-4} M ODA in chloroform which results in phase transfer of silver nanoparticles from aqueous to chloroform phase. After phase transfer, aqueous phase became colorless and chloroform phase turned yellow (inset of Fig. 3.9A). The colorless aqueous phase was then discarded, and the process of phase transfer was continued with fresh tyrosine-reduced silver nanoparticle solution. About 1000 mL of tyrosine-reduced silver nanoparticle solution was transferred in this way. After completion of the phase transfer, the organic phase was separated from the aqueous phase, rotavapped, and washed with ethanol to remove excess uncoordinated ODA molecules. Removal of excess ODA was checked by monitoring the intensity of the signal at 3330 cm^{-1} in the FTIR spectrum of powder of ODA-capped silver (ODA-Ag) nanoparticles which arises due to N-H stretching and bending vibrations of free amine groups in ODA. Moderate washing of the

powder of ODA-Ag nanoparticles resulted in complete loss of the 3330 cm^{-1} band and indicated removal of uncoordinated ODA molecules (within detection limits of the FTIR instrument). The purified powder of ODA-Ag nanoparticles could be readily redispersed in different organic solvents such as chloroform, toluene, benzene and so forth. A known amount of powder form of purified ODA-Ag nanoparticles was redispersed in chloroform and used for further experiments.

3.3-2 Organization of silver nanoparticles at air-water interface and formation of LB films

Hydrophobized silver nanoparticles (ODA-Ag) were organized on the surface of water by spreading 110 μL (concentration 1mg/mL) solution of pure ODA-Ag nanoparticles in chloroform. π-A isotherm, UV-vis spectroscopy, FTIR spectroscopy, TEM, XPS and contact angle measurements were carried out according to the details discussed in chapter 2.

3.3-3 Silver nanoparticles hydrophobized with ODA

Silver nanoparticles synthesized by tyrosine reduction of silver sulphate solution at alkaline pH are stabilized by oxidized tyrosine molecules bound to the surface of nanoparticle through amine groups. The transfer of these nanoparticles to chloroform phase was achieved using ODA as a phase transfer molecule as described in the experimental section. It was observed that the phase transfer of the tyrosine-capped silver nanoparticles from aqueous phase to chloroform phase was strongly dependent on the pH of the aqueous solution of nanoparticles and that the phase transfer at pH 5 was most facile. This indicates that the transfer of nanoparticles is governed by the electrostatic interaction between ODA and nanoparticle surface bound tyrosine molecules as shown in Fig. 3.9B, step 1. The phase transfer of silver nanoparticles from aqueous to chloroform phase was monitored by UV-vis spectroscopy measurements. Curves 1 and 2 in Fig. 3.9A correspond to the spectra of the aqueous phase before and after phase transfer of silver nanoparticles while curves 3 and 4 are the spectra of the chloroform phase containing ODA before and after phase transfer, respectively. The sharp absorbance at 410 nm in the as-prepared solution of silver nanoparticles (curve 1) is due to the excitation of surface plasmons in the silver nanoparticles. The complete disappearance of this peak after

vigorous shaking with the chloroform solution of ODA (curve 2) indicates almost total phase transfer of the silver nanoparticles to the chloroform phase. This is also evident from the appearance of the sharp surface plasmon resonance at 417 nm observed in the spectrum of the chloroform phase after phase transfer (curve 4). The small damping and red shift of the surface plasmon band observed after the phase transfer (curve 4 in comparison with curve 1) can be attributed to the passivation of nanoparticles surface with ODA and to a change in the refractive index of the medium in which nanoparticles are suspended (refractive indices: chloroform: 1.446; water: 1.33) [40].
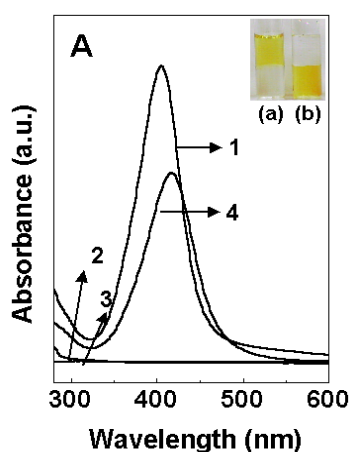

Figure 3.9 (A) UV-vis spectra of solution of silver nanoparticles before and after phase transfer. Curves 1 and 2: spectra of the aqueous phase containing tyrosine reduced silver nanoparticles before and after phase transfer respectively. Curves 3 and 4: chloroform phase containing 5×10^{-4} M ODA, before and after phase transfer of silver nanoparticles respectively. Inset of fig. shows the picture of tubes containing biphasic mixture, before (tube a) and after phase transfer (tube b).
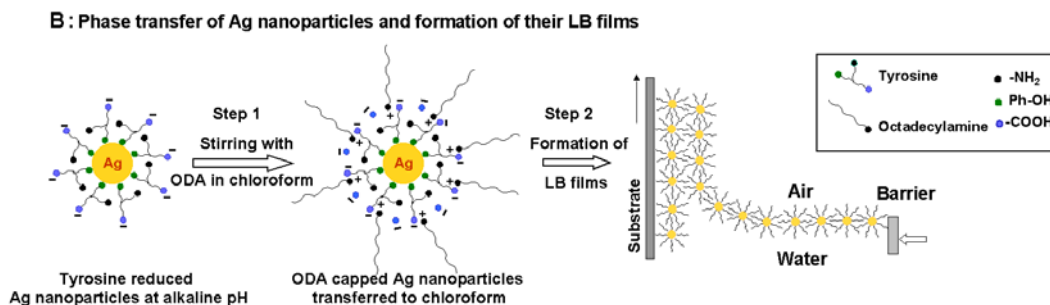

Figure 3.9 (B) Schematic showing the phase transfer of silver nanoparticles from aqueous phase to chloroform phase by electrostatic complexation between nanoparticles surface bound tyrosine from aqueous phase and ODA from chloroform phase and formation of their LB films

3.3-3a *Transmisson electron microscopy results*

Drop-coated film of silver nanoparticles transferred to chloroform phase using ODA molecules was prepared by solvent evaporation on carbon-coated copper grid and

analyzed by TEM. Representative transmission electron micrograph (Fig. 3.10A) shows the spherical nanoparticles of size 22 ± 3.6 nm which assemble into a close-packed structure, during evaporation of the solvent, chloroform.
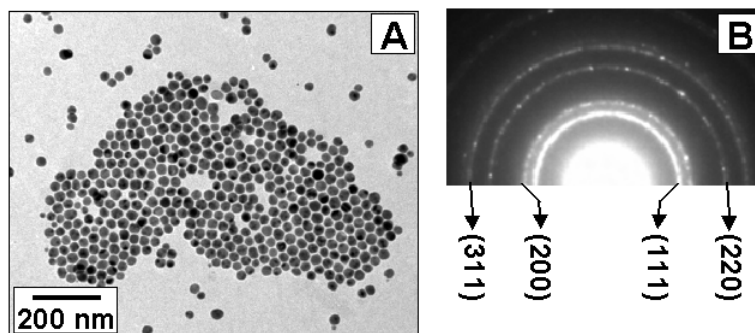

Figure 3.10 (A) TEM image of a drop-coated film of ODA-Ag nanoparticles deposited on a carbon-coated TEM grid. **(B)** Electron diffraction pattern recorded from the nanoparticles shown in image A.

Selected area electron diffraction pattern (Fig. 3.10B) recorded from the silver nanoparticles shown in Fig. 3.10A shows a number of diffuse rings, which could be indexed, based on the fcc structure of silver. It may be pointed out here that ODA capped silver nanoparticles are quite monodisperse if reduced with tyrosine (Fig. 3.10A) instead of the more common reducing agent, sodium borohydride. Hence unlike in case of gold nanoparticles, tyrosine was used as a reducing agent for the synthesis of silver nanoparticles in the present study.

3.3-3b *FTIR spectroscopic analysis*

FTIR and XPS measurements were carried out in order to understand the exact nature of interaction between ODA molecules and tyrosine-reduced silver nanoparticles. Fig. 3.11A,B show the FTIR spectra recorded from powders of pure ODA (curve 1) and ODA-Ag nanoparticles (curve 2) in different spectral windows, recorded with a KBr pellet. The peaks obtained at 3330 cm^{-1} (feature a) and 1565 cm^{-1} (feature b) in the case of pure ODA (curve 1) can be attributed to N-H stretching and bending vibrations, respectively. These features are completely broadened in the case of the ODA-Ag nanoparticles (curve 2). The appearance of a new peak at 1601 cm^{-1} (feature c) in curve 2

is due to the carbonyl stretching frequency from the carboxylate groups in the silver nanoparticles surface bound tyrosine molecules.
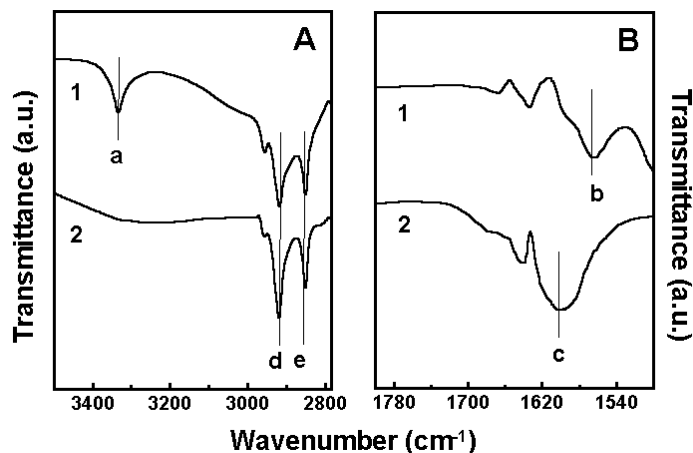

Figure 3.11 FTIR spectra of powders of pure ODA (curve 1) and ODA-Ag nanoparticles (curve 2) in the spectral windows **(A)** 3500-2800 cm^{-1} **(B)** 1800-1500 cm^{-1}.

The carbonyl stretch for carboxylic acids is known to occur at 1700 cm^{-1}[41]. The shift to lower wavenumbers clearly implies that the carboxylic acid group is ionized and that it is most likely complexed electrostatically with the protonated amine groups of ODA. Thus, the disappearance of N-H stretching and bending vibrations and the appearance of carboxylate stretching vibrations clearly indicates that the amine group of ODA interacts with the carboxylic acid group of tyrosine molecules bound to the surface of the silver nanoparticles (scheme 3.9B, step 1). This supports the experimental observation that facile phase transfer of the silver nanoparticles requires suitable adjustment of pH (pH 5) of the aqueous nanoparticle solution. The features d and e centered at 2920 and 2850 cm^{-1} are due to methylene antisymmetric and symmetric vibrations, respectively, which are common in both cases.

3.3-3c *X-ray photoelectron spectroscopic analysis*

The ODA-Ag nanoparticles in chloroform were drop coated in the form of a film onto a Si(111) substrate and analyzed by XPS. The general scan spectrum of the film showed the presence of strong C 1s, N 1s, and Ag 3d core levels with no evidence of impurities. The film was sufficiently thick, and therefore no signal was measured from

the substrate (Si 2p core level). The Ag 3d, C 1s, and N1s core levels recorded from the film are shown in Fig. 3.12A-C, respectively.
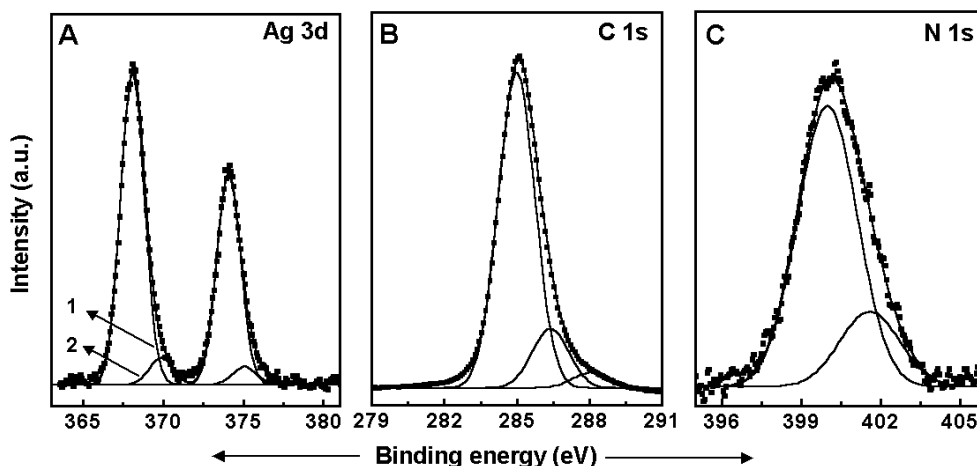

Figure 3.12 (A) Ag 3d, **(B)** C 1s, and **(C)** N 1s XPS core level spectra recorded from the LB film of ODA-Ag nanoparticles deposited on a Si(111) substrate by drop-coating. The solid lines are nonlinear least-squares fits to the data.

The spectra have been background corrected using the Shirley algorithm [42] prior to curve resolution, and the core levels were aligned with respect to the adventitious C1s BE of 285 eV. The Ag 3d core level spectrum (Fig. 3.12A) could be stripped into two chemically distinct spin-orbit pairs. The binding energies of two chemically distinct Ag 3d 5/2 components are observed at 368 and 370 eV. (labled 1 and 2 in Fig. 3.12A respectively). The low BE component is attributed to electron emission from the silver metal nanocore [43] while the high BE component arises from silver ions, indicating that a small fraction of unreduced Ag^+ ions remain bound to the surface of the nanoparticles. The C 1s core level spectrum recorded from the nanoparticle film could be stripped into three main chemically distinct components at 285, 286.4, and 288.1 eV (Fig. 3.12B). The high BE component observed at 288.1 eV can be assigned to the carboxylate carbon from the silver-bound tyrosine molecules. The 286.5 eV BE peak is attributed to the carbon adjacent to the carboxylic acid group in tyrosine as well as the carbon bound to the amine groups in ODA. Two chemically distinct components are observed at 400 and 401.5 eV in the case of the N1s core level spectrum (Fig. 3.12C). The presence of two N 1s signals

is indicative of protonated amine groups in ODA and surface-bound amine groups from tyrosine (scheme 3.9B).

3.3-3d *Surface pressure-Area (π-A) isotherm results*

The assembly of ODA-Ag nanoparticles into monolayers on the surface of water was followed by π-A isotherm measurements. Fig. 3.13 shows the π-A isotherms recorded as a function of time after spreading the solution of ODA-Ag nanoparticles on water subphase. Curve 1 is the isotherm recorded 15 min after spreading the monolayer, while curves 2-5 are the isotherms recorded 1, 2, 3, and 4 h after spreading the monolayer, respectively. The upward and downward directed arrows in the isotherms indicate the compression and expansion cycles of the monolayer respectively. The area of the trough was not transformed into an effective area/cluster since the theoretical prediction of mass of one hydrophobized colloidal silver nanoparticle is not as straight forward as in case of hydrophobized colloidal gold nanopartilcle. This is because unlike gold nanoparticles where the surface is hydrophobized with a monolayer of DDA/ODA, hydrophobized silver nanoparticles involve surface capping with tyrosine molecules, which are further complexed with ODA molecules. During compression, the surface pressure builds up, to reach a limiting value of ~ 40 mN/m (curve 1). However, it is observed that the monolayer expands gradually as a function of time, which is seen clearly by an increase in takeoff area from 300 cm^2 at time t = 15 min (curve 1) to 420 cm^2 at t = 3 h (curve 4). Minimal difference is seen in the isotherms recorded at time t = 3 h (curve 4) and t = 4 h (curve 5), which indicates that the monolayer of silver nanoparticles was stabilized 3 h after spreading the monolayer. From the π-A isotherm measurements (Fig. 3.13, curve 4), a region of reasonably large incompressibility is seen to occur up to a surface pressure of ca. 50 mN/m. Therefore multilayer films of ODA-capped Ag nanoparticles of different thickness were transferred onto different substrates at a surface pressure of 40 mN/m by the LB technique, 3 h after spreading the monolayer for further studies. During expansion of the monolayer, some hysteresis is observed, but this is not surprising given that the hydrophobic Ag nanoparticles cannot be considered to be truly amphiphilic.
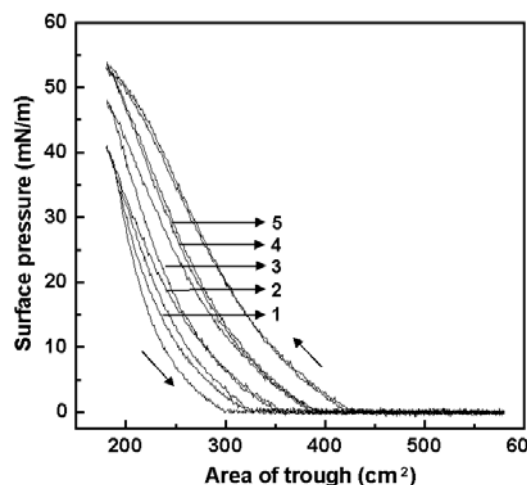
Figure 3.13 π-A isotherms during one compression and expansion cycle (indicated by arrows), recorded at different time intervals after spreading the ODA-Ag nanoparticle solution in chloroform on the surface of pure water. Curve 1, t =15 min; curve 2, t = 1 h; curve 3, t = 2 h; curve 4, t = 3 h; curve 5, t = 4 h.

The hysteresis observed may also arise due to rearrangement of the Ag nanoparticles within domains (and reorganization of the domains themselves) on release of surface pressure with a time scale larger than the experimentally controlled expansion rate of the monolayer.

3.3-3e *Transmission electron microscopy results*

Fig. 3.14(A-D) shows representative TEM images of one monolayer of ODA-Ag nanoparticles deposited vertically from the air-water interface onto a carbon-coated TEM grid, recorded at different magnifications. The low-magnification images (A,B) reveal that the silver nanoparticles assemble into linear, nanowire-like superstructures extending up to 3-4 μm in length. Each individual linear assembly is observed to consist of highly ordered domains of silver nanoparticles in a close-packed configuration (Fig. 3.14C). The hexagonally close-packed structure of the silver nanoparticles is clearly seen in the Fourier transform of the image shown in inset of Fig. 3.14C. The hexagonal arrangement of the spots in the Fourier transform attests to the existence of reasonably long-range ordering of the silver nanoparticles within the linear domains. From the periodicity of the spots in the Fourier transform, the average silver nanoparticle core-core separation was determined to be ca. 24 nm. We recollect that the average diameter of the silver particles

was determined to be 22 ± 3.6 nm. The center-center distance of 24 nm implies that the hydrophobic sheath surrounding the particles contributes 2 nm to the particle separations. Thus the bilayer thickness of the stabilizer on the surface of the silver nanoparticles is ca. 2 nm, which is less than twice the length of the stabilizer ODA calculated from the empirical formula of Bain *et al.*. (l = 0.25 nm + 0.127n nm, where n is the number of CH_2 groups, and 0.25 nm takes into account the amine and methyl terminal functional groups; l = 2.41 nm for ODA) [30].
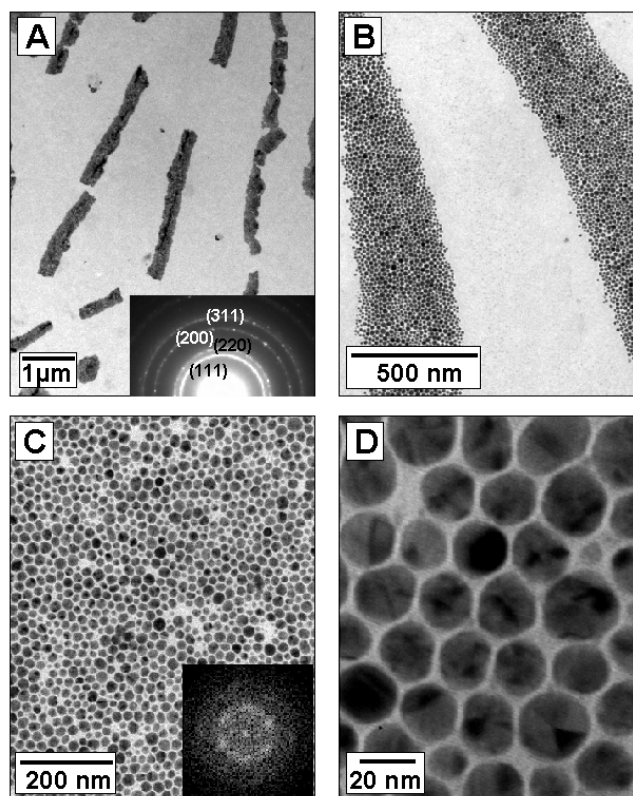
Figure 3.14 (A-D) Representative TEM images recorded at different magnifications from one monolayer of ODA-Ag nanoparticles transferred onto a carbon-coated TEM grid by the LB method. Inset of (A) shows the electron diffraction pattern obtained from nanoparticles shown in image A while inset of image (C) shows the Fourier transform recorded from image C.

Thus, there is considerable interdigitation of the hydrocarbon chains of ODA in the close-packed silver nanoparticle assemblies. The high magnification image of the silver nanoparticles in the linear superstructures shows that the particles are faceted with significant contrast within individual particles, indicating that they are multiply twinned

nanocrystals (Fig. 3.14D). The average particle diameter determined for the silver nanoparticles in the drop-coated film is ca. 22 nm (Fig. 3.10A), which is the same as the particle size of the nanoparticles in the LB film. The nanoparticles in the drop-coated film do not show any particular ordered packing or long range order suggesting that compression of the monolayer of silver nanoparticles on the surface of water and hydrophobic association of the interdigitating ODA chains are responsible for the ordered superstructures formed. At this stage, it is not clear why the particles assemble into linear superstructures and why so little of the totally available film area is covered with the particles. However, the rather small surface coverage obtained in the present case is consistent with previous reports for the two dimensional assembly of gold nanoparticles [44] and may be rationalized in terms of strong interparticle repulsive interactions which we believe will be operative in the phase-transferred silver nanoparticles. The charge on the surface of the nanoparticles could arise either from incomplete or over-charge-compensation of the negative charge by the ODA molecules (illustrated in scheme 3.9B for incomplete charge-compensation by ODA of the negatively charged oxidized product of tyrosine).

3.3-3f *UV-vis spectroscopic analysis*

LB films of the silver nanoparticles of different thickness were deposited on quartz substrates to study their optical properties (scheme 3.9B). Fig. 3.15A shows the UV-vis spectra of LB films of silver nanoparticles recorded as a function of number of monolayers. A broad absorption band centered at ca. 540 nm is observed in the LB films whose intensity increases with increasing number of monolayers in the LB film. The absorbance band at 540 nm is due to surface plasmon vibrations in silver nanoparticles in the film. Nano sized metal particles exhibit a unique surface plasmon absorption band, which is, superimposed onto the exponential-decay Mie scattering profiles [40]. Well-dispersed, spherical silver nanoparticles in solution in general show a sharp surface plasmon resonance in the range of 400-420 nm (Fig. 3.9A, curve 4). The surface plasmon band of the silver nanoparticles in the LB films is considerably red-shifted and broadened, indicating plasmon coupling because of close packed arrangement of

nanoparticles (Fig. 3.14C). A similar observation was made by Efrima's group in the case of LB films of oleic acid capped silver nanoparticles [18a].
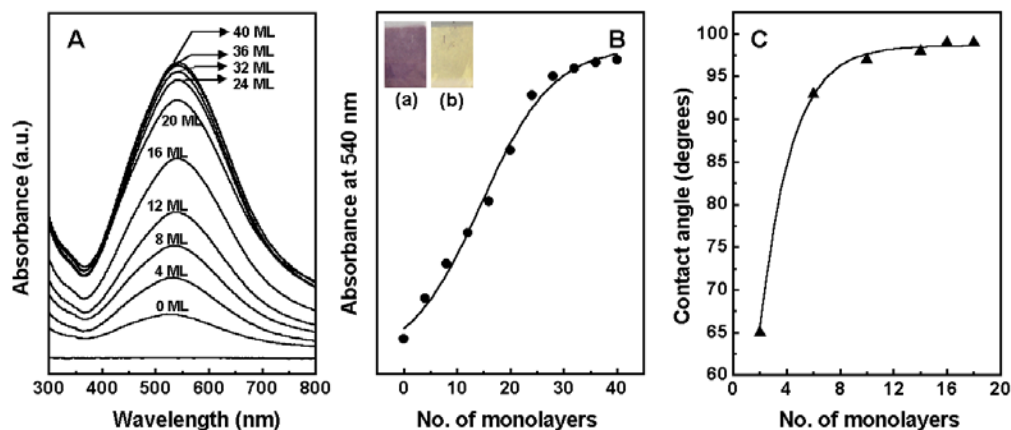

Figure 3.15 (A) UV–vis spectra recorded from LB films of ODA-Ag nanoparticles of different thickness transferred onto hydrophobized quartz substrate. The number of monolayers in the LB films is indicated next to the respective curves. **(B)** A plot of intensity of the surface plasmon resonance (absorbance at 540 nm) as a function of number of monolayers of ODA-Ag nanoparticles deposited on a quartz substrate. The inset shows photographs of a 40 ML LB film of the silver nanoparticles on a quartz substrate recorded normal to (a) and slightly off normal to the surface of the film (b). **(C)** Contact angle measurements of sessile water drop on LB films of ODA-Ag nanoparticles plotted as a function of thickness (in terms of number of monolayers transferred) of the film. The solid line is to aid the eye and has no physical significance.

The position of the absorption band in the UV-vis spectra of the silver nanoparticle LB films is very close to that normally observed for dispersed gold nanoparticles and indeed, direct viewing of the films showed that they possessed a purple color normally associated with gold nanoparticles (picture shown in the inset of Fig. 3.15B to the left). The LB films of the silver nanoparticles when viewed slightly off normal showed that they had a golden hue (inset of Fig. 3.15B, photo to the right). One of the problems associated with preparing thick LB films of pure, undiluted rigid cluster monolayers from the air-water interface is the poor monolayer transfer manifested by continuous breaking of the meniscus in both dipping directions (except for the first dipping cycle). However, in the present case, the absorption at 540 nm increases linearly with film thickness up to 24 monolayers (Fig. 3.15B), clearly indicates close to unity monolayer transfer ratios up to this thickness.

Fig. 3.15C shows the contact angle measurements of sessile water drop on LB films of the hydrophobized ODA-Ag nanoparticles of different thickness. The contact angle is 65° for LB film of 2 monolayers (ML), which increases to 93° for 6 ML film and reaches to a value of 99° for the 18 ML film. Hydrophilicity of the film at lower thickness is due to the incomplete coverage of the substrate with the monolayer. This is consistent with the TEM results, which show assemblies of nanoparticles leading to the formation of linear superstructures with lower surface coverage. However, once the surface of the substrate is fully covered, at a thickness of 6 ML, the film becomes hydrophobic (contact angle 93°). Unlike in case of DDA-capped gold nanoparticles where film is hydrophilic even at a thickness of 14 ML due to presence of ODO molecules, in the present case the film is highly hydrophobic due to hydrophobic nature of ODA-Ag of nanoparticles. This result, together with UV-vis spectroscopy results presented in Fig. 3.15A, clearly shows that multilayer LB films of the silver nanoparticles organized at the air–water interface may be grown uniformly in layer-by-layer fashion.

Thus, it has been demonstrated that the tyrosine reduced silver nanoparticles can be conveniently made hydrophobic and transferred to organic phase utilizing the electrostatic interaction between nanoparticle surface-bound tyrosine molecules and octadecylamine molecules present in the organic phase. The hydrophobized gold and silver nanoparticles give long range 2D ordered assembly when organized at the air-water interface. UV-visible spectroscopy, QCM and contact angle measurements of the multilayer films indicate that the film growth is lamellar. Further, different optical behaviour of LB films made from ordered assemblies of both gold and silver nanoparticles in comparison with respective dispersed spherical nanoparticles indicates the existence of interparticle surface plasmon coupling phenomenon between the particles in the arrays. Thus these monolayers could be good candidates for electron-transport measurements as a function of interparticle distance, parallel to the conventional systems comprising monolayer of short-chain thiol capped nanoparticles.

References

(1) (a) Ulman, A. "An Introduction to Ultrathin Organic Films: From Langmuir-Blodgett to Self-Assembly" Academic Press New York, **1991**. (b) Sastry, M. "Colloids and Colloid Assemblies: Synthesis, Modification, Organization and Utilization of Colloid Particles ed. F. Caruso, Wiley-VCH, Berlin Chapter 12, **2003**, 369-397. (c) Sastry, M. Handbook of Surfaces and Interfaces of Materials, Ed. H.S. Nalwa, Nanostructured Materials, Micelles and Colloids, Academic Press Volume 3, Chapter 2, **2001**, 87-119.

(2) (a) Ganguly, P.; Paranjape, D.V.; Sastry, M. *J. Am. Chem. Soc.* **1993**, *115*, 793. (b) Ganguly, P.; Paranjape, D.V.; Sastry, M. *Langmuir* **1993**, *9*, 577. (c) Ganguly, P.; Paranjape, D.V.; Patil, K.R.; Sastry, M.; Rondelez, F. *Langmuir* **1997**,*13*, 5440. (d) Clemente-Leon, M.; Mignotaud, C.; Agricole B.; Gomez-Garcia, C.J.; Coronado, E.; Delhaes, P. *Angew. Chem. Int. Ed. Ed. Engl.* **1997**, *36*, 1114. (e) Cuvillier, N.; Rondelez, F. *Thin Solid Films* **1998**, *19*, 327. (f) Chambers, C. R.; Atkinson, E. J. O.; McAdams, D.; Hayden, E. J.; Brown, D. J. A. *Chem. Comm.* **2003**, 2456.

(3) (a) Sastry, M.; Rao, M.; Ganesh, K.N. *Acc. Chem. Res.* **2002**, *35*, 847. (b) Sastry, M.; Ramakrishnan, V.; Pattarkine, M.; Gole, A.; Ganesh, K.N. *Langmuir* **2000**, *16*, 9142.(c) Ramakrishnan, V.; Manisha, M.; Ganesh, K.N.; Sastry, M. *Langmuir* **2002**, *18*, 6307. (d) Riccio, A.; Lanzi, M.; Antolini, F.; Nitti, C. de.; Tavani, C.; Nicolini, C. *Langmuir* **1996**, *12*, 1545. (e) Raedler, U.; Heinz, C.; Luigi, P.; Tampe, R. *Langmuir* **1998**, *14*, 6620. (f) Okahata, O.; Kobayashi, T.; Tanaka, K. *Langmuir* **1996**, *12*, 1326. (g) Shimomura, M.; Nakamura, F.; Ijiro, K.; Taketsuna, H.; Tanaka, M.; Nakamura, H.; Hasche, K. *J. Am. Chem. Soc.* **1997**, *119*, 2341. (h) Kago, K.; Matsuoka, H.; Yoshitome, R.; Yamaoka, H.; Ijiro, K.; Shimomura, M. *Langmuir* **1999**, *15*, 5193. (i) Ebara, Y.; Mizutani, K.; Okahata, Y. *Langmuir* **2000**, *16*, 2416. (j) Patino, J. M. R.; Fernandez, M. C. *Langmuir* **2004**, *20*, 4515. (k) Kent, M. S.; Yim, H.; Sasaki, D. Y.; Satija, S.;
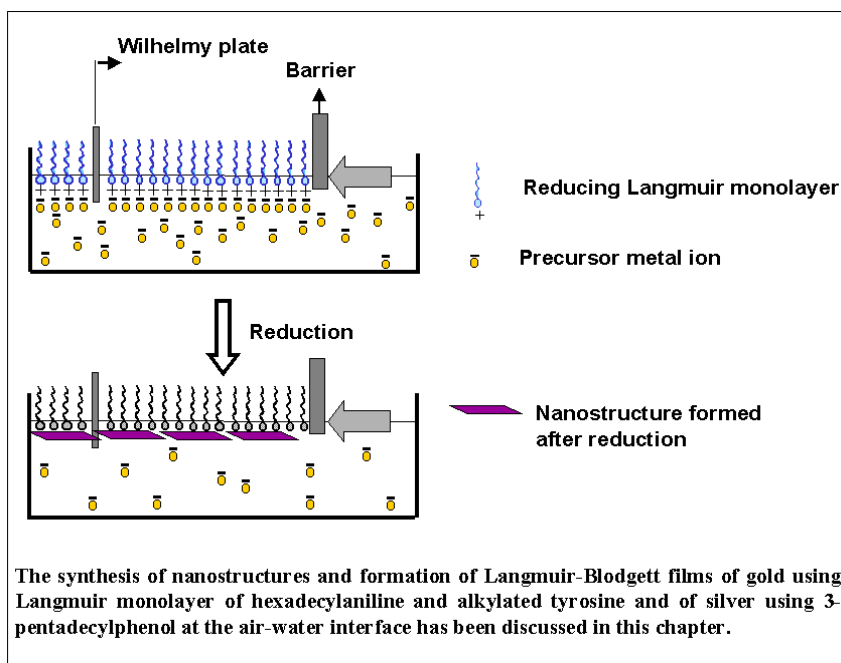
Majewski, J.; Gog, T. *Langmuir* **2004**, *20*, 2819. (l) Christian, S.; Marc, S.; Gerald, B.; Helmuth, M. *Macromolecules* **2004***,37*, 3865.

(4)　Kyunghee, C.Yi.; Fendler, J.H. *Langmuir* **1990**, *6*, 1519.

(5)　Yang, J.; Meldrum, F.C.; Fendler, J. H. *J. Phys. Chem.* **1995***, 99,* 5500.

(6)　Zhao, X.K.; McCormick, L.D.; Fendler, J. H. *Langmuir* **1991**, *7,* 1255.

(7)　Yang, J.; Fendler, J. H. *J. Phys. Chem.* **1995***, 99,* 5505.

(8)　Yi, K. C.; Horvolgyi, Z.; Fendler, J. H. *J. Phys. Chem*. **1994**, *98*, 3872.

(9)　Yi, K. C.; Mendieta, V. S.; Castaiiares, R.L.; Meldrum, F.C.; WU, C.; Fendler, J. H. *J. Phys. Chem.* **1995***, 99,* 9869.

(10)　Israelachvili, J. N. *Intermolecular and surface forces* Academic Press, San Diego, **1996**.

(11)　Meldrum, F. C.; Kotov, N. A.; Fendler, J. H. *Langmuir* **1994***, 10,* 2035.

(12)　Meldrum, F. C.; Kotov, N. A.; Fendler, J. H. *J. Phys. Chem.* **1994***, 98,* 4506.

(13)　Kotov, N. A.; Meldrum, F.C.; Fendler, J.H. *J. Phys. Chem.* **1994***, 98,* 8827.

(14)　Kotov, N. A.; Zavala, G.; Fendler, J. H. *J. Phys. Chem.* **1995***, 99,* 12375.

(15)　Meldrum, F.C.; Kotov, N. A.; Fendler, J. H. *Chem. Mater.* **1995**, *7,* 1112.

(16)　(a) Kotov, N. A.; Meldrum, F. C.; Wu, C.; Fendler, J. H. *J. Phys. Chem.* **1994***, 98,* 2735. (b) Tian, Y.; Fendler, J.H. *Chem. Mater.* **1996**, *8,* 969.

(17)　Ganguly, P.; Paranjape, D.V.; Patil, K.R.; Chaudhari, S. K.; Kshirsagar, S.T. *Indian J. Chem. A* **1992**, *31*, F42.

(18)　(a) Wang, W.; Chen, X.; Efrima, S. *J. Phys. Chem. B* **1999**, *103,* 7238. (b) Heath, J. R.; Knobler, C. M.; Leff, D. V. *J. Phys. Chem. B* **1997**,*101*, 189.

(19)　(a) Burghard, M.; Philipp, G.; Roth, S.; von Klitzing, K.; Pugin, R.; Schmid, G. *Adv. Mater.* **1998**, *10*, 842. (b) Bourgoin, J. F.; Kergueris, C.; Lefevre, E.; Palacin, S. *Thin Solid Films* **1998**, *327-329*, 515. (c) Chen, X. Y.; Li, J. R.; Jiang, L. *Nanotech.* **2000**, *11*, 108. (d) Kim, B.; Tripp, S. L.; Wei, A. *J. Am. Chem. Soc.* **2001**, *123,* 7955. (e) Brust, M.; Stuhr-Hansen, N.; Nørgaard, K.; Christensen, J. B.; Nielsen, L. K.; Bjørnholm, T. *Nano Lett.* **2001**, *1*, 189. (f) Brown, J. J.; Porter, J. A.; Daghlian, C. P.; Gibson, U. J. *Langmuir* **2001**, (g)

Huang, S.; Minami, K.; Sakaue, H.; Shingubara, S.; Takahagi, T. *Langmuir* **2004**, *20*, 2274. (h) Santhanam, V.; Andres, R. P. *Nano Lett.* **2004**, *4*, 41.

(20)   (a) Sastry, M.; Patil, V.; Mayya, K.S.; Paranjape, D.V.; Singh, P.; Sainkar, S.R. *Thin Solid Films* **1998**,   324, 239. (b) Perez, H.; de Sousa, R.M. Lisboa; Pradeau, J.P.; Albouy, P.A. *Chem. Mater.* **2001**, *13*, 1512.

(21)   Damle, C.; Gole, A.; Sastry, M. *J.Mater.Chem.* **2000**, *10*, 1389.

(22)   (a) Chen, S. *Adv. Mater.* **2000**,*12*, 186. (b) Chen, S. *Langmuir* **2001**, *17*, 2878.

(23)   Hassenkam, T.; Nørgaard, K.; Iversen, L.; Christopher, J. K.; Brust, M.; Bjørnholm T. *Adv. Mater.* **2002**, *14*, 1126.

(24)   Tao, A.; Kim, F.; Hess, C.; Goldberger, J.; He, R.; Sun, Y.; Xia, Y.; Yang P. *Nano Lett.* **2003**, *3*, 1229.

(25)   Kim, F.; Kwan, S.; Akana, J.; Yang, P. *J. Am. Chem. Soc.* **2001**, *123,* 4360.

(26)   Mayya, K. S.; Patil, V.; Sastry, M. *Langmuir* **1997**, *13,* 2575.

(27)   (a) Sastry, M.; Mayya, K. S.; Patil, V.; Paranjape, D. V.; Hegde, S. G. *J. Phys. Chem. B* **1997**, *101,* 4954. (b) Mayya, K. S.; Sastry, M. *Langmuir* **1998**, *14,* 74.

(28)   Sastry, M.; Patil, V.; Mayya, K.S. *Langmuir* **1997**, *13*,4490.

(29)   Sastry, M.; Kumar, A.; Mukherjee, P. *Colloids Surf. A* **2001**, *181*, 255.

(30)   Bain, C. D.; Evall, J.; Whitesides, G. M. *J. Am. Chem. Soc.* **1989**, *111*, 7155.

(31)   Patil, V.; Malvankar, R.B.; Sastry, M.; *Langmuir* **1999**, *15*, 8197 and references therein.

(32)   Quinten, M.; Kreibig, U. *Surf. Sci.* **1986**, *172*, 557.

(33)   Collier, C. P.; Saykally, R. J.; Shiang, J. J.; Henrichs, S. E.; Heath, J. R. *Science* **1997**, *277*, 1978.

(34)   Sastry, M.; Patil, V.; Mayya, K.S. *J. Phys. Chem. B* **1997**, *101*, 1167.

(35)   Hostetler, M.J.; Stokes, J.J.; Murray, R.W. *Langmuir* **1996**,*12*,3604.

(36)   Sydow, R.G. von *J. Mol. Spectrosc.* **1961**, *7*,116.

(37)   Prasad, B.L.V.; Stoeva, S.I.; Sorensen, C.M.; Klabunde, K.J. *Langmuir* **2002**, *18*, 7515.

(38) (a) Brown, L.O.; Hutchison, J.E. *J. Phys. Chem. B* **2001**, *105*, 8911. (b) Brown,L.O.; Hutchison, J.E. *J. Am. Chem. Soc*. **1999**, *121*,882. (c) Hutchinson, T.O.; Liu, Y.-P.; Kiely, C.; Kiely, C.J.; Brust, M. *Adv. Mater*. **2001**, *13*, 1800.

(39) Selvakannan, PR.; Swami, A.; Srisathiyanarayanan, D.; Shirude, P. S.; Pasricha, R.; Mandale, A.B.; Sastry, M. *Langmuir* **2004**, *20*, 7829.

(40) (a) Underwood, S.; Mulvaney, P. *Langmuir* **1994**, *10*, 3427. (b) Kelly, K. L.; Coronado, E.; Zhao, L. L.; Schatz, G. C. *J. Phys. Chem. B* **2003**, *107*, 668.

(41) Silverstein, R. B.; Bassler, G. C. *Spectrometric Identification of Organic Compounds*, 2nd ed.; John Wiley & Sons: New York, **1967**, Chapter 3, p 88.

(42) Shirley, D. A. *Phys. Rev. B* **1972**, *5*, 4709.

(43) Fadley, C. S.; Shirley, D. A. *J. Res. Nat. Bur. Stand*. **1970**, *74A*, 543.

(44) (a) Grabar, K. C.; Allison, K. J.; Baker, B. E.; Bright, R. M.; Brown, K. R.; Freeman, R. G.; Fox, A. P.; Keating, C. D.; Musick, M. D.; Natan, M. J. *Langmuir* **1996**, *12*, 2353. (b) Mayya, K. S.; Patil, V.; Sastry, M. *Langmuir* **1997**, *13*, 2575.

C H A P T E R IV

Synthesis of nanostructures at the air-water interface by the spontaneous reduction of precursor metal ions in the subphase using Langmuir monolayers as reducing agents

The synthesis of nanostructures and formation of Langmuir-Blodgett films of gold using Langmuir monolayer of hexadecylaniline and alkylated tyrosine and of silver using 3-pentadecylphenol at the air-water interface has been discussed in this chapter.

4.1 Introduction

It is now well recognized that in addition to nanoparticle size and composition, the shape of the nanoparticles plays an important role in modulating their electronic, optical [1] and catalytic properties [2]. As a consequence, there is considerable current interest in developing synthesis methods to control the shape of nanoparticles. In so far as noble metal nanoparticles such as gold, silver and semiconductor nanoparticles are concerned, plethora of solution based experimental procedures have been developed for shape modulation [1a, 3]. Most of the protocols result predominantly in rod-like nanoparticles of silver [4], gold [3b,5], cadmium selenide [6], tungsten sulfide [7] with a tunable aspect ratio and nanoprisms of silver [3a]/gold [3h, 8] and cadmium sulphide [9]. In addition, Xia and co-workers have developed methods for the synthesis of silver nanowires [10a,b], nanocubes [10c], and triangular nanoplates [10d] through a soft, self-seeding, polyol process. Further to this they have also established a one-step approach to the large scale synthesis of gold, platinum and palladium nanostructures with hollow interiors by the transmetallation reaction between silver nanostructures and an aqueous precursor metal ion solution [10e-g]. A similar strategy has been used for the synthesis of nanoframes of gold [11]. Structures such as gold nanoshells [12] have also been reported recently using silica spheres as templates for its formation.

From the above reports it can be noted that usually shape anisotropy is introduced in nanoparticles by synthesizing them in the presence of templates such as porous alumina [13,14], polycarbonate membranes [15], carbon nanotubes [16,17], aqueous surfactant media [3b,18], and a seed mediated growth process [3g]. Apart from this, it has been shown that exposing the metal ions entrapped in thin LB films of suitable amphiphilic molecule to reducing atmosphere leads to confined growth of nanostructures and thus results in anisotropy in their shape [19]. Langmuir monolayers of suitable amphiphilic molecules acting as a template have also been used for the synthesis of anisotropic nanostructures [20]. Owing to the fact that air-water interface has intrinsic anisotropy, it could be a model system for the generation of anisotropic nanostructures.

Surprisingly, the use of air-water interface for achieving nanoparticle shape control remains largely unexplored and under exploited.

In this laboratory the multifunctional capability of the molecule 4-hexadecylaniline (4-HDA) has been demonstrated in the one-step synthesis of gold nanoparticles in organic media [21]. This molecule plays the role of a phase transfer agent (enabling transfer of $AuCl_4^-$ ions from aqueous to organic phase), reducing agent and capping agent for the gold nanoparticles that are predominantly spherical in shape. Making use of the built-in anisotropy of the air–water interface, we here show that Langmuir monolayer of 4-HDA on an aqueous subphase of chloroauric acid results in the formation of nano-sheets/-ribbons of gold at the air–water interface. The use of a two dimensional reducing interface constrains growth of the gold nanocrystals within the plane of the Langmuir monolayer and sets it apart from existing air-water interface wet-chemistry methods [20] where the role of the Langmuir monolayer is passive and the growth zone is much more delocalized. The amphiphilic molecule bearing head group acting as a reducing agent can be used for the synthesis of nanoparticles at both liquid-liquid and air-water interfaces. Hence the above synthesis strategy can be generalized for the synthesis of other metal nanoparticles using appropriate Langmuir monolayer. Stepping ahead in this direction, we have synthesized C_{18} -alkylated tyrosine molecule (reduction of gold ions with tyrosine is reported in the literature [22]) and have shown that it behaves similar to 4-HDA molecules at both liquid-liquid (forming spherical nanoparticles) and air-water interfaces (forming anisotropic, flat nanosheets). In a sense, it has been shown that shape variation in the nanoparticles can be achieved by carrying out reduction with same reducing agent at two different interfaces. Further, we have established this approach for the synthesis of silver nanoparticles by reduction of silver ions in the subphase, under alkaline conditions using 3-pentadecylphenol (3-PDP) Langmuir monolayer. In a previous study we have shown that aqueous silver nanoparticles can be synthesized using the amino acid tyrosine at alkaline pH (discussed in chapter 3). Under the alkaline conditions, the phenolic group in tyrosine forms phenolate anion that is capable of reducing silver ions. Surface capping of the silver

nanoparticles by the oxidized tyrosine molecules renders them highly stable. Inspired by these results, we investigate here the possibility of using Langmuir monolayers of 3-pentadecylphenol (PDP) as two-dimensional reducing agent in the formation of silver nanoparticles. We observe that reduction of silver ions present in the subphase under alkaline conditions by 3-PDP Langmuir monolayers leads to the spontaneous formation of highly ordered, large domains of spherical silver nanoparticles at the air-water interface in one step. In the following sections, we have discussed in detail the synthesis of gold nanostructures using 4-HDA and C_{18}-alkylated tyrosine Langmuir monolayer and silver nanostructures using 3-PDP Langmuir monolayer.

4.2 Synthesis of gold nanostructures at air-water interface using hexadecylaniline (4-HDA) Langmuir monolayer

100 μL of 4-HDA in chloroform (conc. 1 mg/mL) was spread on the surface of 10^{-4} M aqueous chloroauric acid (HAuCl$_4$) solution in a Langmuir trough. After measurement of π–A isotherms, the 4-HDA monolayer was compressed to a surface pressure of 20 mN/m and maintained at this pressure for 36 h in the dark. Pressure-Area (π–A) isotherm measurements and the transfer of gold nanoribbon-HDA complex monolayer formed at the air-water interface were carried out according to the details mentioned in chapter 2. The control experiment was almost identical to that presented above with the only difference being that after quick compression of the monolayer to surface pressure of 20 mN/m, the monolayer was exposed to vapors of hydrazine for 30 min in a chamber enclosing the trough.

4.2-1 *Surface pressure-Area (π-A) isotherm results*

In Fig. 4.1A curves 1 and 2 correspond to the isotherms of 4-HDA monolayer measured after spreading on the surface of deionized water and aqueous HAuCl$_4$ solution respectively. It is observed that in case of deionized water, the 4-HDA monolayer is stable upto surface pressure of 45 mN/m while it collapses slowly at comparatively low surface pressure (above 20 mN/m) when spread on the surface of HAuCl$_4$ subphase. The amine groups of 4-HDA spread on the aqueous HAuCl$_4$ solution (pH 3.7) are protonated and thus electrostatically complex with chloroaurate anions (AuCl$_4^-$) present in the

subphase. The complexation of $AuCl_4^-$ ions with 4-HDA monolayer leads to alteration in the organization of the monolayer at the air-water interface and thus leads to a low collapse pressure. Further, formation of the 4-HDA monolayer on the surface of aqueous $HAuCl_4$ solution was followed by π-A isotherm measurements as a function of time after spreading the 4-HDA monolayer.
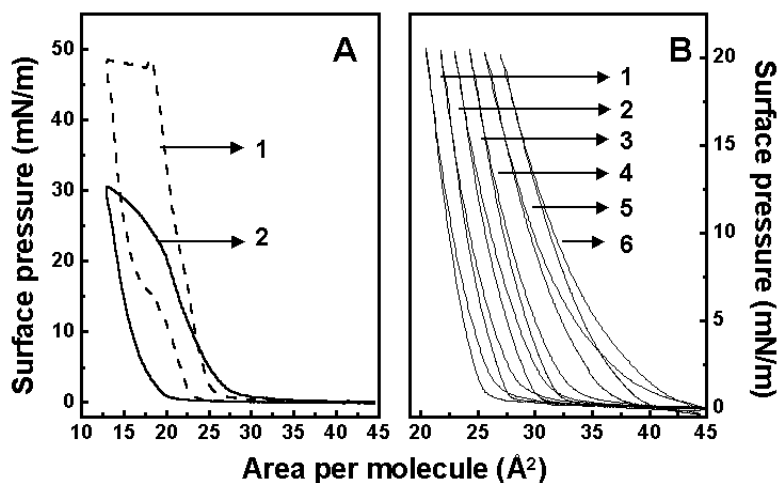

Figure 4.1 **(A)** π–A isotherms (showing collapse pressures) recorded during one compression and expansion cycle of HDA Langmuir monolayer on surface of pure water (curve 1); and aqueous 10^{-4} M chloroauric acid solution (curve 2). **(B)** π–A isotherms of HDA Langmuir monolayer on surface of aqueous 10^{-4} M chloroauric acid solution recorded as a function of time of spreading the monolayer (curves 1-6 correspond to the isotherms recorded at time, t = 15 min, 6 h, 12 h, 18 h, 24 h and 36 h respectively after spreading the monolayer).

In Fig. 4.1B, curves 1-6 show the isotherms recorded at time, t = 15 min, 6 h, 12 h, 18 h, 24 h and 36 h after spreading 4-HDA on aqueous $HAuCl_4$ subphase. The large expansion of the 4-HDA monolayer was observed from 30 Å^2/molecule at time t = 15 min to 45 Å^2/molecule at t = 36 h (Fig. 4.1B, curves 1 and 6 respectively) as the $AuCl_4^-$ ions get reduced and evolve completely into gold nanostructures as discussed in the next section.

4.2-2 *Transmission electron microscopy results*

TEM images recorded from a two-monolayer (2 ML) LB film of gold-HDA complex formed by exposing $AuCl_4^-$ ions in the subphase to the 4-HDA Langmuir monolayer for 36 h revealed the presence of a very large concentration of flat gold

nanosheets/ribbons and, occasionally, triangular gold nanoparticles (Fig. 4.2A,B). A higher magnification image of two gold nanoribbons crossing one another is shown in Fig. 4.2C. While an estimate of the thickness of the ribbons and sheets in this study could not be made, from TEM analysis the contrast in the region of overlap clearly shows that the gold nanostructures are extremely thin. The dark bands observed in the structures are probably due to strains in the ribbons from buckling during growth or deposition of the LB film.
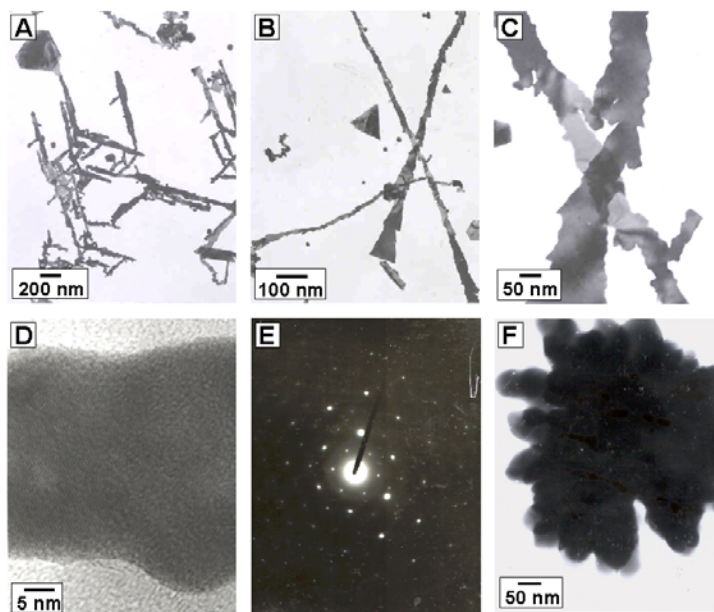

Figure 4.2 (A-D) Representative TEM images at different magnifications of the LB film of gold nanosheets/ribbons formed by the reduction of chloroaurate ions in the subphase by the HDA Langmuir monolayer. **(E)** Electron diffraction pattern obtained from the nanostructures shown in image D. **(F)** TEM image of a nanogold aggregate formed by hydrazine reduction of $AuCl_4^-$ ions complexed with HDA monolayer.

Fig. 4.2D is a high-resolution TEM image of an individual gold nanoribbon that shows the lattice planes corresponding to fcc gold in this nanoribbon. The selected-area electron diffraction (SAED) pattern (Fig. 4.2E) from one of the gold nanoribbon clearly shows that it is single crystalline. The hexagonal nature of the diffraction spots is a clear indication that the gold nanoribbons are highly (111) oriented with this plane normal to the electron beam. The spots could be indexed based on the face-centred-cubic (f.c.c.) structure of gold. Formation of gold nanoribbons at the air-water interface using 4-HDA

Langmuir monolayer involves oxidation of 4-HDA molecules leading to reduction of $AuCl_4^-$, this possibly prevents further complexation/reduction of $AuCl_4^-$ ions at the air-water interface. The reduction of gold ions feeding nanoribbon formation is thus limited to only a monolayer of gold ions originally bound to the 4-HDA monolayer. Indirectly, this supports the TEM evidence that the gold nanoribbons are extremely thin. That the ribbonlike gold nanoparticles morphology is indeed due to spontaneous reduction of $AuCl_4^-$ ions by the 4-HDA Langmuir monolayer was conclusively shown by a simple control experiment. Fig. 4.2F shows a TEM image recorded from a 2 ML LB film grown from gold particles complexed with 4-HDA Langmuir monolayer, however the reduction of the gold ions in this case was accomplished by hydrazine reduction of the metal ions immediately after spreading of the Langmuir monolayer. The gold nanoaggregate is extremely thick and of a dendritic morphology (Fig. 4.2F). Hydrazine is a strong reducing agent that competes with the 4-HDA molecules and leads to complete reduction of the $AuCl_4^-$ ions within 30 min. It may be noted that in case of hydrazine, reduction occurs in the entire subphase while the reduction is confined only to the interfacial region in case of 4-HDA monolayer.

It is observed that the boundary of the nanoribbons is highly serrated (Fig. 4.2C), which suggested the possibility of formation of nanoribbons by self-assembly of smaller triangular units. In order to confirm this, kinetics of growth of nanoribbons was followed by recording TEM images as a function of time of reaction of $AuCl_4^-$ ions with the 4-HDA Langmuir monolayer (Fig. 4.3A-D). Finely dispersed gold nanoparticles were observed after 2 h of reaction (Fig. 4.3A) that expanded with time by the growth of secondary gold nuclei at the periphery of existing gold nanostructures (Fig. 4.3B, 6 h) and eventually, elongated gold nanoribbons were formed at larger reaction times (Fig. 4.3C,D 20 h and 36 h respectively) by a random nucleation and growth process. Thus, the TEM kinetics study reveals that serrated edges of the gold nanoribbons appear due to a templated growth process rather than assembly of smaller triangular subunits. Growth of gold nanostructures as a function of time also supports the expansion of 4-HDA

monolayer while the reaction proceeds as observed via increase in pressure take-off area during π-A isotherm measurements (Fig. 4.1B).
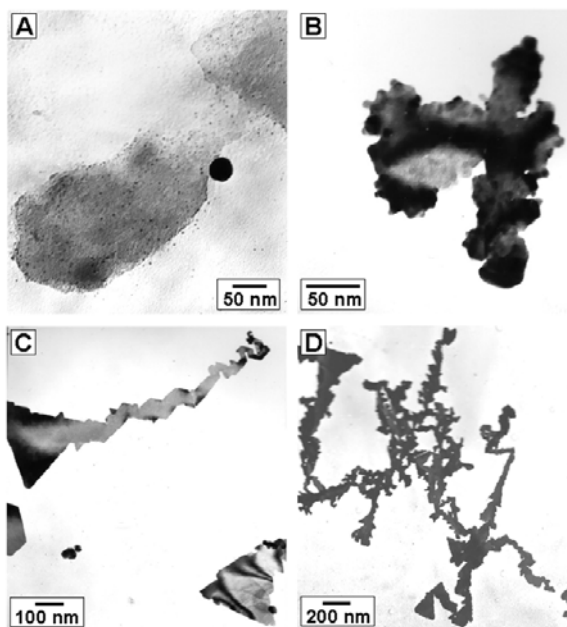

Figure 4.3 (A-D) Representative TEM images recorded at time, t = 2 h, 6 h, 20 h and 36 h respectively of formation gold nanosheets/ribbons by the reduction of chloroaurate ions in the subphase by the HDA Langmuir monolayer.

4.2-3 X-ray diffraction analysis

Formation of gold nanosheets/ribbons at the air-water interface indicates that growth of the nanocrystalline material is highly localized due to confinement of reducing agent (4-HDA) to the two dimensional interface. XRD pattern recorded from a 20 ML LB film of the gold nano-HDA complex deposited on glass shows that the gold nanocrystal growth is also highly face-selective as shown in the Fig. 4.4A. The XRD pattern shows very intense (111) Bragg reflection of fcc gold [23] indicating highly oriented growth of the nanocrystals at the air-water interface. The inset shows the XRD pattern on an expanded scale showing that the (200) and (220) Bragg reflections are extremely weak and considerably broadened relative to the (111) reflection. This interesting feature indicates that gold nanocrystals are highly anisotropic in shape in agreement with TEM results.
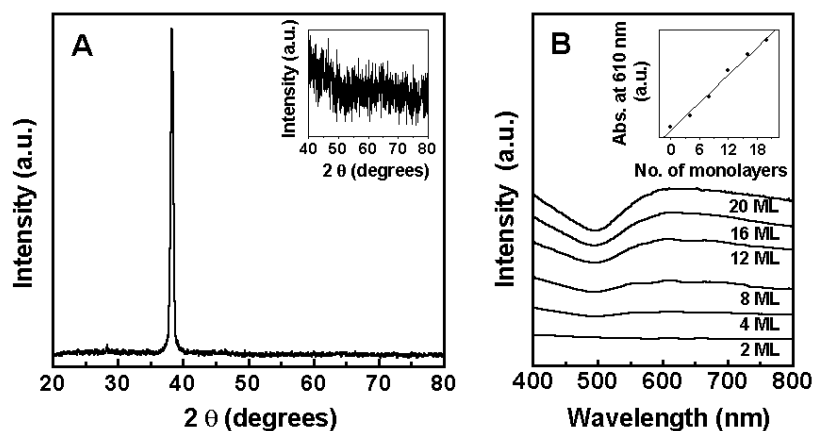
Figure 4.4 (A) XRD pattern recorded from LB film of 20 ML thick gold nanosheets/ribbons deposited on glass. The inset shows an expanded region of the XRD pattern highlighting the less intense Bragg reflections. **(B)** UV-vis spectra recorded from LB films of the gold nanosheets/ribbons of different thickness (thickness in terms of number of monolayers indicated next to the respective spectrum) deposited on quartz. Inset shows the absorbance of gold nanoribbons at 610 nm plotted as a function of number of monolayers.

Attempts were made to estimate the thickness of the gold nanoribbons by monitoring the (00*l*) Bragg reflections in the low 2θ region of the XRD pattern but good signal to-noise ratio could not be obtained. We would like to point out here that 4-HDA-reduced spherical gold nanoparticles obtained in solution (reduction at liquid-liquid interface) [21] and also the gold nanoaggregates formed in case of the control experiment where $AuCl_4^-$ ions covered with 4-HDA monolayer were reduced by exposure to hydrazine vapors did not show any preferred orientation. In order to check whether formation of highly (111)-oriented, flat gold nanosheets/nanoribbons at the air–water interface is due to epitaxy between the 4-HDA Langmuir monolayer and the nucleating gold nanocrystals, efforts were made to break the periodicity of the 4-HDA Langmuir monolayer by mixing it with the surfactant, octadecylamine (ODA) in different ratios. π–A isotherm measurements of mixtures of 4-HDA and ODA in the molar ratios 1:1 and 1:3 on an aqueous HAuCl₄ subphase did not show any evidence of phase separation and confirms the breakage in periodicity of the 4-HDA Langmuir monolayer. The nanogold films formed using these mixed monolayers were transferred onto glass and analyzed by x-ray diffraction. The XRD patterns of these LB films (formed from 4-HDA:ODA mixed

Langmuir monolayers) also showed very strong (111) Bragg peaks indicating similar face-selective growth in the (111) direction. Thus, this control experiment suggests that the formation of highly anisotropic, (111)-oriented flat nanostructures at the air–water interface is not a consequence of epitaxy but most probably due to surface energy considerations [the (111) crystallographic face is the most energetically favorable crystal face] and stabilization of the nanosheets/nanoribbons by the oxidized product of 4-HDA.

4.2-4 *UV-vis spectroscopic analysis*

A major advantage of organization of nanoparticles at the air-water interface is that multilayer superlattice films of close-packed nanoparticle assemblies may be deposited by the LB method as illustrated in chapter 3. Fig. 4.4B shows the UV-vis spectra recorded from LB films of the gold nanoribbon-HDA complexes of different thickness deposited on quartz substrates. A broad absorption band centered at ca. 610 nm is observed in the films. This absorption band arising due to excitation of surface plasmons in spherical gold nanoparticles has comparatively small band width and occurs in the range 510-530 nm in solution [1a]. The shift and broadening of the resonance in the LB films indicates considerable aggregation of the particles and/or a high degree of anisotropy in the particle shape, both conclusions borne out by the TEM results. Inset of Fig. 4.4B shows that the absorption at 610 nm increases linearly with film thickness, indicating that the gold nanoparticle multilayers grow in a lamellar fashion. Thus the above studies demonstrate that the spontaneous reduction of aqueous chloroaurate ions by 4-HDA Langmuir monolayer lead to the formation of highly oriented, flat gold nanosheets and nanoribbons at the air-water interface.

4.3 Synthesis of gold nanostructures by reduction of chloroauric acid using alkylated tyrosine (AT)

4.3-1 Synthesis of alkylated tyrosine (AT)

(a) *N-(tert-Butyloxycarbonyl)-O-(benzyl)-tyrosinyl octadecylamine*

To a stirred clear solution of N-(tert-butyloxycarbonyl)-O-(benzyl)-tyrosine (0.20 g, 0.53 mmol) and 1-hydroxybenzotriazole (HOBt) (0.14 g, 1.036 mmol) in anhydrous DMF (5 mL) was added diisopropylcarbodiimide (0.1 mL, 0.64 mmol), followed by octadecylamine (0.16 g, 0.59 mmol). The solution was stirred at room temperature under

nitrogen atmosphere overnight. TLC indicated formation of the product. The solvent was removed under vacuum and the residue taken up in aqueous sodium bicarbonate (15 mL) and extracted with ethyl acetate (15 mL 6 3). The organic extracts were dried over sodium sulfate and evaporated to obtain 0.49 g crude product, which was purified by column chromatography on silica gel to get 0.28 g pure product (83.5% yield). ^{1}HNMR(CDCl$_3$): d 7.39 (m, 5H), 7.09 (d, 2H, J ~8.06 Hz), 6.91 (d, 2H, J ~ 8.06 Hz), 5.63 (br s, 1H), 5.02 (br s, 3H), 4.18 (m, 1H), 3.12 (m, 2H), 2.95 (m, 2H), 1.40 (s, 9H), 1.24 (m, 32H), 0.87 (t, 3H, J ~ 6.59 Hz).

(b) *N-(tert-Butyloxycarbonyl)-tyrosinyl octadecylamine*

To a solution of N-(tert-butyloxycarbonyl)-O-(benzyl)-tyrosinyl octadecylamine (0.09 g, 0.14 mmol) in methanol (5 mL) was added 10% Pd–C (0.01 g, 11% by weight). The reaction mixture was hydrogenated in a Parr hydrogenation apparatus for 4 h at 50 psi. TLC examination indicated completion of the reaction. The catalyst was filtered off and the filtrate was concentrated under vacuum to obtain N-(tert-butyloxycarbonyl)-tyrosinyl octadecylamine (0.076 g, 99% yield) as a pure white solid.

^{1}H NMR (CDCl$_3$): d 7.00 (d, 2H, J ~ 8.79 Hz), 6.74 (d, 2H, J ~8.79 Hz), 5.83 (m, 1H), 5.13 (m, 1H), 4.21 (m, 1H), 3.14 (m, 2H), 2.94 (m, 1H), 1.41 (s, 9H), 1.30 (m, 2H), 1.24 (s, 30H), 0.86 (t, 3H, J ~ 6.59 Hz).

(c) *Tyrosinyl octadecylamine*

The N-(tert-butyloxycarbonyl)-tyrosinyl octadecylamine (0.08 g, 0.15 mmol) was dissolved in dry dichloromethane (1 mL). To this, 1 mL of trifluoroacetic acid was added and stirring was continued at room temperature for 20 min, when TLC examination indicated completion of the reaction. The solvents were completely removed by evaporation under vacuum and co-evaporation with dichloromethane. A gummy product (0.08 g, 97% yield) was obtained which solidified on standing.

^{1}H NMR (CDCl$_3$ 1 DMSO-d6): d 6.89 (d, 2H, J ~8.75 Hz), 6.62 (d, 2H, J ~8.34 Hz), 3.90 (t, 1H, J ~7.15 Hz), 2.91–3.04 (m, 2H), 2.90 (d, 2H, J ~7.15 Hz), 1.23 (m, 2H), 1.08 (s, 30H), 0.71 (t, 3H, J ~ 6.75 Hz and 7.16 Hz). C.

4.3-2 Synthesis of gold nanoparticles at a liquid–liquid interface using alkylated tyrosine

In a typical experiment, 25 mL of a 10^{-4} M aqueous solution of HAuCl$_4$ was taken in a beaker along with 25 mL solution of 2×10^{-4} M AT in chloroform. Considering AT as a 2 e$^-$ donor, three equivalents of AT are required for the reduction of two equivalents of AuCl$_4^-$ ions and hence the ratio of AT:Au(III) was maintained at 2:1 where AT molecules are present in excess. The biphasic mixture was stirred vigorously on a magnetic stirrer for 6 h that resulted in a reddish pink color in the organic phase. The chloroform was removed by rotary evaporation; the sample was washed repeatedly with ethanol and the gold nanoparticles obtained as a dry powder. The AT-capped gold nanoparticles could be readily redispersed in chloroform, hexane and toluene.
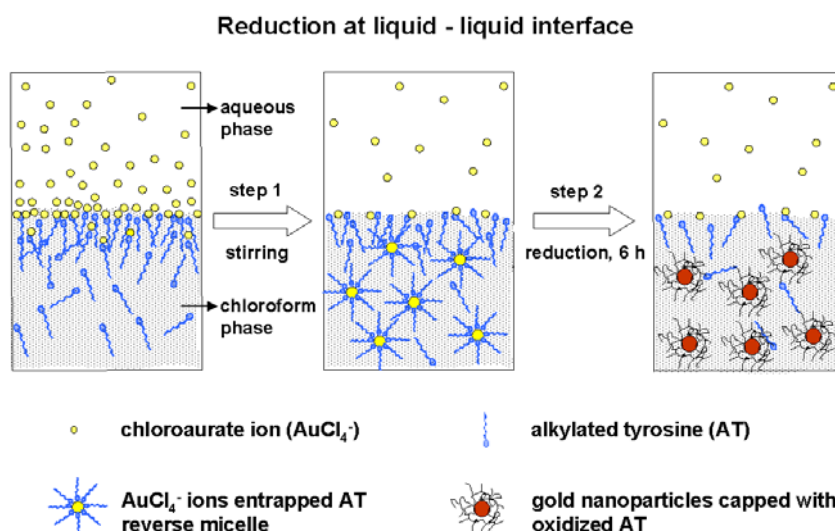
Scheme 4.1 (A) Diagram showing, step 1: hydrophobization and phase transfer of chloroaurate ions from an aqueous to a chloroform phase by stirring the aqueous chloroauric acid solution with the solution of alkylated tyrosine (AT) in chloroform; step 2: reduction of chloroaurate ions (entrapped in AT reverse micelle) by AT and formation of spherical gold nanoparticles capped and stabilized by oxidized AT.

4.3-2a *UV-vis spectroscopic analysis*

The inset of Fig. 4.5A shows a picture of test tubes containing the biphasic mixture of aqueous HAuCl$_4$ and AT in chloroform before (test tube a) and after the reaction for 6 h under continuous stirring at room temperature (test tube b). The

chloroform phase, which is initially colorless, takes on a reddish pink hue after reaction indicating formation of gold nanoparticles in the organic phase. Fig. 4.5A shows the UV-vis spectra recorded from the organic phase as a function of time of reaction of aqueous $AuCl_4^-$ ions with AT in chloroform. Curves 1, 2, 3 and 4 correspond to the spectra recorded after 2 min, 2 h, 4 h and 6 h of reaction, respectively.
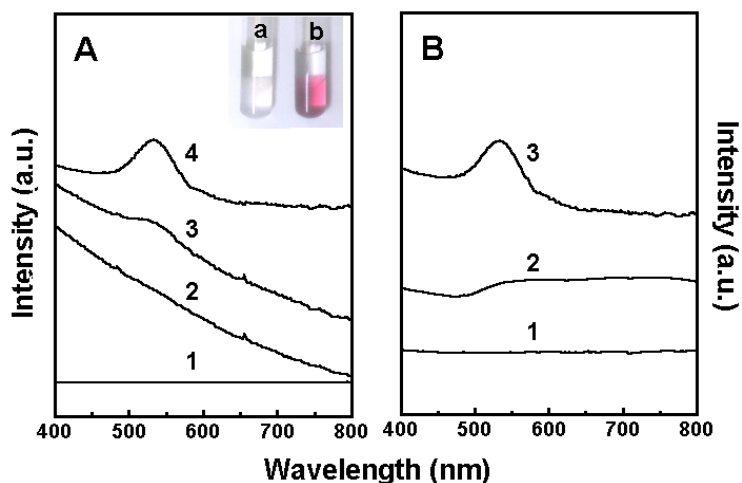

Figure 4.5 (A) UV-vis spectra of the chloroform phase recorded as a function of time of reaction of 10^{-4} M aqueous $HAuCl_4$ solution with 2×10^{-4} M chloroform solution of AT. Curves 1, 2, 3 and 4 in the figure correspond to the spectra recorded at time t ~ 0 h, 2 h, 4 h and 6 h of reaction, respectively. The inset shows a picture of the test tubes containing the biphasic mixtures of AT in chloroform (lower phase) and aqueous $HAuCl_4$ (upper phase) before (test tube a) and after (test tube b) the reaction. **(B)** UV-vis spectra of 10^{-4} M aqueous $HAuCl_4$ solution after reaction with 2×10^{-4} M tyrosine at room temperature (curve 1) and under boiling conditions (curve 2). Curve 3 corresponds to the UV-vis spectrum recorded from the chloroform phase after reaction of AT with aqueous $AuCl_4^-$ ions at a liquid–liquid interface at room temperature (identical to curve 4 in fig. 4.5A).

The increase in the surface plasmon resonance centered at ca. 535 nm with time indicates formation of gold nanoparticles in the chloroform phase and that the density of the particles increases steadily during this period of reaction. We would like to mention that after 6 h of reaction, the intensity of the surface plasmon resonance band does not increase further, indicating completion of reaction in this time interval. Under stirring conditions, the amine groups in the AT molecules are expected to be completely protonated leading to electrostatic complexation with $AuCl_4^-$ ions at the water–chloroform interface followed by transfer of $AuCl_4^-$ ions from the aqueous to the

chloroform phase. We believe that the $AuCl_4^-$ ions become entrapped in the hydrophilic cavities of the reverse micelle-like structures formed by the AT molecules, which enables the transfer of gold ions from the aqueous to the organic phase as shown in scheme 4.1. The solution of gold nanoparticles in chloroform was extremely stable over time, indicating effective capping of the nanoparticles by oxidized AT.

It would be instructive to compare AT reduction of gold ions with the reduction of aqueous gold ions directly using the amino acid tyrosine. Fig. 4.5B shows the UV-vis spectra recorded from 10^{-4} M aqueous $HAuCl_4$ solution after reaction with 2 x 10^{-4} M tyrosine for 6 h at room temperature (curve 1) and under boiling conditions (curve 2). For comparison, the UV-vis spectrum of gold nanoparticles formed in chloroform by the reaction of aqueous $AuCl_4^-$ ions with AT at room temperature as discussed earlier is shown (curve 3). The absence of a clear surface plasmon resonance in the case of the room temperature reduction of gold ions by pure tyrosine (curve 1) indicates that tyrosine does not readily reduce $AuCl_4^-$ ions under these conditions. Boiling the gold ion–tyrosine reaction mixture does lead to the formation of gold nanoparticles in solution (curve 2) but the presence of a broad absorption band indicates considerable aggregation of the gold nanoparticles in solution. A highlight of this part of the work is the finding that after alkylation, tyrosine is capable of rapid and facile reduction of gold ions at room temperature (curve 3). The exact reason for the increase in reducing capability of tyrosine after alkylation is not fully understood. As will be shown below, Langmuir monolayers of AT on aqueous chloroauric acid solution also lead to facile reduction of gold ions and therefore the role of the solvent, chloroform, in enhancing the reduction ability of AT may be ruled out.

4.3-2b *Transmission electron microscopy results*

Drop-coated film of AT-capped gold nanoparticles shows a number of highly polydisperse spherical gold nanoparticles at low magnification, which assemble into a close-packed structure, presumably during evaporation of the solvent, chloroform. It is observed from TEM image (Fig. 4.6A,B) that although close-packed, the gold nanoparticles are well separated from each other with an apparently uniform inter-particle

separation. This indicates that the gold nanoparticles are capped by an oxidized product of AT that prevents physical contact between the particles and also provides sufficient hydrophobicity to the gold nanoparticles to enable their dispersion in chloroform. At higher magnification, the morphology of the gold nanoparticles is observed more clearly (Fig. 4.6B). Fig. 4.6 C shows the selected area electron diffraction pattern recorded from the gold nanoparticles shown in Fig. 4.6A. A number of diffuse rings are observed in the electron diffraction pattern and could be indexed based on the fcc structure of gold. The presence of diffuse rings suggests that the gold nanoparticles are crystalline in nature. Particle size distribution (PSD) measured from 150 particles from Fig. 4.6A and other similar images yielded an average particle size of 42 ± 1.3 nm.
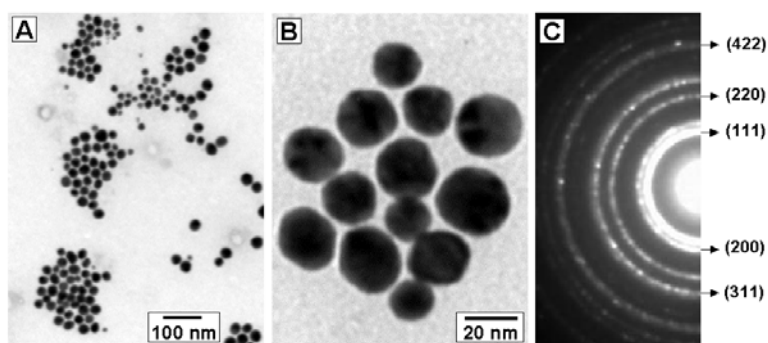

Figure 4.6 (A,B) Representative TEM pictures of AT-reduced gold nanoparticles synthesized in chloroform (see text for details). **(C)** Selected area electron diffraction pattern recorded from the gold nanoparticles shown in fig. 4.6A.

4.3-2c *X-ray diffraction analysis*

Fig. 4.7A shows the XRD pattern recorded from a drop coated film of AT-stabilized gold nanoparticles synthesized in chloroform on a glass substrate. From the XRD pattern, prominent Bragg reflections at 2θ values of 38.2°, 42.2°, 66.4° and 79.5° are observed which correspond to the (111), (200), (220) and (311) Bragg reflections of fcc gold, respectively, and are thus in agreement with the electron diffraction results discussed above [23]. It is clear from the above measurements that the AT molecules reduce $AuCl_4^-$ ions at the liquid–liquid interface leading to the formation of stable gold nanoparticles capped by oxidized AT in chloroform.
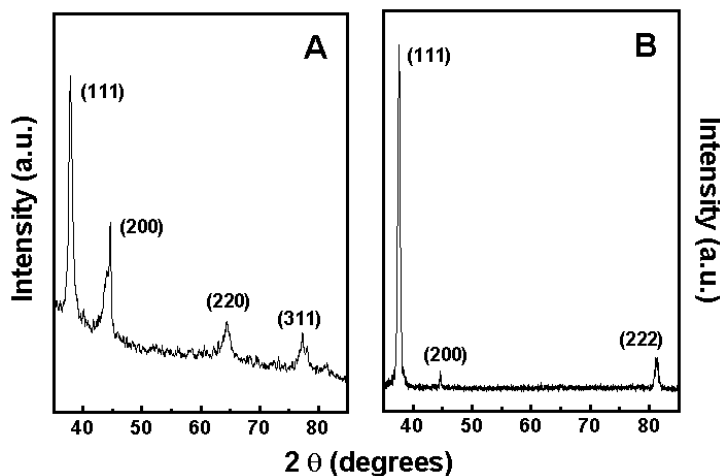
Figure 4.7 (A) XRD pattern recorded from a drop-coated film of AT-reduced gold
nanoparticles in chloroform (see text for details). **(B)** XRD pattern recorded
from a 24 monolayer (ML) LB film of AT-reduced gold nanoparticles at the
air–water interface, both deposited on a glass substrate.

4.3-3 Synthesis of gold nanoparticles at the air–water interface using alkylated tyrosine Langmuir monolayer

In a typical experiment, 75 μL of AT in chloroform (concentration 1 mg/mL) was
spread on surface of 10^{-4} M aqueous $HAuCl_4$ solution in a LB trough. Measurement of π–
A isotherms and deposition of gold-AT complex monolayers on different substrates for
further analysis was followed in the same way as described in chapter 2.

4.3-3a *Surface pressure-Area (π-A) isotherm results*

The above study shows that AT molecules reduce $AuCl_4^-$ ions spontaneously and
lead to the formation of stable hydrophobized gold nanoparticles of nearly spherical
shape in chloroform. The reducing capability of AT coupled with the in-built anisotropy
of the air–water interface provides one with the interesting option of using Langmuir
monolayers of AT in the highly localized formation of gold nanoparticles by the
spontaneous reduction of chloroaurate ions in the subphase. Fig. 4.8 shows pressure–area
(π–A) isotherms recorded at room temperature and at time intervals of 15 min., 2 h, 6 h,
10 h and 20 h after spreading the AT monolayer on the 10^{-4} M aqueous $HAuCl_4$ solution
as the subphase. At pH 3.7 of the subphase electrostatic complexation of $AuCl_4^-$ ions with
the cationic Langmuir monolayer is expected to occur in a manner similar to that

occurring at the liquid–liquid interface. π–A isotherm measurements show a large expansion of the monolayer from ca. 37 Å^2 /molecule at time t ~ 15 min to ca. 55 Å^2 /molecule at t ~ 20 h.
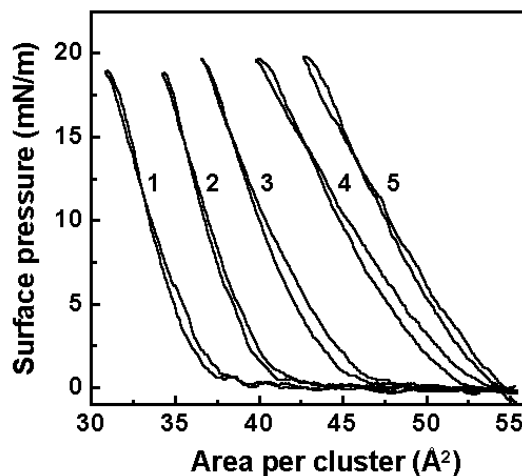

Figure 4.8 π–A isotherms recorded during one compression and expansion cycle of the AT Langmuir monolayer on the surface of the aqueous $HAuCl_4$ subphase as a function of time of spreading the monolayer. Curves 1-5 correspond to the isotherms recorded at time 15 min, 2 h, 6 h, 10 h and 20 h respectively after spreading the monolayer.

The liftoff area after equilibration of the $AuCl_4^-$ ions at the air–water interface (determined to be 55 Å^2 /molecule) is considerably larger than the liftoff area for the uncomplexed AT molecules (ca. 35 Å^2/molecule), which indicates complexation of $AuCl_4^-$ ions to the charged AT monolayer. It was observed that the AT monolayer collapsed at a surface pressure close to 23 mN/m and, consequently, the π–A isotherms with time were recorded to a limiting pressure of 20 mN/m (Fig. 4.8). From the π–A isotherm measurements, a region of reasonable incompressibility is seen to occur up to surface pressures of ca. 20 mN/m and, therefore, multilayer films of the AT–Au complex of different thickness were transferred onto hydrophobized quartz, TEM grids and Si (111) substrates for additional analysis at a surface pressure of ca. 15 mN/m.

4.3-3b *Transmission electron microscopy results*

The shape of the gold nanostructures formed at the air–water interface was studied by recording TEM images of a monolayer of the AT-complexed particles after complete reduction of chloroaurate ions.
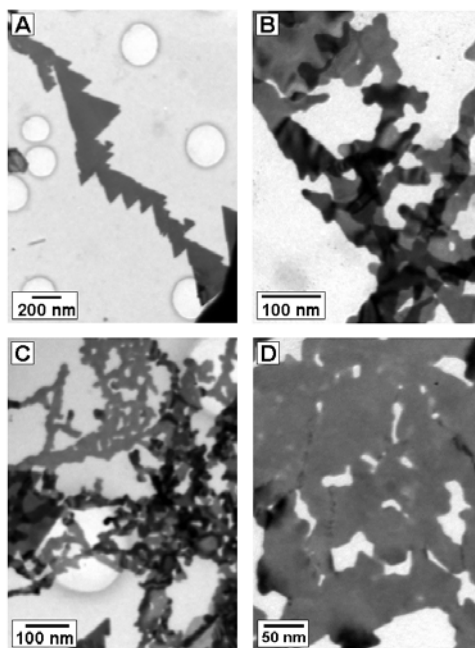
Figure 4.9 (A–D) Representative TEM images recorded at different magnifications from one monolayer of AT-reduced gold nanoparticles formed at the air–water interface and transferred onto a carbon-coated TEM grid by vertical lifting.

Fig. 4.9A–D show representative TEM images of a 2 ML (monolayer) of the AT–gold nanofilm recorded 36 h after spreading of the AT monolayer on the surface of 10^{-4} M HAuCl$_4$. It is clear from the images that a large concentration of very thin and flat gold nanoribbons/nanosheets is obtained at the air–water interface, in contrast to the spherical gold nanoparticles obtained by the reduction of gold ions by AT in chloroform. These results are similar to the results obtained in case of HDA-reduced gold nanoparticles both at liquid-liquid and air-water interfaces. In the case of the air–water interface, reduction of gold ions is localized to a quasi two-dimensional surface since the reducing AT molecules are restricted to the interface owing to their amphiphilicity. This leads to a high degree of anisotropy in the shape of the nanostructures formed [scheme shown on cover page of chapter]. In the case of the liquid–liquid interface, initially the AT molecules are concentrated at the interface because of their amphiphilicity. However under vigorous stirring conditions, complexation of AuCl$_4^-$ ions with AT results in hydrophobization and transfer of AuCl$_4^-$ ions from water to the chloroform phase

[scheme 4.1] and hence further reduction of gold ions (symmetrically surrounded by AT molecules) takes place in the chloroform phase and not at the water–chloroform interface. Thus, we speculate that the dramatic morphological variation of nanostructures formed at liquid–liquid and air–water interfaces is due to the different degrees of freedom (orientational and translational) experienced by the AT molecules and gold ions at the two interfaces as clearly shown in scheme 4.1 & scheme shown on cover page of this chapter. The nanoribbons/nanosheets formed at the air–water interface could be transferred by the Langmuir–Blodgett method on glass and quartz substrates for further study by XRD and UV-vis spectroscopy.

4.3-3c *X-ray diffraction analysis*

Fig. 4.7B shows the XRD pattern recorded from a 24 ML LB film of the gold nanosheets/nanoribbons transferred onto a glass substrate. This film shows a very strong gold (111) Bragg reflection at $2\theta \sim 38.2°$. The peaks corresponding to the (200) and (220) reflections are very weak indicating that the growth is highly face-selective. It is clear from the comparison of Fig. 4.7 A and B that highly oriented growth of the gold nanocrystals occurs in the case of gold ions reduced at the air–water interface by the AT Langmuir monolayer. In the case of synthesis of gold nanoparticles at a liquid–liquid interface there is no such specific orientation. This result is consistent with the TEM results that show the different morphologies of the gold nanocrystals in the two experiments. The above experiments prove the point that a single reducing agent with different degrees of freedom by applying different constraints can drastically alter the growth and evolution process of gold nanoparticles.

4.3-3d *UV-vis spectroscopic analysis*

Fig. 4.10A shows the UV-vis spectra recorded from LB films of the AT–gold nanoribbon complexes of different thickness deposited on quartz substrates. A broad absorption band centered at ca. 610 nm is observed that increases in intensity with increasing number of monolayers in the LB film (inset of Fig. 4.10A). The absorption at 610 nm is due to excitation of surface plasmon modes in the gold nanoparticles. This

absorption band is red shifted and broadened relative to the narrow absorption band at 534 nm observed for gold nanoparticles synthesized in chloroform (Fig. 4.5A).
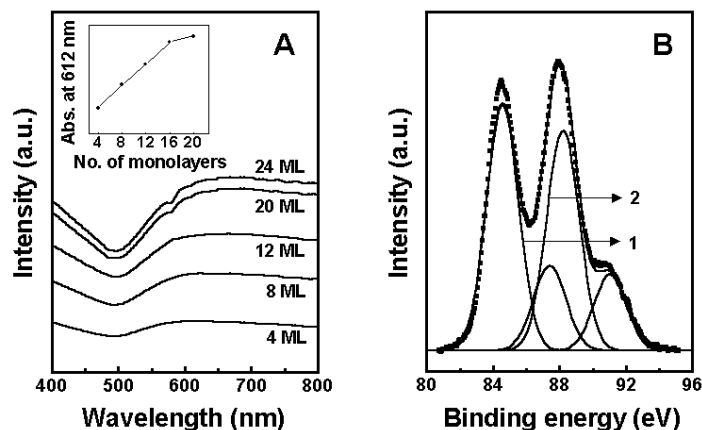

Figure 4.10 **(A)** UV-vis spectra recorded from LB films of AT-reduced gold nanosheets of different thickness (number of monolayers indicated next to the respective spectrum) deposited on quartz substrate. The inset is a plot of the intensity of the surface plasmon resonance maximum (absorbance at 610 nm) as a function of the number of monolayers of AT-capped gold nanoparticles in the LB films. The solid line is an aid to the eye and has no physical significance. **(B)** Au 4f core level spectrum recorded from a 24 ML thick LB film of AT-reduced gold nanoparticles deposited on a Si (111) substrate and stripped into two chemically distinct spin–orbit components (see text for details).

The shift and broadening of the resonance in the LB films indicates anisotropy in the particles and is also supported by the TEM results. The inset of Fig. 4.10A shows the intensity of absorption at 610 nm plotted as a function of the number of monolayers. The monotonic and almost linear increase in the intensity of the absorption band with film thickness indicates that similar amounts of the nanogold–AT monolayers are uniformly deposited during each cycle due to growth of gold multilayers in a lamellar fashion.

4.3-3e *X-ray photoelectron spectroscopic analysis*

A 24 ML LB film of AT-capped gold nanoparticles was deposited on a Si (111) substrate and analyzed by XPS. The general scan spectrum showed the presence of strong C 1s, N 1s and Au 4f core levels with no evidence of impurities. The film was sufficiently thick and, therefore, no signal was measured from the substrate (Si 2p core level). The Au 4f core level recorded from the LB film deposited 36 h after spreading the AT monolayer on aqueous $HAuCl_4$ acid solution is shown in Fig. 4.10B. The spectrum

was background corrected using the Shirley algorithm [24] prior to curve resolution. The Au 4f core level spectrum recorded from the LB film could be deconvoluted into two spin–orbit pairs. The two chemically distinct Au $4f_{7/2}$ components were centered at binding energies (BEs) of 84.5 eV and 87.5 eV (labelled 1 and 2 in Fig. 4.10B, respectively). The low BE component is attributed to electron emission from Au^0 oxidation state in the metal [23] while the smaller, high BE component arises from the presence of unreduced Au^{+3} ions in the LB film. The XPS results thus show that a major fraction of the $AuCl_4^-$ ions are reduced to metallic Au by the AT Langmuir monolayer at the air-water interface. Based on charge neutrality considerations, it would be expected that one $AuCl_4^-$ ion would bind to one protonated AT molecule. However, since the conversion of Au^{+3} to Au^0 is a 3 e^- transfer process, it is expected that three equivalents of AT molecules are required for the reduction of two equivalents of gold ions (considering AT as a 2 e^- donor). Hence all the $AuCl_4^-$ ions bound to the interface would not be fully reduced to Au^0 by the AT Langmuir monolayer, evidence of which is clearly seen by the presence of the fraction of unreduced $AuCl_4^-$ ions in the LB films identified by XPS.

4.3-3f *Nuclear Magnetic resonance spectroscopy*

In order to analyze the oxidation product of AT molecules formed consequent to the reduction of $AuCl_4^-$ ions, AT-capped nanoparticles were separated out from the organic solvent and also from the LB films and redispersed in $CDCl_3$ + DMSO-d_6 for ^1H NMR spectroscopic measurements. Curves 1, 2 and 3 in Fig. 4.11 correspond to the ^1H NMR spectra recorded from pure AT, AT-capped gold nanoparticles formed at the liquid–liquid interface and LB films of AT-reduced gold nanostructures formed at the air–water interface dispersed in $CDCl_3$ + DMSO-d_6, respectively. The NMR spectrum of AT (curve 1) shows a number of prominent resonances that are identified in the schematic given in the inset of the figure. The AT molecule shows chemically shifted protons at 6.8 and 6.6 ppm in curve 1 and are assigned to the two sets of aromatic protons labeled j and i, respectively, in the schematic. The chemically shifted peaks centered at 2.9 - 3.0 ppm, 1.2, 1.0 and 0.7 ppm correspond to the α-CH_2, β-CH_2, methylene and methyl protons in the C_{18} hydrocarbon chain, respectively. In curves 2 and 3 (AT-reduced

gold nanoparticles at the liquid–liquid and air–water interfaces, respectively) there is a complete disappearance of the peaks at 6.8, 6.6, 2.9 - 3.0 and at 1.2 ppm.
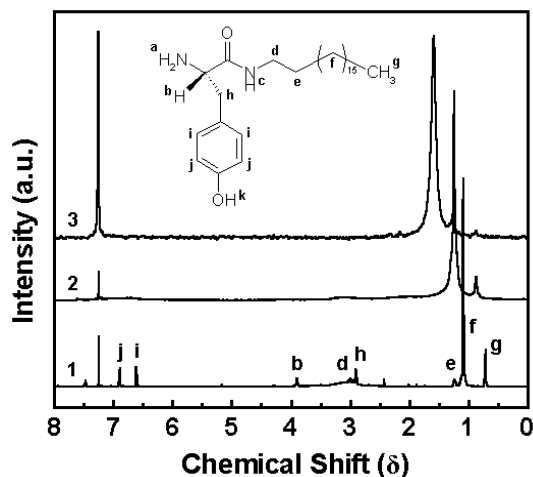

Figure 4.11 ^{1}H NMR spectra recorded from pure AT (curve 1); AT reduced gold nanoparticles at the liquid–liquid interface synthesized in chloroform and then dispersed in CDCl₃ + DMSO-d₆ (curve 2); LB film of AT-reduced gold nanoparticles after dissolving in CDCl₃ + DMSO-d₆ (curve 3). The inset is a schematic of the AT molecule used in this study identifying the protons that appear in the NMR spectra.

Disappearance of signatures of aromatic protons in the ^{1}H NMR spectra indicate polymerization of AT following the reduction of $AuCl_4^-$ ions. Oxidative oligomerization/polymerization of aromatic diamines in the presence of oxidants such as salts of various transition metals is wellknown in the literature [25]. Thus, we believe that the formation of gold nanoparticles at the liquid–liquid and air–water interfaces is accompanied by the polymerization of AT. It is clear from the NMR results that unreacted AT is not present on the gold nanoparticles formed at both the liquid–liquid and air–water interfaces. At this stage, the extent of polymerization is not comprehensible from ^{1}H NMR studies. This would require separation of the polymer from the nanoparticles for detailed analysis.

Above results reveal that the ability of the amino acid tyrosine to reduce gold ions can be enhanced by alkylation. Alkylation of tyrosine enables the use of this multifunctional molecule in the spontaneous reduction of aqueous gold ions at both the

liquid–liquid and air–water interfaces with dramatic differences in the shape of the gold nanoparticles formed.

4.4 Synthesis of silver nanostructures at air-water interface using pentadecylphenol (PDP) Langmuir monolayer

In a typical experiment, 100 μL chloroform solution of 3-PDP (1mg/mL) was spread on the surface of 10^{-4} M aqueous Ag_2SO_4 solution (pH adjusted to 10 using 1M aqueous KOH solution) as the subphase LB trough. Measurements of π–A isotherms and multilayer films of the 3-PDP-reduced silver nanoparticles of different thickness were formed by the LB technique in the same way as described in chapter 2. Reduction of silver ions at the air-water interface was monitored by *in-situ* UV-vis spectroscopy measurements of the compressed monolayer (compressed to a surface pressure of 15 mN/m) at different time intervals.

4.4-1 Surface pressure-Area (π-A) isotherm and UV-vis spectroscopy results

It was observed in our laboratory that 3-PDP can reduce the silver ions under alkaline conditions to form nanoparticles in both aqueous and organic phases [26]. Since 3-PDP is an amphiphilic molecule and can form stable Langmuir monolayers on the surface of water, it motivated us to study the reduction of silver ions at the air-water interface by spreading 3-PDP on the surface of aqueous Ag_2SO_4 solution under alkaline conditions. Fig. 4.12A shows the π-A isotherms recorded after stabilization of the 3-PDP Langmuir monolayer on different subphases; curve 1 is the isotherm recorded from the monolayer spread on the surface of deionized water while curves 2 and 3 are the isotherms recorded on the surface of aqueous 10^{-4} M Ag_2SO_4 solution (pH 6.5) and aqueous 10^{-4} M Ag_2SO_4 solution adjusted to pH 10 respectively. The liftoff molecular area of 3-PDP on deionized water (curve 1) is observed to be ca. 50 $Å^2$/molecule. The liftoff area in the π-A isotherms recorded on the 10^{-4} M Ag_2SO_4 solution (pH 6.5, curve 2) and aqueous 10^{-4} M Ag_2SO_4 solution at pH 10 (curve 3) increases to ca. 60 $Å^2$/molecule indicating some interaction of the aqueous Ag^+ ions with the phenolic head group of 3-PDP. The most significant changes in the π-A isotherms are observed in the collapse pressures and hysteresis of the isotherms (compare curves 1-3). The collapse

pressure is the least and hysteresis is maximum in the case of 3-PDP on 10^{-4} M Ag$_2$SO$_4$ solution at pH 10 indicating strong interaction of the monolayer with subphase silver ions under these conditions.
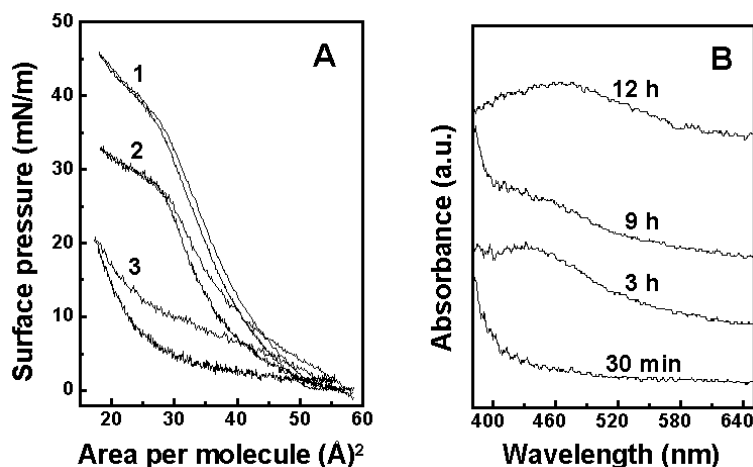

Figure 4.12 (A) π-A isotherms recorded after the stabilization of the 3-PDP Langmuir monolayer on the surface of: pure water (curve 1); aqueous 10^{-4} M Ag$_2$SO$_4$ solution, (curve 2); and alkaline 10^{-4} M Ag$_2$SO$_4$ (pH adjusted to 10 using 1 M KOH) solution (curve 3). **(B)** UV-vis spectra of the 3-PDP monolayer on the surface of alkaline 10^{-4} M Ag$_2$SO$_4$ (pH 10) solution measured *in situ* at different time intervals after spreading the monolayer (time indicated next to the respective curve). The curves have been shifted vertically for the clarity.

The function of KOH is to ionize the phenolic group of 3-PDP into phenolate anion and the resulting electron transfer from these phenolate ions to silver ions leads to the formation of silver nanoparticles capped by the quinone group of the oxidized 3-PDP molecule (scheme 4.2).
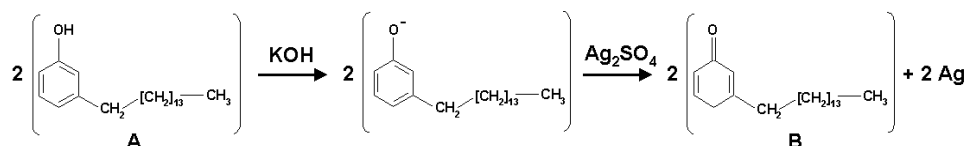
Scheme 4.2 The structure of 3-PDP before **(A)** and after oxidation **(B)** consequent to reduction of the silver ions and formation of silver nanoparticles.

Under alkaline subphase conditions, metallic luster could readily be seen at the interface 1-2 hours after spreading the monolayer, which then develops as a function of time eventually forming a yellow film of silver nanoparticles at the air-water interface

after about 12 hours of spreading the monolayer. In this experiment (10^{-4} M Ag_2SO_4 solution at pH 10), we have monitored the reduction of the silver ions at the air-water interface by *in-situ* UV-vis spectroscopic measurements of the monolayer in reflection mode. Fig. 4.12B shows the UV-vis absorption curves obtained from the monolayer of silver nanoparticles recorded at different time intervals after spreading the 3-PDP monolayer. No absorption is observed during the initial stages as shown by the curve recorded 30 minutes after spreading the monolayer. However, as the reduction proceeds, an absorption band centered at ca. 430 nm is observed (3 h), which arises due to excitation of surface plasmon modes in the silver nanoparticles. This absorption band broadens and eventually shifts to ca. 475 nm as seen in the spectrum recorded 12 hours after spreading the 3-PDP monolayer. The broadening and red shift in the plasmon absorption band can be attributed to increasing interactions between silver nanoparticles that are assembled on the surface of water as the density of the nanoparticles builds up with time [27] at the air-water interface.

4.4-2 Transmission electron microscopy results

The growth and assembly of the spontaneously formed silver nanoparticles at the air-water interface was followed by TEM measurements by depositing a monolayer of the 3-PDP-reduced silver nanoparticles on carbon coated TEM grids at different times of reaction. Figs. 4.13A,C,E and G show representative TEM images (recorded at low magnification) of the silver nanoparticles formed at air-water interface after 30 minutes, 3 h, 9h and 12 h of spreading the 3-PDP monolayer while Figs. 4.13B,D,F and H are the corresponding TEM images recorded at higher magnification. The lower magnification images (A,C,E and G) reveal that the nanoparticles assemble to form domains whose coverage and size increases from about 200 nm (at time t = 30 min) to about 10 μm (at time t = 12 h). The individual nanoparticles and their 2-dimensional (2D) assembly in the domains is clearly seen in the higher magnification images (B,D,F and H). A comparison of the high magnification images shows that there is no detectable change in the average silver nanoparticle size as a function of time of reaction of the 3-PDP Langmuir monolayer with the aqueous silver ions; however the morphology of the domains does

change with time of reaction from one of open, string-like structures (Fig. 4.13B,D) to compact, circular and hexagonally packed assemblies of nanoparticles (Fig. 4.13F,H).
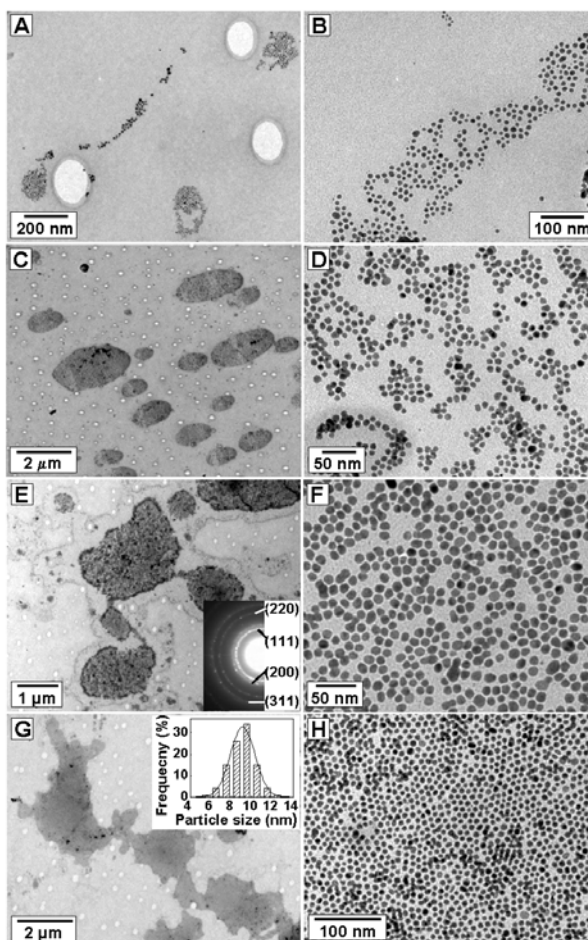

Figure 4.13 Representative TEM images of the 3-PDP-reduced silver nanoparticles formed at the air-water interface as a function of time of reaction - time: t = 30 min **(A)**, **(B)**; t = 3 h **(C)**, **(D)**; t = 9 h **(E)**, **(F)** and t = 12 h **(G)**, **(H)**. The inset of (E) shows the electron diffraction pattern obtained from the nanoparticles shown in image (H). The inset of (G) corresponds to the particle size distribution histogram determined from 100 particles shown in image (H) and other similar images. The solid line is a Gaussian fit to the data.

Thus, it is clear from TEM results that the red shift in the surface plasmon resonance observed from monolayers of the 3-PDP-reduced Ag nanoparticles (Fig. 4.12B) is due to the spontaneous formation and 2D organization of nanoparticles [27].

The inset of Fig. 4.13E shows the selected area electron diffraction pattern recorded from the nanoparticles shown in Fig. 4.13H.
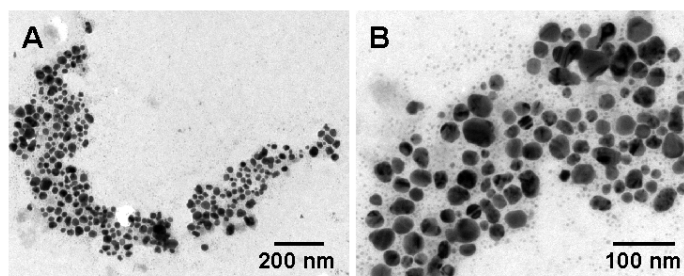

Figure 4.14 (A,B) Representative TEM images of silver nanoparticles formed in the subphase by the reduction of silver ions under alkaline conditions using 3-PDP Langmuir monolayer recorded at different magnifications.

The characteristic rings in the diffraction pattern reveal the crystalline nature of the nanoparticles and could be indexed as the (111), (200), (220) and (311) allowed Bragg reflections from fcc silver. The inset of Fig. 4.13G shows the particle size distribution histogram measured from 100 particles from Fig. 4.13H and other similar images. The solid line is a Gaussian fit to the particle size distribution histogram and yielded an average particle size of 9.0 ± 1.2 nm. The particle size in the case of the nanoparticles formed at the air-water interface is marginally less than those that are formed in the biphasic reaction experiment (11.8 ± 1.6 nm) and may be due to constrained growth at the air-water interface. The high magnification TEM images also suggest that the interparticle separation is very uniform; an analysis of the interparticle separations yielded an average value of 1.5 ± 0.2 nm. This value is less than twice the length of 3-PDP molecules calculated empirically, indicating that the silver nanoparticles in the 2-D assemblies are packed with interdigitation of the hydrocarbon chains between neighboring particles. Along with the yellow colored monolayer of silver nanoparticles at the interface, a faint yellow color was also observed in the subphase indicating that partial reduction of the silver ions also occur in the subphase. TEM analysis of this solution shows that the nanoparticles in the subphase are polydisperse (size range 5 nm – 50 nm) and of very irregular shape (Fig. 4.14A, B). Hence, the 2D reduction of silver ions at the air-water interface using 3-PDP Langmuir monolayer results in the one-step

spontaneous formation of monodisperse silver nanoparticles assembled into close-packed domains that may then be transferred in the form of superlattices onto solid supports by the LB technique. We speculate that the excellent monodispersity of the silver nanoparticles synthesized at the air-water interface arises due to rapid capping of the silver nanoparticles by oxidized 3-PDP molecules that limits their growth to the initial nucleation stage. This suggests strong interaction of the oxidized 3-PDP molecules with the silver surface. It is well known that the polydispersity of nanoparticles increases during the growth phase and consequently, limiting nanoparticle growth by surface capping could explain the above results. The fact that the monodispersity of the silver nanoparticles in the aqueous phase was worse than for the particles in chloroform in the liquid-liquid interface experiment provides further support for this hypothesis – insufficient capping of the silver nanoparticles by the oxidized 3-PDP molecules renders them water dispersible and also enables them to grow more readily.
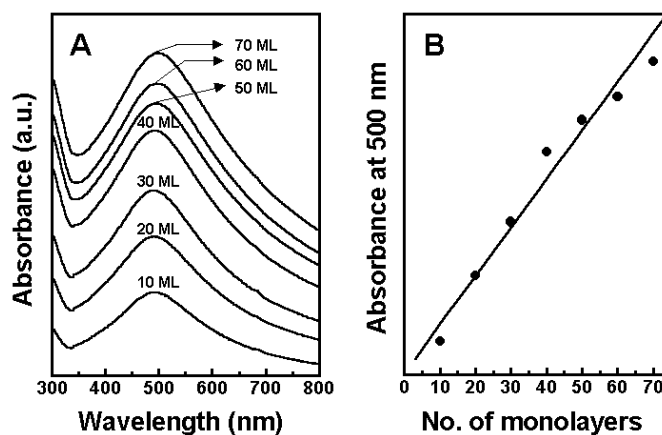
4.4-3 UV-vis spectroscopic analysis

Figure 4.15 **(A)** UV-vis absorption spectra of LB films of 3-PDP-reduced silver nanoparticles of different thickness deposited on quartz substrates (film thickness in terms of number of monolayers is indicated next to the respective curve). **(B)** Plot of the intensity of the surface plasmon resonance at 500 nm plotted against the number of monolayers in the LB films of silver nanoparticles on quartz substrate. The solid line is non-linear least squares fit to the data.

Fig.4.15A shows the UV-vis spectra recorded from films of silver nanoparticles of different thickness deposited on quartz substrates by the LB technique. The surface plasmon band increases monotonically with increasing film thickness (Fig. 4.15A) for

nanoparticles on the quartz substrate. Fig. 4.15B shows a plot of the intensity of absorption at λ_{max} (500 nm in this case) against the number of monolayers in the LB film. It is observed that the plasmon absorption peak intensity increases linearly with number of monolayers of silver nanoparticles in the LB film. This indicates that the density of silver nanoparticles in each of the layers in the LB film is (within detection limits) almost the same. The large red shift in the plasmon resonance band compared to that observed for the monolayer of silver nanoparticles (475 nm) is most probably due to a change in the refractive index of the film relative to the air-water interface.

4.4-4 X-ray photoelectron spectroscopic analysis

A chemical analysis of the 3-PDP-reduced silver nanoparticles was done by XPS measurements of a 30 ML LB film of the nanoparticles deposited on Si(111) substrate. Fig. 4.16A and B show the C1s and Ag 3d core level spectra recorded from this LB film respectively.
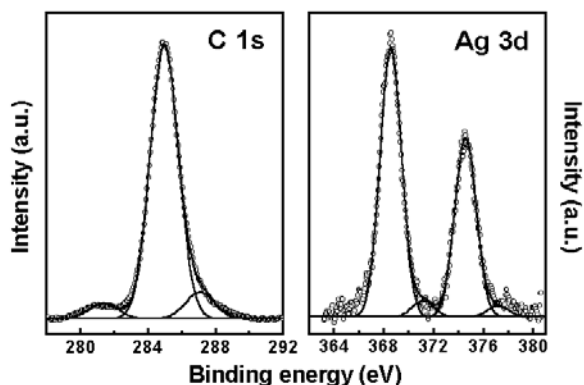

Figure 4.16 (A) C 1s and **(B)** Ag 3d XPS core level spectra recorded from a 30 ML thick LB film of 3PDP-reduced silver nanoparticles deposited on a Si (111) substrate. The solid lines are non-linear least square fits to the data.

The C1s signal could be deconvoluted into three chemically distinct components. The major component at 285 eV binding energy (BE) arises from carbons in the hydrocarbon chains of 3-PDP molecules capping the silver nanoparticles while the other two components at 281.3 eV and 287 eV can be assigned to the carbons in the aromatic ring of the 3-PDP molecules and carbonyl carbon respectively (scheme 4.2). The Ag 3d core level could be deconvoluted into two chemically distinct species with Ag $3d_{5/2}$ BEs

of 368 eV and 370.2 eV that are assigned to metallic silver (Ag^0) and unreduced silver ions (Ag^+) respectively indicating that a small percentage of unreduced silver ions are present in the LB films.

A simple one-step process for the synthesis of highly ordered, large domains of monodisperse silver nanoparticles by the spontaneous reduction of silver ions under alkaline conditions present in the subphase by 3-pentadecylphenol (PDP) Langmuir monolayers has been illustrated. Excellent quality superlattice LB films of the silver nanoparticles could easily be formed on suitable solid substrates.

References
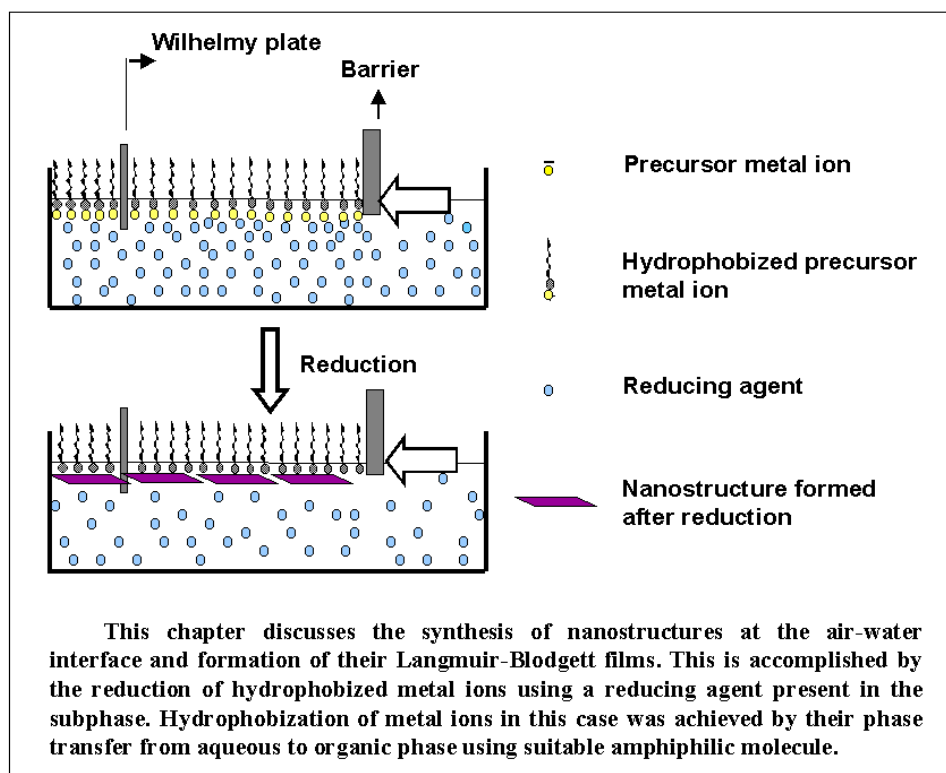
(1)   (a) El-sayed, M.A. *Acc. Chem. Res*. **2001**, *34*, 257. (b) Victor F. P.; Krishnan, K.M.; Alivisatos. A. P. *Science* **2001**, *291*,2115. (c) Sun, Y.; Xia**,** Y. *Analyst* **2003**, *128,* 686. (d) El-sayed, M.A. *Acc. Chem. Res.* **2004,** *37*, 326.

(2)   (a) Schmid, G. M. *Chem. Rev* **1992**, *92*, 1709. (b) Le Bars, J.; Specht, U.; Bradley, J. S.; Blackmond, D. G. *Langmuir* **1999**, *15*, 7621. (c) Li, Y.; Hong, X. M.; Collard, D. M.; El-Sayed, M. A. *Org. Lett*. **2000,** *2*, 2385. (d) Li, Y.; El-Sayed, M. A. *J. Phys. Chem. B* **2001,** *105*, 8938. (e) Dai, J.; Bruening, M. L. *Nano Lett.* **2002,** *2,* 497. (f) Yoo, J. W.; Hathcock, D.; El-Sayed, M. A. *J. Phys. Chem. A* **2002**, *106*, 2049.

(3)   (a) Jin, R.; Cao, Y. W.; Mirkin, C. A.; Kelly, K. L.; Schatz, G. C.; Zheng, J. G. *Science* **2001**, *294*, 1901. (b) Esumi, K.; Matsuhisa, K.; Torigoe, K. *Langmuir* **1995**, *11*, 3285. (c) Kameo, A.; Suzuki, A.; Torigoe, K.; Esumi, K. *J. Colloid Int. Sci.* **2001**, *241*, 289. (d) Leontidis, E.; Kleitou, K.; Kyprianidou-Leodidou, T.; Bekiari, V.; Lianos, P. *Langmuir* **2002**, *18*, 3659. (e) Brown, K. R.; Walter, D. C.; Natan, M. J. *Chem. Mater.* **2000**, *12*, 306. (f) Jana, N. R.; Gearheart, L.; Murphy, C. J. *J. Phys. Chem. B* **2001**, *105*, 4065. (g) Zhou, Y.; Wang, C. Y.; Zhu, Y. R.; Chen, Z. Y. *Chem. Mater.* **1999**, *11*, 2310. (h) Malikova, N.; Pastoriza-Santos, I.; Scheirhorn, M.; Kotov, N. A.; Liz-Marzan, L. M. *Langmuir* **2002**, *18*, 3694. (i) Zhu, Z.; Liu, S.; Palchik, O.; Koltypin, Y.; Gedanken, A. *Langmuir* **2000**, *16*, 6396.

(4)   (a) Chung, S.-W.; Markovich, G.; Heath, J. R. *J. Phys. Chem. B* **1998**, *102*, 6685. (b) Jana, N. R.; Gearhart, L.;. Murphy, C. J. *Chem. Comm.* **2001**, 617.

(5)   (a) Brown, K. R.; Walter, D. G.; Natan, M. J. *Chem. Mater.* **2000**, *12*, 306. (b) Johnson, C. J.; Dujardin, E.; Davis, S. A.; Murphy, C. J.; Mann, S. *J. Mater. Chem.* **2002**, *12*, 1765.

(6)   Peng, X.; Manna, L.; Yang, W.; Wickham, J.; Scher, E.; Kadanavich, A.; Alivisatos, A. P. *Nature* **2000**, *404*, 59.

(7)   Nikitenko, S. I.; Koltypin, Y.; Mastai, Y.; Koltypin, M.; Gedanken, A. *J. Mater. Chem.* **2002**, *12*, 1450.

(8)   Shankar, S. S.; Rai, A.; Ankamwar, B.; Singh, A.; Ahmad, A.; Sastry, M. *Nature Mater.* **2004**, *3*, 482.

(9)   Pinna, N.; Weiss, K.; Urban, J.; Pileni, M.-P. *Adv. Mater.* **2001**, *13*, 261.

(10)   (a) Sun, Y.; Mayers, B.; Herricks, T.; Xia, Y. *Nano Lett.* **2003**, *3*, 955. (b) Sun, Y.; Xia, Y. *Adv. Mater.* **2002**, *14*, 833. (c) Sun, Y.; Xia, Y. *Science* **2002**, *298*, 2176. (d) Sun, Y.; Xia, Y. *Adv. Mater.* **2003**, *15*, 695. (e) Sun, Y.; Mayers, B. T.; Xia, Y. *Nano Lett.* **2002**, *2*, 481. (f) Sun, Y.; Mayers, B.; Xia, Y. *Adv. Mater.* **2003**, *15*, 641. (g) Sun, Y.; Xia, Y. *J. Am. Chem. Soc.* **2004**, *126*, 3892.

(11)   Metraux, G. S.; Cao, Y.C.; Jin, R.; Mirkin, C. A. *Nano Lett.* **2003**, *3*, 519.

(12)   Cassagneau, T.; Caruso, F. *Adv.Mater.* **2002**, *14*, 732.

(13)   Martin, B. R.; Dermody, D. J.; Reiss, B. D.; Fang, M. M.; Lyon, L. A.; Natan, M. J.; Mallouk, T. E. *Adv. Mater.* **1999**, *11*, 1021.

(14)   van der Zande, B. M. I.; Bohmer, M. R.; Fokkink, L. G.; Schonenberger, C. *Langmuir* **2000**, *16*, 451.

(15)   Cepak, V. M.; Martin, C. R. *J. Phys. Chem. B* **1998**, *102*, 9985.

(16)   Govindaraj, A.; Satishkumar, B. C.; Nath, M.; Rao, C. N. R. *Chem. Mater.* **2000**, *12*, 202.

(17)   Fullam, S.; Cottell, D.; Rensmo, H.; Fitzmaurice, D. *Adv. Mater.* **2000**, *12*, 1430.

(18)   Yu, Y. Y.; Chang, S. S.; Lee, C. L.; Wang, C. R. C. *J. Phys. Chem.* **1997**, *101*, 6661.

(19) (a) Pike, J. K.; Byrd, H.; Morrone, A. A.; Talham, D. R. *J Am.Chem. Soc*. **1993**, *115*, 8497. (b) Ravaine, S.; Fanucci, G. E.; Seip, C.T.; Adair, J. H.; Talham, D.R. *Langmuir* **1998,** *14,* 708.

(20) Yi, K. C.; Mendieta, V. S.; Castanares, R. L.; Meldrum, F. C.; Wu, C.; Fendler, J. H. *J. Phys. Chem.* **1995**, *99*, 9869.

(21) Selvakannan, PR.; Mandal, S.; Pasricha, R.; Adyanthaya, S. D.; Sastry, M. *Chem. Comm.* **2002**, 1334.

(22) Zhou, Y.; Chen, W.; Itoh, H.; Naka, K.; Ni, Q.; Yamane, H.; Chujo, Y. *Chem. Comm*. **2001**, 2518.

(23) Leff, D. V.; Brandt, L.; Heath, J. R. *Langmuir* **1996**, *12*, 4723.

(24) Shirley, D. A. *Phys. Rev. B* **1972**, *5*, 4709.

(25) Li, X.-G.; Huang, M-R.; Duan, W.; Yang, Y.-L. *Chem. Rev*. **2002**, *102*, 2925.

(26) Swami, A.; Selvakannan, PR.; Pasricha, R.; Sastry, M. *J. Phys. Chem. B* **2004**, *108*, 19269.

(27) Taleb, A.; Petit, C.; Pileni, M. P. *J. Phys. Chem. B* **1998**, *102*, 2214.

C H A P T E R V

Synthesis of nanostructures by the reduction of precursor metal ions constrained to a monolayer at the air-water interface

This chapter discusses the synthesis of nanostructures at the air-water interface and formation of their Langmuir-Blodgett films. This is accomplished by the reduction of hydrophobized metal ions using a reducing agent present in the subphase. Hydrophobization of metal ions in this case was achieved by their phase transfer from aqueous to organic phase using suitable amphiphilic molecule.

5.1 Introduction

Shape control of nanoparticles is one of the important areas of nanoparticle research and methods developed for synthesizing nanoparticles of different shapes have already been discussed in Chapter 4. Chapter 4 further describes a novel method for the two-dimensional (2D) synthesis of highly oriented, flat, anisotropic nanostructures formed due to the localized reduction of metal ions in confined geometries using Langmuir monolayer as a reducing agent. To further extend this idea, it would be interesting to study the growth of metal nanoparticles by constraining the metal ions at the air–water interface as opposed to the use of Langmuir monolayer as a reducing agent in the process of synthesis of metal nanoparticles in constrained environment. The reduction here may be accomplished using an aqueous reducing agent in the subphase or by ultraviolet irradiation of the monolayer. Khomutov and coworkers have shown the synthesis of magnetic iron containing nanoparticles by ultraviolet decomposition of volatile precursor compound iron pentacarbonyl ($Fe(CO)_5$) spread on the surface of water along with stearic acid monolayer [1]. A similar strategy has been used by them for the synthesis of palladium and gold nanostructures by the chemical reduction of mixed monolayers of organometallic compounds such as $Pd_3(CH_3COO)_6$ and $Au(P(C_6H_5)_3)Cl$ respectively with stearic acid, arachidic acid or octadecyl amine on the surface of the aqueous subphase containing sodium borohydride ($NaBH_4$) as a reducing agent [2]. Flat, anisotropic nanostructures are obtained in case of ultraviolet decomposition of $Fe(CO)_5$ [1]. However the limitations of this method are first, that $Fe(CO)_5$ is a liquid at normal conditions with a tendency to evaporate slowly and hence the monolayer molecular composition is dependent on time, temperature and gas phase content that can result in changes of morphology of generated nanoparticles. Secondly the iron-containing nanostructures formed are amorphous in nature. Further, so far as the synthesis of palladium and gold nanoparticles is concerned [2], though the precursor organometallic compounds are spread on the surface of aqueous subphase along with the surfactants to slow down the nucleus coalescence and to stabilize grown nanoparticles against aggregation, their chemical reduction results in aggregated large spherical nanoparticles.

This may possibly be due to the phase separation of precursor organometallic compounds from surfactant molecules when spread on the surface of water.

In this chapter, we show the formation of highly anisotropic, flat gold nanostructures at the air–water interface by immobilizing chloroaurate ions at the interface and further reducing them with anthranilic acid present in the subphase. For the gold ions to be immobilized on the surface of water, they need to be rendered hydrophobic and this was accomplished by their phase transfer from aqueous to chloroform using phase-transfer molecules such as octadecylamine (ODA) and benzyldimethylstearylammonium chloride (BDSAC, molecular structure shown in inset of Fig. 5.1). While phase-transfer molecules such as tetraalkylammonium salts are routinely used in the synthesis of gold nanoparticles in organic media, [3] to the best of our knowledge, the use of the phase-transferred hydrophobized gold ions for growth of nanoparticles in constrained environments, such as that described in this chapter, has not been reported so far. Spreading of hydrophobized $AuCl_4^-$ ions on surface of aqueous subphase results in formation of uniform monolayer of gold ions on the surface of water since they are complexed with the surfactant as against the reported case [2] where precursor metal ions phase separate from the surfactant molecules and thus lead to the aggregated nanostructures after reduction. In the present study the reduction of gold ions at the air–water interface led to the formation of flat gold nanostructures exhibiting interesting fractal morphology that could be transferred by the Langmuir–Blodgett (LB) technique onto a variety of substrates leading to the formation of excellent multilayer films of the nanoparticles.

5.2 Synthesis of gold nanostructures at air-water interface by reduction of chloroaurate ions constrained to monolayer using benzyldimethylstearylammonium chloride (BDSAC) or octadecyl amine (ODA)

5.2-1 Hydrophobization of chloroaurate ($AuCl_4^-$) ions

10 ml of 10^{-3} M aqueous solution of chloroauric acid ($HAuCl_4$) was taken in a conical flask along with a 10 ml solution of 10^{-3} M surfactant ODA/BDSAC in chloroform giving immiscible layers of the colorless organic solution at the bottom of the

faint yellow colored aqueous $HAuCl_4$ solution. The phase transfer of $AuCl_4^-$ ions is achieved by their electrostatic interaction with the cationic head group of the surfactant in the organic phase. Rapid transfer (within 30 s) of the $AuCl_4^-$ ions from the aqueous phase into the organic phase was done under vigorous stirring conditions of the biphasic mixture (Scheme 1, step 1). The organic phase containing hydrophobized $AuCl_4^-$ ions after phase transfer was separated from the aqueous phase and diluted with chloroform to attain a concentration of 1 mg/mL of the surfactant (ODA or BDSAC) for further experiments.
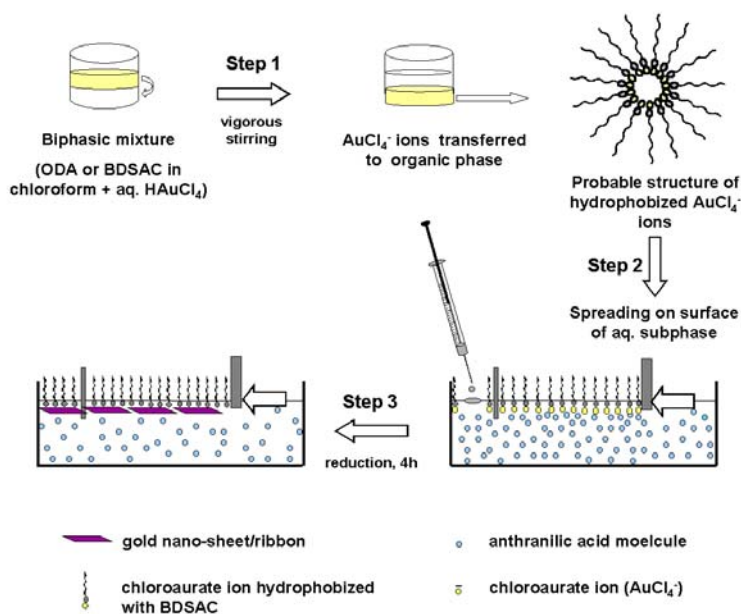
Scheme 5.1 Step 1: Hydrophobization of chloroaurate ions achieved by stirring the aqueous chloroauric acid solution with the solution of surfactant (ODA or BDSAC) in chloroform; **Step 2**: immobilization of chloroaurate ions at the air–water interface by spreading the monolayer of hydrophobized chloroaurate ions on the surface of an aqueous anthranilic acid solution; **Step 3**: Reduction of chloroaurate ions immobilized at the air–water interface by anthranilic acid solution present in the subphase leading to the formation of gold nanosheets under the monolayer (see text for details).

5.2-2 Immobilization and reduction of chloroaurate ($AuCl_4^-$) ions at the air–water interface

In a typical experiment, a known volume of hydrophobized $AuCl_4^-$ ions (obtained as described above in section 5.2-1) with 1 mg/mL concentration of the ODA/BDSAC in

chloroform was spread on 10^{-4} M aqueous anthranilic acid (4-aminobenzoic acid, $NH_2C_6H_4COOH$) solution as the subphase in a LB trough (Scheme 1, step 2). After measurement of the π–A isotherms, the $AuCl_4^-$ ion monolayer was compressed to a surface pressure of 30 mN/m and maintained at this pressure for 4 h. After complete reduction of the hydrophobized $AuCl_4^-$ ion Langmuir monolayer (Scheme 1, step 3), multilayer films of the anthranilic acid-reduced gold nanoparticles of different thickness were formed by the LB technique as the details given in chapter 2.

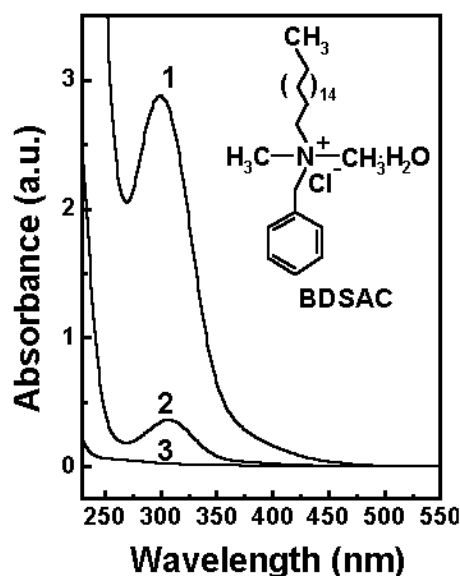## 5.2-3 UV-vis spectroscopic analysis

Figure 5.1 UV-vis spectra of the aqueous phase of the biphasic mixture of aqueous chloroauric acid (HAuCl₄) and surfactant (ODA and BDSAC) in chloroform before and after the phase transfer of chloroaurate ions $AuCl_4^-$ ions from the aqueous to the chloroform phase. Curve 1: spectrum of the aqueous phase before phase transfer; Curve 2: spectrum of the aqueous phase after phase transfer with ODA; curve 3: spectrum of the aqueous phase after phase transfer with BDSAC. The inset shows the molecular structure of BDSAC monohydrate.

The extent of phase transfer of $AuCl_4^-$ ions from the aqueous to the chloroform phase using two different surfactants, ODA and BDSAC, was estimated from UV-vis spectroscopic analysis. Fig. 5.1 shows the UV-vis spectra of the aqueous chloroauric acid (HAuCl₄) solution before and after phase transfer of $AuCl_4^-$ ions from the aqueous to the chloroform phase while the inset shows the molecular structure of BDSAC monohydrate.

Curve 1 is the spectrum of the aqueous phase before phase transfer while curves 2 and 3 correspond to the spectra of the aqueous phase after phase transfer with ODA and BDSAC respectively. An intense resonance at 300 nm due to absorption by the Au^{+3} ions [4] is observed in curve 1. Significant reduction in intensity of this absorption band after vigorous stirring of the biphasic mixture (curves 2, 3) indicates phase transfer of $AuCl_4^-$ ions from the aqueous to the chloroform phase. Simple back-of-the envelope calculations (within the accuracy limits of absorption spectroscopy) show that 88% and 99% of $AuCl_4^-$ ions have been transferred into the chloroform phase using ODA and BDSAC as phase transfer agents respectively. Amine groups of the ODA molecules are protonated at the pH of chloroauric acid solution (pH 3.7) and thus complex electrostatically with the $AuCl_4^-$ ions during vigorous stirring of the biphasic mixture of aqueous chloroauric acid and ODA in chloroform. This results in the $AuCl_4^-$ ions bound to the ODA molecules becoming sufficiently hydrophobic and amenable to transfer into chloroform. In the case of phase transfer of $AuCl_4^-$ ions with BDSAC, electrostatic interactions between the surfactant and $AuCl_4^-$ ions are expected to be stronger due to the cationic quaternary ammonium head groups of BDSAC molecules, thereby leading to a larger percentage (99%) of $AuCl_4^-$ ions transferred into the organic phase. UV-Vis spectroscopic measurements also indicate that the phase transfer of $AuCl_4^-$ ions from the aqueous to the chloroform phase is more efficient using BDSAC than ODA as a phase transfer agent. We believe that the $AuCl_4^-$ ions are entrapped in the hydrophilic cavities of the micelles formed by the surfactant molecules. Even though most studies on the synthesis of gold nanoparticles in organic solvents use phase transfer molecules similar to those used in this study (the Brust method), [3a] to the best of our knowledge, the exact nature of the gold ion-phase transfer molecule complex in the organic phase prior to metal ion reduction is poorly understood.

5.2-4 Surface pressure–area (π–A) isotherm measurements

Surface pressure–area (π–A) isotherm measurements were performed to check the ability of surfactant molecules complexed with $AuCl_4^-$ ions ($ODA^+- AuCl_4^-$ and $BDSA^+-AuCl_4^-$) to form stable Langmuir monolayers on an aqueous subphase. In Fig. 5.2A and

(B), curve 1 shows the π–A isotherm cycle of ODA$^+$–AuCl$_4^-$ and BDSA$^+$–AuCl$_4^-$, respectively, on the surface of acidic aqueous subphase (pH of water adjusted to 4.5 using conc. HCl, since pH of 10^{-4} M anthranilic acid solution was measured to be ca. 4.5) recorded 1 h after spreading the monolayers.
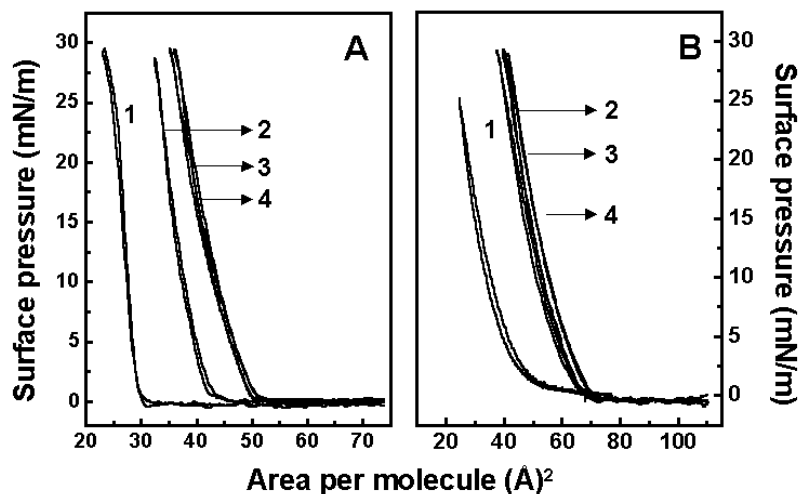

Figure 5.2 (A) Curve 1: π–A isotherm during one compression and expansion cycle of octadecyl amine electrostatically complexed with chloroauric acid (ODA$^+$-AuCl$_4^-$) on acidic water (pH 4.5) subphase recorded 1 h after spreading the monolayer. Curves 2, 3, 4: π–A isotherms of ODA$^+$-AuCl$_4^-$ on 10^{-4} M aqueous anthranilic acid subphase recorded 10 min, 1 h and 3 h after spreading the monolayer, respectively. **(B)** Curve 1: π–A isotherm during one compression and expansion cycle of benzyldimethylstearylammonium chloride electrostatically complexed with chloroauric acid (BDSA$^+$- AuCl$_4^-$) on acidic water (pH 4.5) subphase recorded 1 h after spreading the monolayer. Curves 2, 3, 4: π–A isotherms of BDSA$^+$- AuCl$_4^-$ on 10^{-4} M aqueous anthranilic acid subphase recorded 10 min, 1 h and 3 h after spreading the monolayer, respectively.

Curves 2, 3 and 4 in Fig. 5.2A and B likewise correspond to π–A isotherms recorded from ODA$^+$–AuCl$_4^-$ and BDSA$^+$–AuCl$_4^-$ monolayers on the surface of a 10^{-4} M aqueous anthranilic acid subphase recorded 10 min, 1 h and 3 h after spreading the monolayers, respectively. A steep build up in surface pressure in both cases up to 30 mN/m indicates that the ODA$^+$–AuCl$_4^-$ and BDSA$^+$–AuCl$_4^-$ form stable monolayers on both acidic aqueous subpphase and aqueous anthranilic acid subphase (Fig. 5.2A and B). This clearly indicates that in both cases of acidic aqueous subphase (pH 4.5) and anthranilic acid subphase, ODA$^+$–AuCl$_4^-$ and BDSA$^+$–AuCl$_4^-$ behave like classical

amphiphiles. The hydrophilic $AuCl_4^-$ ions complexed with the hydrophobic surfactant molecules anchor the ODA/BDSAC molecules to the subphase. It is likely that once spread on the surface of water/aqueous anthranilic acid subphase, the micellar structure of the $ODA^+–AuCl_4^-$ and $BDSA^+–AuCl_4^-$ complexes, is disrupted resulting in the formation of a gold ion–surfactant monolayer on the subphase (Scheme 5.1, step 2). It is important to note that at the take-off pressure the molecular area of the $ODA^+–AuCl_4^-$ monolayer on the anthranilic acid subphase (50 $Å^2$/molecule) recorded immediately after spreading the monolayer (Fig. 5.2A, curve 2) is much higher than that recorded for this Langmuir monolayer (32 $Å^2$/molecule, Fig. 5.2A, curve 1) on acidic aqueous subphase (pH 4.5). A similar increase in take-off area from 50 $Å^2$/molecule to 70 $Å^2$/molecule is observed in the case of the $BDSA^+–AuCl_4^-$ monolayer on changing the subphase from acidic water (pH 4.5) to aqueous anthranilic acid solution (Fig. 5.2B, curves 1 and 2, respectively). This clearly indicates that anthranilic acid molecules present in the subphase interact with the $ODA^+–AuCl_4^-$ and $BDSA^+– AuCl_4^-$ monolayers. It is also observed that there is a small increase in the molecular take-off area in the $\pi–A$ isotherms of the $ODA^+–AuCl_4^-$ and $BDSA^+–AuCl_4^-$ monolayers on the anthranilic acid subphase with time (Fig. 5.2A and B, curves 2, 3 and 4). This suggests that anthranilic acid molecules present in the subphase are very easily accessible to the $AuCl_4^-$ ions (which are bound to the surfactant monolayer and thus localized at the interface). The process of reduction of the gold ions by anthranilic acid in the subphase could be observed by the appearance of a faint violet color at the interface that is characteristic of gold nanostructures. Since the gold ions are constrained to a monolayer at the air–water interface by the new strategy outlined above, we anticipate that reduction of these highly localized ions would result in a high degree of anisotropy in the shape of the gold nanostructures formed.

5.2-5 Transmission electron microscopy results

The morphology of anthranilic acid-reduced gold nanostructures formed at the air-water interface was studied by depositing two monolayers (2 ML) LB film of the nanoparticles on carbon-coated TEM grids. Figs. 5.3A–D and 5.4A–C show

representative TEM images of anthranilic acid-reduced gold nanoparticles obtained from the $ODA^+-AuCl_4^-$ and $BDSA^+-AuCl_4^-$ Langmuir monolayers, respectively, at different magnifications.
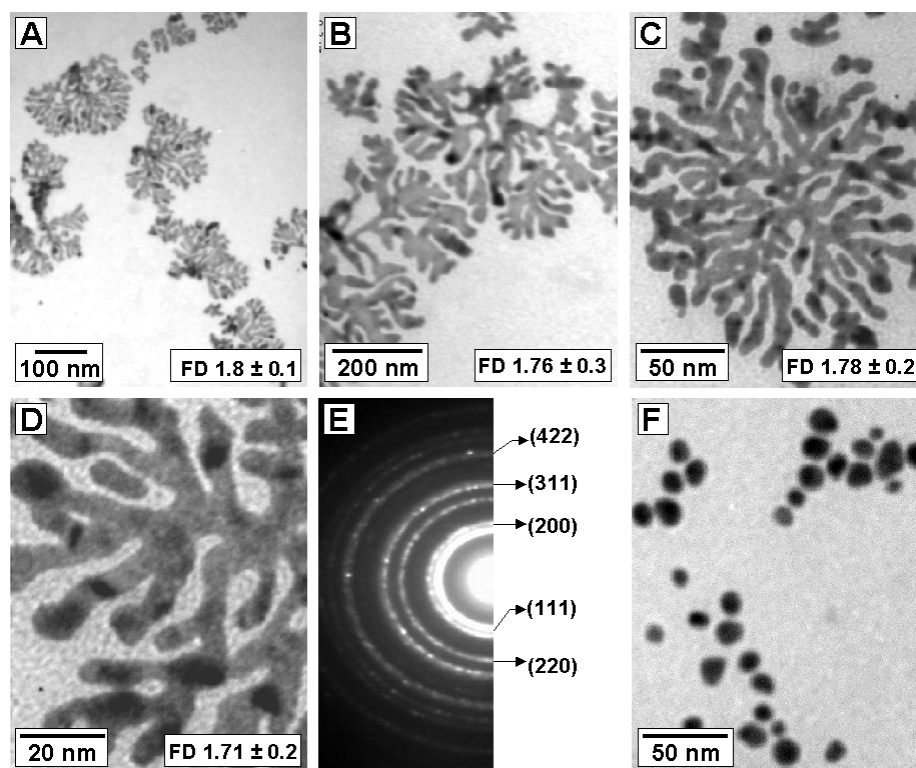

Figure 5.3 (A)–(D) Representative TEM images of gold nanostructures formed at the air–water interface by the reduction of $AuCl_4^-$ ions (immobilized on the surface of 10^{-4} M aqueous anthranilic acid subphase by complexing with ODA) using anthranilic acid as a reducing agent present in the subphase, recorded at different magnifications. Respective fractal dimensions are shown in the images. **(E)** Electron diffraction pattern recorded from flat gold nanostructures shown in image (D). **(F)** TEM image of gold nanoparticles formed at the liquid–liquid interface by the reduction of hydrophobized $AuCl_4^-$ ions (hydrophobized by complexing with ODA) in chloroform using 10^{-3} M aqueous anthranilic acid solution as a reducing agent present in the biphasic mixture.

In both cases, assemblies of gold nanostructures are observed uniformly over the surface of the TEM grid at low magnification (Figs. 5.3A and 5.4A). The higher magnification images (Figs. 5.3B–D, 5.4B–C) reveal that the gold nanostructures obtained from both $ODA^+-AuCl_4^-$ and $BDSA^+-AuCl_4^-$ Langmuir monolayers are highly anisotropic, flat and irregular in shape. Closer examination reveals that there are

remarkable differences between the gold nanostructures obtained using ODA and BDSAC as complexation agents. An important and fascinating feature of the gold nanostructures obtained by reduction of the $ODA^+- AuCl_4^-$ monolayer is that they show a high frequency of fractal, dendritic structures of nanoscale dimensions extending to lengths of up to 200 nm (Fig. 5.3A–D). Fractal dimensions of a number of nanostructures in these images were determined and were found to vary from 1.71 ± 0.2 to 1.8 ± 0.1. Fractal dimensions have been calculated using the radial mass distribution method. In this calculation scheme, the number of pixels (picture elements) N(R) in a given radius R is measured. Since for a growing fractal, $N(R) \sim R^D$, a plot of ln N(R) vs. ln R results in a curve which has an asymptotic slope equal to the fractal dimension, D[5]. The error in the fractal dimension is essentially the error in the slope of the asymptotic line. The slope in the ln N(R) vs. ln R plot was determined by the method of least squares. The formation of silver and gold fractal structures has been previously observed in solution under sonochemical [6] or ultrasonic agitation [7,8] and in the presence of specific surface modifiers [9-11]. Very recently, formation of fractal gold nanostructures by the spontaneous reduction of chloroaurate ions entrapped in thermally evaporated hexadecylaniline thin films due to diffusion limited aggregation has been demonstrated in this laboratory [12]. The gold fractal nanostructures obtained in this study are characteristic of diffusion-limited aggregated (DLA) structures [13]. Indeed, the fractal dimensions of the gold nanostructures obtained by reduction of $ODA^+-AuCl_4^-$ monolayers in the present study (1.7–1.8; Fig. 5.3A–D) are in the range expected for DLA structures (< 2) [13,14]. While the exact mechanism leading to formation of the fractal gold nanoparticles is not clear at the moment, we believe that the strong binding of the ODA molecules with the gold nanoparticle surface (since chloroaurate ions are hydrophobized with ODA before spreading on surface of aqueous subphase) may be partly responsible for this. While flat gold nanosheets of size ranging from 10 to 100 nm are obtained by reduction of the $BDSA^+-AuCl_4^-$ monolayer at the air–water interface (Fig. 5.4B and C), they do not demonstrate the same fractal structure as observed in case of $ODA^+-AuCl_4^-$ monolayer. Figs. 5.3E and 5.4D show electron diffraction patterns

recorded from the single flat gold nanostructure shown in Figs. 5.3D and 5.4C, respectively. It is clear from the electron diffraction pattern that the gold nanostructures formed using both ODA and BDSAC are polycrystalline in nature.
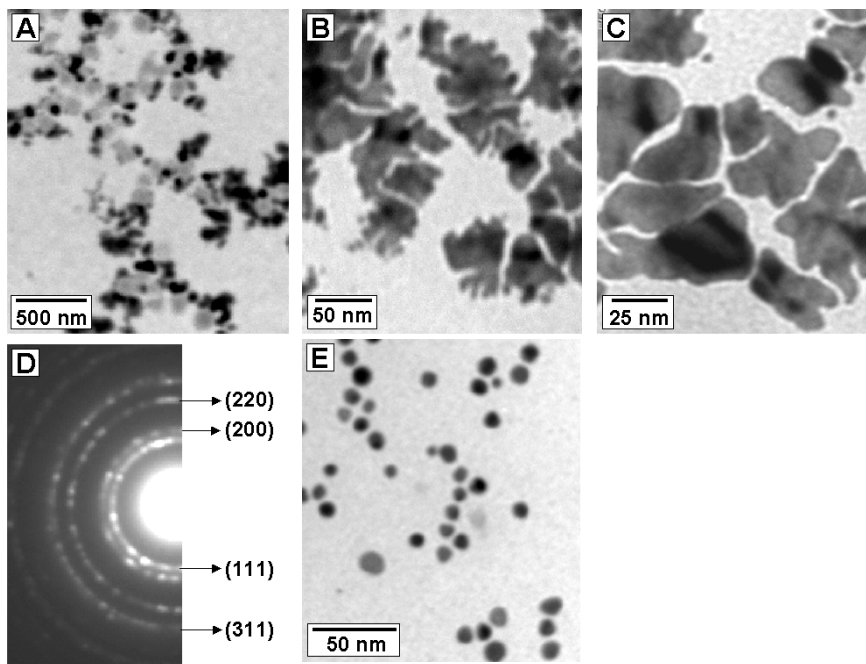

Figure 5.4 (A)–(C) TEM images of gold nanostructures formed at the air–water interface by the reduction of $AuCl_4^-$ ions (immobilized on the surface of 10^{-4} M aqueous anthranilic acid subphase by complexing with BDSAC) using anthranilic acid as a reducing agent present in the subphase, recorded at different magnifications. **(D)** Electron diffraction pattern recorded from flat gold nanostructure shown in image (C). **(E)** TEM image of the gold nanoparticles formed at the liquid–liquid interface by the reduction of hydrophobized $AuCl_4^-$ ions (hydrophobized by complexing with BDSAC) in chloroform using 10^{-3} M aqueous anthranilic acid solution as a reducing agent present in the biphasic mixture.

The characteristic rings in the polycrystalline diffraction pattern could be indexed as the allowed Bragg reflections from the (111), (200), (220) and (311) lattice planes of fcc gold. In order to confirm that the formation of flat, anisotropic nanostructures at the air–water interface is really a consequence of localization of gold ions at the two dimensional surface, control experiments were performed wherein chloroaurate ions ($AuCl_4^-$ ions) hydrophobized with ODA and BDSAC were reduced separately in solution (at the liquid–liquid interface) using 10^{-3} M aqueous anthranilic acid solution under

constant stirring for 1 h. Spherical nanoparticles with size in the range 10 to 20 nm are obtained (Figs. 5.3F and 5.4E) in contrast to the morphology obtained at the air–water interface (Figs. 5.3D and 5.4C). The control experiments thus ensure that the flat, anisotropic nature of nanostructures formed at the air–water interface is truly the result of immobilization of gold ions at the air–water interface and the highly localized reduction of these ions constrained to the monolayer. It may be pointed out here that the dimensions of the gold nanostructures formed in the present study (50 nm-200 nm) are much smaller than the gold nanoribbons that extended upto few micrometers in length (obtained in our previous study as discussed in chapter 4) by the reduction of $AuCl_4^-$ ions using 4-HDA or AT Langmuir monolayer as a reducing agent. This is because of the very low concentration of $AuCl_4^-$ ions within the Langmuir monolayer of ODA^+–$AuCl_4^-$ and $BDSA^+$–$AuCl_4^-$ on an aqueous subphase in comparison with the comparatively high concentration at the interface when 4-HDA or AT monolayer was spread on the surface of aqueous $HAuCl_4$ subphase.

5.2-6 UV-vis spectroscopic analysis

One of the important advantages of the LB technique is that it permits the characterization and utilization of nanoparticles and nanoparticulate films in the solid state by enabling their transfer onto the solid substrate at any stage of their growth. Multilayer LB films of anthranilic acid-reduced gold nanoparticles were deposited on quartz substrates by the LB technique to study their optical properties. Figs. 5.5A and 5.6A show the UV-vis spectra of LB films of gold nanostructures of different thickness obtained by the reduction of ODA^+–$AuCl_4^-$ and $BDSA^+$–$AuCl_4^-$ monolayers, respectively. Broad absorption bands centered at ca. 565 nm and 590 nm are observed in these two cases and their intensity increases with increasing number of monolayers in the LB film. The absorption bands at 565 nm and 590 nm are due to excitation of surface plasmons in gold nanoparticles and are responsible for the characteristic pink/violet color of solutions/ films of gold nanoparticles [15]. Well-dispersed, spherical gold nanoparticles in solution show a sharp surface plasmon resonance in the range 510 nm – 530 nm.
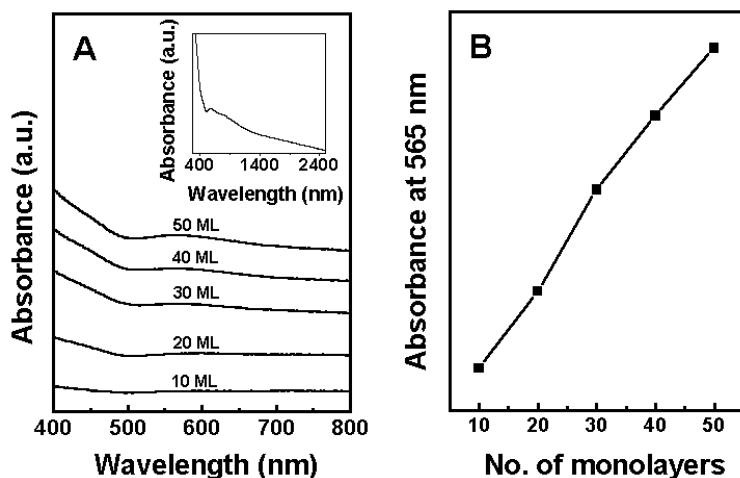
Figure 5.5 (A) UV-vis spectra of LB films of gold nanoparticles deposited on a quartz substrate formed at the air–water interface by the reduction of chloroaurate ($AuCl_4^-$) ions (immobilized at the air–water interface using octadecylamine, ODA) using 10^{-4} M anthranilic acid as a reducing agent present in the subphase, recorded as a function of number of monolayers in the LB films. The number of monolayers of the gold nanoparticles in the LB films is indicated next to the respective curves. The inset shows the UV-vis spectrum of a 50 ML gold nanoparticle LB film recorded in the spectral range 280–2500 nm **(B)** A plot of intensity of the surface plasmon resonance (absorbance at 565 nm) as a function of number of monolayers of LB films of anthranilic acid-reduced gold nanoparticles grown on a quartz substrate.

The shift and broadening of the resonance in the LB films indicates anisotropy in shape of the particles and thus supports the TEM results. The optical behavior revealed by these nanostructures is also consistent with that of flat, anisotropic nanostructures formed by the reduction of aqueous $AuCl_4^-$ ions using hexadecylaniline (HDA) and alkylated tyrosine (AT) Langmuir monolayer at air-water interface as described in chapter 4. The intensity of absorption band at 565 nm and 590 nm increases linearly with the film thickness (Figs. 5.5B and 5.6B) clearly indicating that the gold nanoparticle multilayers grow without change in nanoparticle density in successive layers even up to 60 monolayers (ML) thickness. The insets of Figs. 5.5A and 5.6A show the UV-vis spectra of a 60 ML thick LB film obtained from the reduction of $ODA^+-AuCl_4^-$ and $BDSA^+-AuCl_4^-$ complexes respectively, in the spectral range 280 nm - 2500 nm. A very broad absorption is observed that interestingly extends to the near infrared (NIR) region. The large absorption in the NIR is clearly a consequence of high anisotropy in the gold nanostructures in the superlattice films.
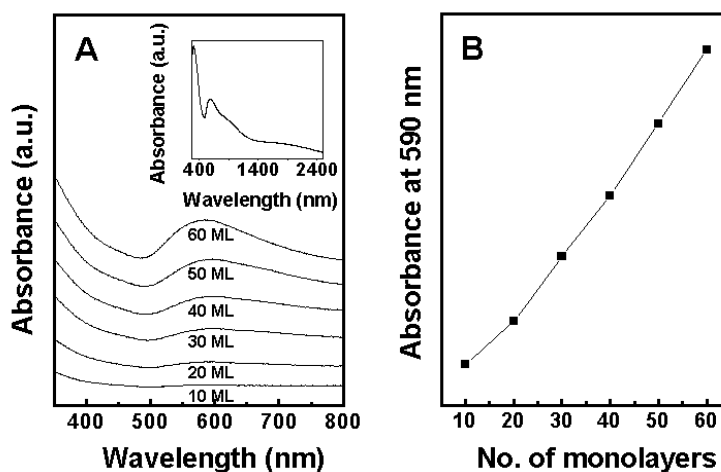
Figure 5.6 **(A)** UV-vis spectra of LB films of gold nanoparticles deposited on a quartz substrate formed at the air–water interface by the reduction of chloroaurate ($AuCl_4^-$) ions (immobilized at the air–water interface using benzyldimethylstearyammonium chloride, BDSAC) by 10^{-4} M anthranilic acid as a reducing agent present in the subphase, recorded as a function of number of monolayers. The number of monolayers of the gold nanoparticles in the LB films is indicated next to the respective curve. The inset shows the UV-vis spectrum of 60 ML LB film recorded in the spectral range 280 to 2500 nm. **(B)** A plot of intensity of the surface plasmon resonance (absorbance at 590 nm) plotted as a function of number of monolayers of LB films of anthranilic acid-reduced gold nanoparticles grown on a quartz substrate.

5.2-7 X-ray photoelectron spectroscopic analysis

A 60 ML anthranilic acid-reduced gold nanoparticle film obtained by the reduction of $BDSA^+–AuCl_4^-$ monolayer was deposited on a Si(111) substrate and analyzed by XPS. The general scan spectra of the LB film showed the presence of strong C1s, N1s and Au 4f core levels with no evidence of impurities. The film was sufficiently thick and therefore, no signal was measured from the substrate (Si 2p core level). The Au 4f, C1s and N1s core levels recorded from the film are shown in Fig. 5.7A, B and C, respectively. The spectra have been background corrected using the Shirley algorithm [16] prior to curve resolution. The Au 4f core level spectrum recorded from the LB film (Fig. 5.7A) could be deconvoluted into two spin-orbit pairs (splitting constant 3.7 eV). Two chemically distinct Au $4f_{7/2}$ components are observed at 83.8 and 87.4 eV binding energies (BEs, labelled 1 and 2 in Fig. 5.7A). The lower BE component is attributed to electron emission from Au^0 oxidation state of gold in the LB film while the high BE

component arises from unreduced Au^{+3} ions in the LB film [3b] indicating that a small fraction of the AuCl$_4^-$ ions remain in the film.
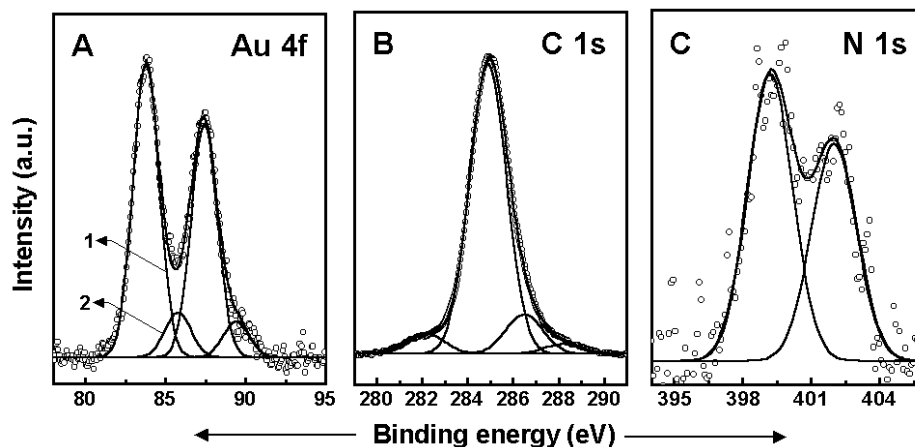

Figure 5.7 (A) Au 4f, **(B)** C 1s and **(C)** N 1s core level spectra recorded from a 60 ML anthranilic acid-reduced gold nanoparticle film transferred from the air–water interface on a Si(111) substrate by LB technique 4 h after spreading the monolayer of BDSAC complexed with chloroaurate ions on a 10^{-4} M anthranilic acid subphase. The solid lines are non-linear least square fits to the data.

The C1s core level spectrum recorded from the LB film could be deconvoluted into four components at 282.2, 284.9, 286.5 and 288.4 eV (Fig. 5.7B) indicating the presence of four chemically distinct carbons in the film. The high BE component observed at 288.4 eV can be assigned to the carbon bonded to oxygen in the carboxylic group of anthranilic acid which is also observed in the C1s core level spectrum recorded from the drop-coated film of an aqueous solution of only anthranilic acid. The 286.5 eV BE peak is attributed to the carbon adjacent to the carboxylic acid group in anthranilic acid. Two chemically distinct components of the N1s core level spectrum are observed at 399.2 eV and 402 eV (Fig. 5.7C). The presence of two N1s signals also supports the presence of anthanilic acid in the LB film along with the hydrophobizing agent, BDSAC.

Thus it is clear from the above studies that the chloroaurate ions can be easily immobilized at the air-water interface by rendering them hydrophobic. Hydrophobization can be accomplished by complexing them with surfactants such as ODA and BDSAC at the liquid–liquid interface and facilitating their phase transfer into chloroform. Reduction of chloroaurate ions constrained to a monolayer at the air–water interface by anthranilic

acid present in the subphase results in the formation of highly anisotropic, flat gold nanostructures which can be transferred onto suitable solid substrates in a lamellar fashion to form superlattice films of desired thickness using the elegant LB technique.

References

(1) Khomutov, G.B.; Bykov, I.V.; Gainutdinov, R.V.; Gubin, S.P.; Obydenov, A.Yu.; Polyakov, S.N.; Tolstikhina, A.L. *Colloids and Surfaces A* **2002**, *198–200,* 347.

(2) Khomutov, G. B. *Colloids and Surfaces A* **2002**, *202,* 243.

(3) (a) Brust, M.; Walker, M.; Bethell, D.; Schiffrin, D. J.; Whyman, R. *Chem. Comm*. **1994**, 801. (b) Leff, D. V.; Brandt, L.; Heath, J. R. *Langmuir* **1996**, *12*, 4723.

(4) Henglein, A. *Langmuir* **1999**, *15*, 6738.

(5) Vicsek, T. "*Fractal Growth Phenomena*" World Scientific, Singapore, 2nd edn., **1992**.

(6) Nikitenko, S. I.; Koltypin, Y.; Mastai, Y.; Koltypin, M.; Gedanken, A. *J. Mat. Chem*. **2002**, *12*, 1450.

(7) Xiao, J.; Xie, Y.; Tang, R.; Chen, M.; Tian, X. *Adv. Mater*. **2001**, *13*, 1887.

(8) Zhu, J.; Liao, X.; Chen, H-Y. *Mat. Res. Bull*. **2001**, *36*, 1687.

(9) Zhou, Y.; Yu, S. H.; Wang, C. Y.; Li, X. G.; Zhu Chen, Y. R. Z. Y. *Adv. Mater*. **1999**, *11*, 850.

(10) Wang, X.; Naka, K.; Itoh, H.; Park, S.; Chujo, Y. *Chem. Comm*. **2002**,1300.

(11) Selvan, S. T. *Chem. Comm*. **1998**, 351.

(12) Mandal, S.; Phadtare, S.; Selvakannan, PR.; Pasricha, R.; Sastry, M. *Nanotech.* **2003**, *14*, 878.

(13) Lin, M. Y.; Lindsay, H. M.; Weitz, D. A.; Ball, R. C.; Klein, R.; Meakin, P. *Nature* **1989**, *339*, 360.

(14) Solecka-Cermakova, K.; Vlckova, B.; Lednicky, F. *J. Phys. Chem*. **1996**, *100*, 4954.

(15) (a) Henglein, A. *J. Phys. Chem*. **1993**, *97*, 5457. (b) Mayya, K. S.; Patil, V.; Sastry, M. *Langmuir*, **1997**, *13*, 2575.

(16) Shirley, D. A. *Phys. Rev. B*. **1972**, *5*, 4709.

C H A P T E R VI

Summary

The salient features of the work detailed in the thesis and possible avenues for future work are briefly discussed.

Summary of work

The use of air-water interface for the two dimensional (2D) assembly of hydrophobized nanoparticles and synthesis of anisotropic nanostructures is the objective of this thesis. It has been shown that long chain alkylamines (octadecyl amine, ODA) capped gold and silver nanoparticles spread on the surface of water and form stable Langmuir monolayer, Langmuir-Blodgett (LB) films of which can be deposited on different solid substrates in a layer by layer fashion using LB technique. Though many reports are available in the literature for the 2D assembly of metal nanopparticles by LB technique, alkane thiols are primarily used as nanoparticle passivating agent in most of the cases. The interaction of thiols with the nanoparticles is covalent as against the electrostatic interaction in case of capping with alkyl amine molecules. The interparticle separation and the 2D arrangement of the nanoparticles in both the cases are similar as the assembly is directed by the hydrophobic interactions of the capping agents. However the additional advantage that alkyl amines offer is that, they can be used in general to assemble any negatively charged nanoparticles as compared with thiol molecules that are restricted to those nanoparticles that have ability to interact through their surface.

Further, the built in anisotropy of air-water interface has been utilized for selective synthesis of anisotropic gold nanostructures. On confining the reduction of the metal ions just below the Langmuir monolayer, interesting anisotropic growth of metallic nanocrystals was observed. The selective reduction of the metal ions at the air-water interface has been achieved in two ways (1) *by confining the reductant at the air-water interface*: Surfactants such as 4-hexadecylaniline (4-HDA) and alkylated tyrosine (AT) possess sufficiently long hydrocarbon chain to form stable Langmuir monolayer on an aqueous subphase and bear a head group with reducing capability. Thus when spread on the surface of aqueous gold ion solution, 4-HDA and AT molecules complex electrostatically with the gold ions and reduce them at the air-water interface to generate flat, anisotropic sheet like structures. It was observed that the growth of these nanostructures is highly face selective. (2) *by confining the metal*

ions at the air-water interface wtih reducing agent in the aqueous subphase: Gold ions hydrophobized with surfactants such as ODA and benzyldimethylstearylammonium chloride (BDSAC) when spread on the surface of aqueous anthranilic acid subphase, undergo reduction to evolve into flat, anisotropic nanostructures at air-water interface.

Scope for future work

The study of interparticle interactions (conduction and plasmon coupling) in 2D assembly of alkyl amine capped gold and silver nanoparticles could be interesting in order to explore their potential applications in electron transport systems. One of the most attracive prospect of the strategy of hydrophobizing nanoparticles using elctrostatic interactions is that any kind of nanoparticles that can be charged using suitable surfactant can be organized on the surface of water to form a 2D assembly. Films of which can be deposited on solid substrates by LB technique. In particular, method can be extended to get the ordered assemblies of technologically important, oxide and magnetic nanoparticles.

Method for generating anisotropic nanostructures at the air-water interface, can be modified using appropriate additives in the subphase that will inhibit or promote the growth in particular direction to give more regular shaped nanostructures. Further the protocol for hydrophobizing gold ions can be extended to other ions such as cadmium (Cd), zinc (Zn), lead (Pb) etc. thus providing a simple general route for the synthesis on anisotropic nanostructures of important semiconductors like CdS, ZnS and PbS etc.

List of Publications

1) "One-step synthesis of ordered two-dimensional assemblies of silver nanoparticles by the spontaneous reduction of silver ions by pentadecylphenol Langmuir monolayers"

   A. Swami, PR. Selvakannan, R. Pasricha, M. Sastry, *J. Phys. Chem. B* 108 (2004) 19269**.**

2) "Phase transfer of oelic acid capped Ni_{core} Ag_{shell} nanoparticles assisted by the flexibility of oleic acid on the surface of silver"

   T. Bala, **A. Swami**, B. L. V. Prasad, M. Sastry, *J. Colloid Int. Sci.* (2004) doi:10.1016/j.jcis.2004.09.018

3) "Synthesis of aqueous Au core-Ag shell nanoparticles using tyrosine as a pH-dependent reducing agent and assembling phase-transferred silver nanoparticles at the air-water interface"

   PR. Selvakannan, **A. Swami**, D. Srisathiyanarayanan, P.Shirude, R. Pasricha, A. B. Mandle, M. Sastry, Langmuir 20 (2004) 7829.

4) "Flat gold nanostructures by the reduction of chloroaurate ions constrained to a monolayer at the air–water interface"

   A. Swami, M. Kasture, R. Pasricha, M. Sastry, *J. Mater.Chem.*14 (2004) *709*.

5) "Variation in morphology of gold nanoparticles synthesized by the spontaneous reduction of aqueous chloroaurate ions by alkylated tyrosine at a liquid-liquid and air-water interface"

   A. Swami, A. Kumar, M. D`Costa, M. Sastry, *J. Mater. Chem.* 14 (2004) 2696.

6) "Formation of platinum nanoparticles at air-water interfaces by the spontaneous reduction of subphase chloroplatinate anions by hexadecylaniline Langmuir monolayers"

   A. Swami, A. Kumar, R. Pasricha, A.B. Mandale, M. Sastry, *J. Colloid Int. Sci***.** 271 (2004) 381.

7) "Highly oriented gold nanoribbons by the reduction of aqueous chloroaurate ions by hexadecylaniline Langmuir monolayers"

   A. Swami, A. Kumar, PR. Selvakannan, S. Mandal, R. Pasricha, M. Sastry, *Chem. Mater*. 15 (2003) 17.

8) "Formation of water-dispersible gold nanoparticles using a technique based on surface-bound interdigitated bilayers"

   A. Swami, A. Kumar, M. Sastry, *Langmuir* 19 (2003) 1168.

9) "Langmuir-Blodgett films of laurylamine-modified hydrophobic gold nanoparticles organized at the air-water interface"

   A. Swami, A. Kumar, PR. Selvakannan, S. Mandal, M. Sastry, *J. Colloid Int. Sci.* 260 (2003) 367.

10) "Lamellar multilayer hexadecylaniline-modified gold nanoparticle films deposited by the Langmuir-Blodgett technique"

    A. Swami, A. Kumar, M. Sastry, *Proc. Indian Acad. Sci. (Chem. Sci.)* 115 (2003) 185.

11) "Water-dispersible nanoparticles via interdigitation of sodium dodecylsulphate molecules in octadecylamine-capped gold nanoparticles at a liquid-liquid interface"

    A. Swami, A. Jadhav, A. Kumar, S. D. Adyanthaya, M. Sastry, *Proc. Indian Acad. Sci. (Chem. Sci.)* 115 (2003) 679.